

TECHNISCHE UNIVERSITÄT MÜNCHEN



Lehrstuhl für Technische Physik E19

Interfaces and Energy Conversion

**Electrocatalytic activity of platinum on extended gold surfaces
and defined gold-nanostructure arrays for the hydrogen
reactions**

Cornelia Ostermayr

Vollständiger Abdruck der von der Fakultät für Physik der Technischen Universität München zur Erlangung des akademischen Grades eines

Doktors der Naturwissenschaften (Dr. rer. nat.)

genehmigten Dissertation.

Vorsitzender: Univ.-Prof. Dr. A. Zaccone

Prüfer der Dissertation:

1. Univ.-Prof. Dr. U. Stimming (nur schriftliche Beurteilung)
2. apl. Prof. Dr. P. Müller-Buschbaum
3. Univ.-Prof. P. Lugli, Ph.D.

Die Dissertation wurde am 13.01.2014 bei der Technischen Universität München eingereicht und durch die Fakultät für Physik am 12.02.2015 angenommen.

Content

1	Introduction.....	5
2	Fundamentals	9
2.1	Electrochemical potential and reactions.....	9
2.1.1	Electrode potential and electrochemical double layer	9
2.1.2	Kinetics of electrode reactions.....	12
2.1.3	Electrochemical reactions at constant electrode potential	18
2.2	Selected electrodes and charge-transfer reactions.....	21
2.2.1	The hydrogen reactions.....	21
2.2.2	The Au(111) surface	23
2.2.3	Metal deposition.....	26
2.3	Bimetallic electrocatalysis – Interplay of support and catalyst material.....	28
2.3.1	Strain and density functional theory	29
2.3.2	Defect density	32
2.3.3	Spillover.....	35
3	Materials and methods	39
3.1	Equipment and consumables.....	39
3.2	Support material	40
3.2.1	Gold films on glass	40
3.2.2	Nanostructured gold surfaces.....	41
3.3	Deposition of platinum islands and particles on gold	43
3.3.1	Electrochemical deposition.....	43
3.3.2	Micellar technique	45
3.4	Characterization techniques	47
3.4.1	X-ray photoelectron spectroscopy	47
3.4.2	Scanning probe microscopy.....	48
3.4.3	Electrochemical impedance spectroscopy	49
3.4.4	Cyclic voltammetry.....	51
3.4.5	Potentiostatic single pulse technique	53

4	Results.....	57
4.1	Platinum nanoislands on Au(111) – Variation of deposition sites and coverage	57
4.1.1	Characterization of platinum deposit.....	57
4.1.2	Dependence of electrocatalytic activity on coverage.....	64
4.2	Platinum nanoislands on Au(111) – Variation of defect density on the Au(111) surface.....	67
4.2.1	Defect-poor and defect-rich Au(111).....	68
4.2.2	Characterization of platinum deposit.....	71
4.2.3	Dependence of electrocatalytic activity on defect density.....	76
4.3	Platinum nanospheres from micellar diblock-copolymers on Au(111).....	79
4.3.1	Characterization of platinum nanospheres.....	79
4.3.2	Dependence of electrocatalytic activity on particle height.....	84
4.4	Electrochemical properties of defined nanostructure arrays.....	88
4.4.1	Gold pillars on highly doped silicon.....	88
4.4.2	Platinum nanoislands on gold lines between polymer lines.....	94
5	Discussion.....	101
5.1	Platinum nanoislands on Au(111) – Double pulse deposition and dependence of electrocatalytic activity on deposition sites and coverage.....	101
5.2	Platinum nanoislands on defect-rich Au(111) – Spillover effect for the hydrogen oxidation reaction.....	103
5.3	Relevance of strain: Platinum nanospheres compared with platinum nanoislands	105
5.4	Gold pillars on highly doped silicon.....	107
5.5	Relevance of spillover: Platinum nanoislands on gold lines.....	107
6	Summary and conclusions.....	111
	Bibliography.....	115
	Appendix.....	123
	A1 Symbols and abbreviations.....	123
	A2 Additional experimental details.....	127
	A3 Publications.....	129

Danksagung..... 131

1 Introduction

The term *electrocatalysis* (derived from Greek *elektron* – amber and *kata-lyein* – ease or aid) is used in the field of electrochemistry. Electrochemistry is the science of chemical effects that are caused by an electric field and of electric effects that are due to a chemical reaction. Hence, electrochemistry refers to a large research field encompassing numerous different phenomena, such as electrophoresis or corrosion. In contrast, electrocatalysis corresponds to a specific correlation in the field of electrochemistry: It defines a change in the rate and selectivity of an electrochemical reaction, which is caused by a substance that participates in the reaction but is neither consumed nor chemically changed [1, 2]. The change in the reaction rate and selectivity is closely related to adsorption of reactants, intermediates and/or products on the surface of so-called electrocatalysts. Therefore, electrocatalytic reactions are in general very surface sensitive and determined by specific properties of the electrocatalyst.

The classical example of an electrocatalytic reaction is the hydrogen evolution reaction (HER) at platinum (Pt) electrodes, which has been investigated extensively since the beginning of the 20th century [3-11]. However, at that time electrode structures were often poorly defined, such that systematic investigations of the complex underlying multistep mechanism were not possible. Today, the preparation and characterization of single crystal surfaces are well-understood and documented [12-16]. Nevertheless, investigation of the HER at these defined electrode surfaces was not enough to reveal and identify the reaction mechanism. First, there is no unique reaction mechanism for all kinds of electrode material (compare with e.g. [17-20]) and second, the utilization of small nanoparticles showed that the electrochemical properties of a certain material can be altered to a great extent [21]. For instance, a gold (Au) surface is usually inert in electrochemical experiments, i.e. it does not yield a considerable current in an electrochemical reaction unless very high potentials are applied. However, nanoparticles of Au with a diameter between 5nm and 30nm on highly oriented pyrolytic graphite (HOPG) show an enhanced activity for the oxygen reduction reaction (ORR), when compared to the extended Au surface [22]. Thus, in spite of greatly improved techniques, even nowadays it remains a challenge to correlate electrode geometry to activity:

Systematic investigations are complicated because of multiple, partly linked parameters such as size and spacing of catalyst particles, type of support material and electrolyte.

Hence, the hydrogen electrode is revisited once again to illustrate this correlation: In the last years, an activity enhancement regarding hydrogen evolution and oxidation reaction (HER, HOR) on palladium (Pd) and platinum catalyst monolayers and submonolayers on Au(111) supports was found with respect to bulk Pd and Pt. In particular, an increase of the catalytic activity is on the one hand found for decreasing amounts of Pd and Pt [23-28] and on the other hand for an increasing defect density on the Au surface [23, 29]. However, such an enhancement does not occur for Pt on HOPG or single-crystalline diamond [30-32]. While the interaction of Pt nanoislands/-particles with Au(111) is relatively strong, the opposite holds true for carbon supports. Since the physical and chemical background underlying these results is still not completely understood it is important to thoroughly investigate the above mentioned systems experimentally and theoretically. Therefore, several research groups focus on density functional theory (DFT) calculations in order to relate the shift of d-band centers of metal layers in a certain configuration to corresponding adsorption energies of different compounds, such as CO or hydrogen atoms [33-39]. These findings delivered an explanation for the enhancement of Pd/Pt activity on Au with decreasing number of catalyst monolayers. However, these calculations do not account for an increase of the specific electrocatalytic activity with decreasing amount of catalyst at submonolayer coverage. In this regime, a higher activity of catalyst islands on step or defect sites, changed adsorption sites of hydrogen atoms on such islands as well as the spillover effect can be responsible for the enhancement [40-42]. The spillover effect refers to a transition of adsorbed hydrogen atoms from the catalyst to the free Au(111) surface. In order to learn more about these effects further investigations of the interplay of the Au surface and the catalyst nanostructures are important. This can be achieved by varying corresponding physical parameters, such as nanoisland/-particle size, shape or distance, support material or surface properties of the support material.

Therefore, one part of this thesis is focused on the electrocatalytic activity of Pt nanostructures on extended Au(111) surfaces. In a first approach, Pt was electrochemically deposited on the Au(111) surface with varying deposition parameters. Hence, the influence of Pt coverage and deposition routine on electrocatalytic activity was analyzed. Electrochemical deposition of Pt on Au yields randomly distributed, flat, “two-dimensional” nanoislands, i.e. Pt nanostructures are mostly one atomic layer in

height, not exceeding a height of three atomic layers. Since Pt nanoislands grow pseudomorphically on Au(111) [43] the Pt-lattice constant has to match the one of the Au surface. Consequently, tensile strain occurs in the Pt nanoisland, since the lattice constant of Pt is smaller than the one of Au. Furthermore, the defect density on the Au(111) surface was varied for constant Pt coverage. The electrocatalytic activity of Pt on defect-poor Au(111) and of Pt on defect-rich Au(111) was compared. Defect-rich Au(111) was generated by electrochemical oxidation and reduction of a defect-poor surface. By these means the influence of a potential-induced defect density on the Au(111) surface on electrocatalytic properties of Pt nanoislands was quantified.

In a second approach, spherical Pt nanoparticles were established on the Au(111) surface by diblock copolymer micelle lithography (BCML) [44, 45]. In this case, the Pt particles were approximately 6nm and therefore around 20 atomic layers high. Thus, a strain effect was excluded for these particles and made them good candidates for comparison with strained Pt nanoislands on the same surface.

Nevertheless, electrochemical deposition yields a random distribution of catalyst nanoislands, with varying size and spacing. Also the process of developing arrays using electrochemical scanning tunneling microscopy (EC STM) [46] is rather limited due to the small surface area that can be structured by this method (some μm^2). BCML can be used to generate a defined array of catalyst particles, but particles are spherical and their size and distance can only be varied in a small range. In contrast, nanoimprint lithography (NIL) offers several possibilities to establish substrates with a well-defined structure-arrangement, i.e. the different parameters (width, height and spacing of nanostructures) can be varied systematically [47-51]. Thus, in the second part of this thesis novel electrochemical investigations of electrodeposited Pt on a defined array of 160nm-wide Au lines with a spacing of 260nm on an Au surface, established by NIL, are presented. Furthermore, Au pillars, fabricated by nanotransfer printing (nTP), with a cylindrical shape and a diameter of 100nm were characterized electrochemically. Such an array of Au pillars can be coated with Pt via electrochemical deposition. These systems were compared with the randomly distributed Pt nanoislands and spherical nanoparticles on extended Au surfaces. Characterization of the surface structure of the mentioned model systems included the following techniques: X-ray diffraction (XRD), X-ray photoelectron spectroscopy (XPS), cyclic voltammetry (CV), chronoamperometry, electrochemical impedance spectroscopy (EIS) and imaging methods such as EC STM and atomic force

microscopy (AFM). Their electrocatalytic activity was measured by CV and potentiostatic single pulses.

The activity of different electrode structures, conventional extended electrode surfaces and electrodes consisting of defined nanostructure arrays, were finally compared and derived conclusions were interpreted.

This introductory part is followed by chapter 2, which familiarizes with fundamental laws and terms of electrochemistry, such as the electrochemical potential and the electric field at the solid-liquid interface. Furthermore, some basics concerning electrode materials and reactions, investigated for this thesis, are discussed. The fundamental part is complemented by a review of strain, defect density and spillover effect.

In chapter 3 the preparation of used materials, measurement techniques and evaluation methods are described.

Chapter 4 is focused on experimental results, which are discussed in chapter 5: Geometrical properties of the Pt nanoislands and spherical Pt nanoparticles on Au(111), their electrocatalytic activities as well as a comparison of the electrochemical behavior are discussed. Emphasis is put on the interpretation of the results, since this part deals with slightly modified, but conventional and therefore well-known electrode structures. This part is followed by experimental results on defined Au-nanostructure arrays, i.e. nanometer-wide Au lines and Au pillars on Si substrates. Such defined Au nanostructures are meant to be used as support materials for Pt nanostructures. In this case, the demonstration of the applicability of the Au nanostructures in electrochemical systems was emphasized, since this is one of the first approaches to their implementation in electrochemistry. Usually such samples are used as nanostructured semiconductor electrodes for field-effect transistors or solar cells. Thus, focus is put on the discussion of specific properties and the main challenges that had to be overcome for the utilization of these electrodes in an electrochemical system. Finally, electrocatalytic activities of Pt nanostructures on these electrodes are presented and discussed according to their differences to conventional electrode structures.

The thesis is terminated by chapter 6 containing a summary of the main aspects with respect to the different investigated systems and encompassing conclusions.

2 Fundamentals

For a detailed discussion of experimental results it is important to understand the theoretical as well as the experimental background. Therefore, in the following, a brief introduction to electrochemistry will be given and experimental methods to derive fundamental parameters, such as exchange current density of a metal electrode in contact with a redox system, will be introduced. Then, focus will be set on specific electrochemical interfaces, reactions and principles, such as the properties of an Au(111) surface in an electrochemical environment and of metallic catalyst layers or particles on a metal support.

2.1 Electrochemical potential and reactions

Electrochemistry is the science of chemical effects that are caused by an electric field and of electric effects that are due to a chemical reaction. Hence, an electrochemical reaction involves a charge transfer through an interface and thus a flow of current. Such an interface can be composed of various materials. The most well-known electrochemical interface is the metal-electrolyte junction, which will be discussed in the following subsections.

2.1.1 Electrode potential and electrochemical double layer

A galvanic cell consists of two electrically conductive electrodes in an ion-conductive electrolyte. The two electrodes are linked through an external contact, which completes the electric circuit. The discharge of such a galvanic cell implies two electrochemical half-cell or electrode reactions, which, in combination, yield an electronically neutral overall-reaction [52].

Electrode potential

The maximal electric work $nF\Delta U$ performed in the external electric circuit corresponds to the maximal work ΔG that can be achieved for the purely chemical reaction per mole of reactants

$$\Delta G = \Delta H - T\Delta S = -nF\Delta U$$

Equation 2.1.1-1

with molar free energy of reaction ΔG , enthalpy of formation ΔH , entropy of formation ΔS , absolute temperature T , number of transferred electrons n and Faraday constant $F = eN_A$, with elementary charge e and Avogadro constant N_A and potential difference ΔU between the electrodes at open circuit.

For instance, if gaseous chlorine (Cl_2) and hydrogen (H_2) are brought together and the resulting hydrogen chloride dissolves in water to form hydrochloric acid (HCl), the standard free energy of reaction is $\Delta G^0 = -262 \text{ kJ/mol}$. The corresponding standard electrode potential difference is $\Delta U^\ominus = U_{red}^\ominus - U_{ox}^\ominus = 1.36 \text{ V}$ (since $n = 2$) for an electrochemical cell with two metal electrodes, one of them in Cl_2 -purged HCl and the other one in H_2 -purged HCl .

The individual standard electrode potentials $U_{ox,red}^\ominus$ are usually tabulated versus the normal or standard hydrogen electrode (NHE, SHE), which consists of a platinized Pt wire in a solution of hydrogen-purged ($p = 1 \text{ bar}$) acid with an activity of $a_{\text{H}^+} = 1$. Its potential was defined as zero.

Electrochemical double layer

Considering a simple electrochemical system that is not in equilibrium, such as for example a zinc (Zn) electrode, which is brought into contact with a solution containing Zn^{2+} -ions ($\text{Zn} \rightleftharpoons \text{Zn}^{2+} + 2e^-$), either Zn^{2+} -ions are reduced and deposited on the Zn electrode or Zn is oxidized and dissolved into the solution, depending on the energetic relationships. Hence, a potential difference is established between metal and solution phase, which is called an electrochemical double layer, until the system is in equilibrium. If, for instance, Zn^{2+} -ions are reduced and deposited on the Zn electrode until equilibrium is established, the electrode is positively charged and anions are attracted to the metal surface for compensation. In addition, an external voltage could be applied to the Zn electrode and a second electrode, immersed in the solution. By these means, the double-layer charge associated with Zn electrode and solution can be altered, in order to force a greater or minor charge or even change sign of the charges.

According to the Helmholtz model, a description of the (inner) potential decay $\varphi(x)$ with distance x perpendicular to the electrode-electrolyte interface is comparable with the one for a parallel-plate capacitor. This is due to the excess charge of the metal electrode and the counter ions of the electrolyte residing on respective sides of the interface. $\varphi(x)$ can be determined with the one-dimensional Poisson equation

$$\frac{d^2\varphi}{dx^2} = -\frac{\rho}{\epsilon\epsilon_0}$$

Equation 2.1.1-2

with space-charge density ρ , dielectric constant ϵ of the electrolyte and permittivity of the free space ϵ_0 . The charge density between electrode surface and Helmholtz plane, the plane in which the center of the ions nearest to the metal surface is located (compare with Figure 2.1-1), is assumed to be zero [52]. Therefore, Equation 2.1.1-2 equals zero and the derivative of φ over x is constant, yielding a linear decay of $\varphi(x)$.

Although this model is a good approximation for high concentrated electrolytes with a narrow space-charge region, it does not account for the thermal processes in the electrolyte, whose influence changes the properties of the double layer considerably in low concentrated electrolytes. The theory of Gouy and Chapman, who proposed a diffuse double layer, involves a Boltzmann factor for the distribution of the ions of energy $z_i e\varphi(x)$ in the electrolyte (with z_i the charge of ion i) and for the derivation of the space-charge density ρ [53, 54]. It turns out that for small potential difference $\Delta\varphi_{diff} \leq 0.05V/z_i$ in the diffuse double layer, the potential drops exponentially with x . For high potential difference, the expression is more complicated, but still explicitly solvable (compare with e.g. [53], p. 546ff. and [54], p. 39ff.).

Since in the theory of Guoy and Chapman ions were treated as point charges, which can be infinitely close to the metal surface, another modification was made by Stern. It is more realistic to consider the minimum distance of the ions from the metal surface as their ionic radius r . If the ions in the electrochemical double layer are in a solvated state, this distance consists of the ionic radius r and the thickness of the solvation shell s of the ions. The model of Stern therefore results in a combination of Helmholtz and diffuse double layer (compare with Figure 2.1-1).

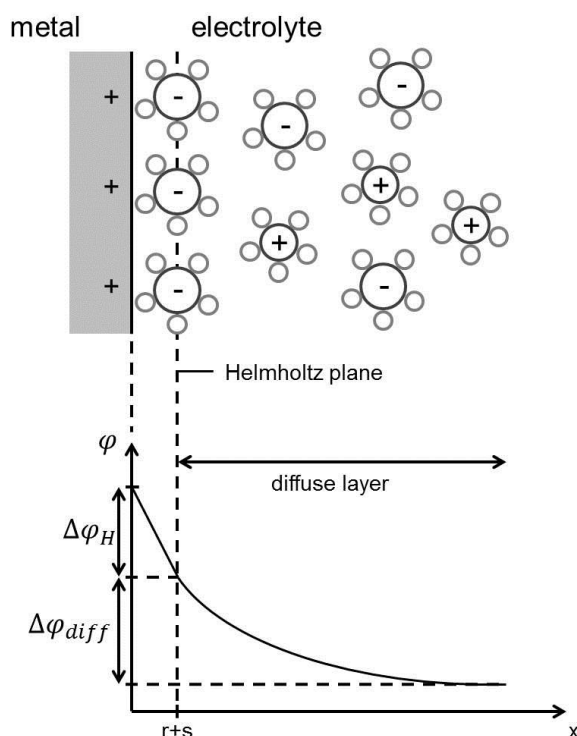


Figure 2.1-1 Schematic of the electrochemical double layer and the potential distribution at a metal-electrolyte interface: The metal is positively charged, thus anions are attracted to the interface. Small circles around the ions represent the solvation shell, since ions in aqueous electrolytes are usually solvated. For simplicity, the water molecules filling all the space between the ions are not shown. The potential φ drops linearly by $\Delta\varphi_H$ in the Helmholtz layer, i.e. from $x = 0$ to the Helmholtz plane and exponentially in the diffuse layer for small $\Delta\varphi_{diff}$.

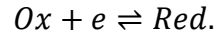
2.1.2 Kinetics of electrode reactions

The previous section was focused on the correlation of electrochemical equilibrium and electrode potential. However, by applying a voltage/potential difference to the electrodes of an electrochemical cell or adding reactants, the equilibrium can be disturbed, which leads to a current flow. The interdependence of current and potential is influenced by the diffusion of reactants in the electrolyte, by chemical reactions and by adsorption/desorption of reactants/products on the electrode surface taking place before and/or after the actual charge-transfer reaction. However, the most fundamental contributor to the current-potential characteristic of an electrochemical system is of course the charge-transfer reaction. The charge-transfer characteristic of an electrochemical system is also referred to as the kinetic regime and its mathematical description is given by the Butler-Volmer formulation of electrode kinetics [53]. Since this thesis focuses on the kinetics of the hydrogen evolution and oxidation reaction at Pt,

the derivation of equations governing charge-transfer characteristics will be discussed in more detail.

Butler-Volmer formalism

In the following, a very simple electrode process, namely a one-step, one-electron reaction will be considered:



Equation 2.1.2-1

The current flow associated with this reaction is closely linked to the rate of the reaction v at the electrode surface. The forward and backward reaction rates v_f and v_b corresponding to this reaction are

$$v_f = k_f C_{Ox}(0, t) = \frac{I_c}{FA}$$

$$v_b = k_b C_{Red}(0, t) = \frac{I_a}{FA}$$

Equation 2.1.2-2

with rate constants $k_{f,b}$, surface concentrations $C_{Ox,Red}(0, t)$ at the electrode-electrolyte interface, cathodic/anodic currents $I_{c,a}$ and surface area A .

Thus, the net reaction rate is

$$v_{net} = v_b - v_f = \frac{I}{FA}$$

and

$$I = I_a - I_c = FA[k_b C_{Red}(0, t) - k_f C_{Ox}(0, t)].$$

Equation 2.1.2-3

Furthermore, the profile of the standard free energy versus reaction coordinate for the above reaction is assumed to have a parabolic shape as shown in Figure 2.1-2. The true shape is dependent on the specific system and not important for the derivation of the general Butler-Volmer equations. Figure 2.1-2 shows the activation energies ΔG_{0c}^\ddagger and ΔG_{0a}^\ddagger at standard electrode potential U^\ominus , when the system is in equilibrium. If the electrode potential is changed by $\Delta U = U - U^\ominus > 0$, the energy of the electron is changed by $-F\Delta U$ and the corresponding activation energy curve is lowered by that amount. The activation energies at potential U are ΔG_c^\ddagger and ΔG_a^\ddagger :

$$\Delta G_c^\ddagger = \Delta G_{0c}^\ddagger + \alpha_c F(U - U^\ominus)$$

$$\Delta G_a^\ddagger = \Delta G_{0a}^\ddagger - \alpha_a F(U - U^\ominus),$$

Equation 2.1.2-4

with transfer coefficient $\alpha_{a,c}$, which depends on the shape of the intersection region. The relation $\alpha_a + \alpha_c = 1$, which is used in many textbooks for these kinds of derivations, only holds for reactants that are not adsorbed on the electrode surface.

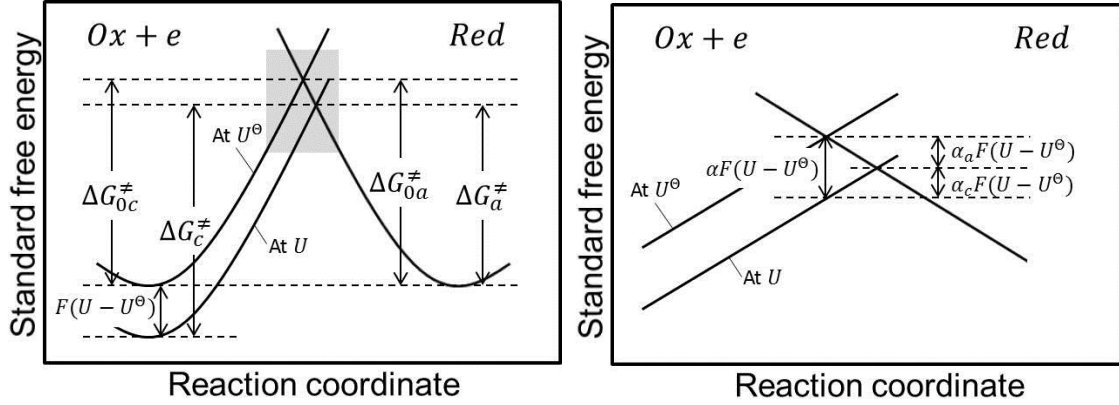


Figure 2.1-2 Schematic curve of the standard free energy versus reaction coordinate for the reaction of Equation 2.1.2-1 at standard electrode potential U^\ominus and any other electrode potential U . The scheme on the right hand side shows the boxed intersection region of the left picture, which is marked in gray.

Now, the rate constants $k_{f,b}$ are modeled by an equivalent to the Arrhenius equation, which is an empirical generalization of experimental findings concerning rate constants of solution-phase reactions. Additionally, Equation 2.1.2-4 is inserted:

$$k_f = A_f e^{-\frac{\Delta G_c^\ddagger}{RT}} = A_f e^{-\frac{\Delta G_{0c}^\ddagger}{RT}} e^{-\alpha_c f(U - U^\ominus)} = k_f^0 e^{-\alpha_c f(U - U^\ominus)}$$

$$k_b = A_b e^{-\frac{\Delta G_a^\ddagger}{RT}} = A_b e^{-\frac{\Delta G_{0a}^\ddagger}{RT}} e^{\alpha_a f(U - U^\ominus)} = k_b^0 e^{\alpha_a f(U - U^\ominus)},$$

Equation 2.1.2-5

with constant factors $A_{f,b}$, rate constants $k_{f,b}^0$ under standard conditions and $f = \frac{F}{RT}$.

Using these rate constants in Equation 2.1.2-3 yields a very general form of the potential-current relation:

$$I = FA[k_b^0 C_{Red}(0, t) e^{\alpha_a f(U - U^\ominus)} - k_f^0 C_{Ox}(0, t) e^{-\alpha_c f(U - U^\ominus)}].$$

Equation 2.1.2-6

In equilibrium, i.e. at a potential U_0 , the net current is zero, which means that anodic and cathodic current are equal. Also, the surface concentrations $C_{Red}(0, t)$ and $C_{Ox}(0, t)$ can

be substituted by the bulk concentrations C_{Red}^* and C_{Ox}^* . With these transformations, the exchange current I_0 can be derived:

$$I_0 = F A k_b^0 C_{Red}^* e^{\alpha_{af}(U_0 - U^\ominus)} = F A k_f^0 C_{Ox}^* e^{-\alpha_{cf}(U_0 - U^\ominus)}.$$

Equation 2.1.2-7

Rewriting Equation 2.1.2-6 with I_0 and overpotential $\eta = U - U_0$, which is the deviation from equilibrium potential, yields the overpotential-current equation

$$I = I_0 \left(\frac{C_{Red}(0, t)}{C_{Red}^*} e^{\alpha_{af}\eta} - \frac{C_{Ox}(0, t)}{C_{Ox}^*} e^{-\alpha_{cf}\eta} \right).$$

Equation 2.1.2-8

A curve exemplifying this relation is shown in Figure 2.1-3. For low overpotentials ($|\eta| \leq 100mV$) the exponential behavior can be seen in the anodic as well as in the cathodic branch. With increasing overpotential, however, the surface concentrations $C_{Red}(0, t)$ and $C_{Ox}(0, t)$ decrease and mass-transfer limitations become dominant. Thus, anodic and cathodic current reach a limiting value I_l at high positive overpotentials ($\eta > 300mV$) and at high negative overpotentials ($\eta < -300mV$), respectively.

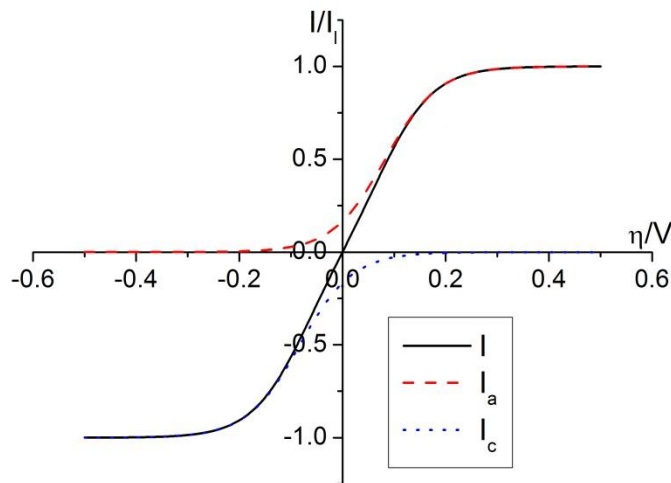


Figure 2.1-3 Overpotential-current curve (solid line) with anodic and cathodic currents (dashed lines) for $\alpha_{a,c} = 0.5$, $T = 298K$, $I_0 = 0.001A$ and $\frac{I_0}{I_l} = 0.2$. With increasing overpotential a limiting current I_l is reached, due to mass-transfer limitation, i.e. decreasing surface concentrations $C_{Red}(0, t)$ and $C_{Ox}(0, t)$ of species Red and Ox.

Special cases

In the special case, in which mass transfer is not limited, the surface concentrations are always equal to bulk concentrations and Equation 2.1.2-8 simplifies to the so called Butler-Volmer equation

$$I = I_0(e^{\alpha_a f \eta} - e^{-\alpha_c f \eta}).$$

Equation 2.1.2-9

A curve corresponding to this equation is shown in Figure 2.1-4 on the left. It is important to note that this equation is applicable to all systems that are not mass-transfer limited but also to the kinetic regime of mass-transfer limited systems. From an experimental point of view, this means that the kinetic currents of the mass-transfer limited system have to be measured. This can be done by e.g. the potentiostatic single pulse technique (for details see section 2.1.3, p. 18ff. and section 3.4.5, p. 53ff.). Current transients measured with this technique can be evaluated according to a theoretical model to yield the kinetic current.

Further special cases are the linear characteristic of Equation 2.1.2-9 for sufficiently small overpotentials ($e^x = 1 + x$ for small x)

$$I = I_0(\alpha_a + \alpha_c)f\eta$$

Equation 2.1.2-10

and the so called Tafel behavior for high overpotentials, for which either cathodic or anodic current are negligible. For instance, at high positive overpotentials, the cathodic current can be neglected and Equation 2.1.2-9 becomes

$$I = I_0 e^{\alpha_a f \eta}.$$

Equation 2.1.2-11

In a Tafel plot the logarithm of the current I is plotted over overpotential η

$$\eta = a + b \cdot \log|I|,$$

Equation 2.1.2-12

with $a = \log |I_0|$ and Tafel slope b . Such a plot shows a linear behavior, as can be deduced from Equation 2.1.2-11. The intersection of this line and the y-axis at $\eta = 0$ is the logarithm of the exchange current I_0 . Furthermore, the transfer coefficients $\alpha_{a,c}$ can be calculated from the slope of the line (compare with Figure 2.1-4). This behavior was first observed by Tafel in HER experiments [3].

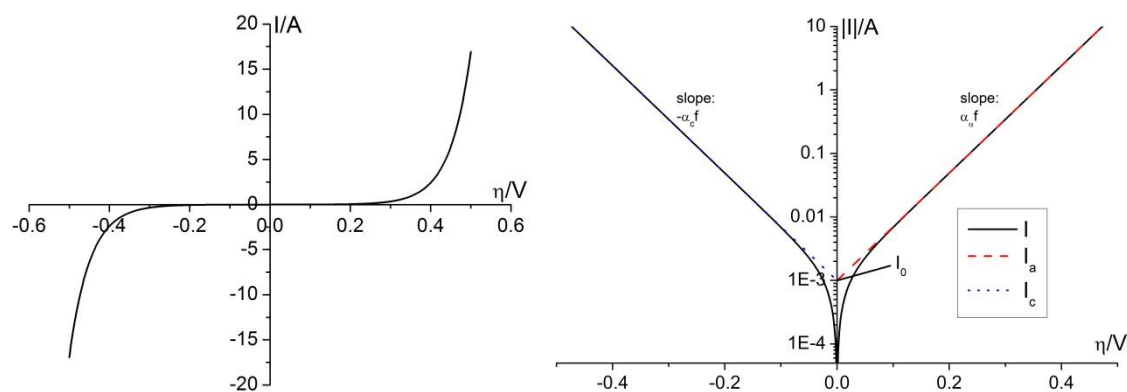


Figure 2.1-4 Left: Overpotential-current curve corresponding to the Butler-Volmer equation, which holds for systems that are not limited by mass transfer. Right: Tafel plots of the anodic and cathodic high-overpotential regimes of the Butler-Volmer equation. The intercept of the current-axis with the linear extrapolation of the Tafel-curves yields the exchange current I_0 and the slope of the lines can be used to calculate the transfer coefficients $\alpha_{a,c}$. (Parameters as in Figure 2.1-3)

Multistep processes

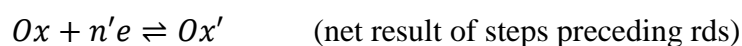
The equations derived in the previous passage are valid for one-step, one-electron processes, such as for example the reaction of potassium ferricyanide to potassium ferrocyanide and vice versa: $Fe(CN)_6^{3-} + e^- \rightleftharpoons Fe(CN)_6^{4-}$. However, many electrochemical reactions require several steps to proceed. This is also the case for the HOR/HER, which was investigated in this thesis: $2H^+ + 2e^- \rightleftharpoons H_2$. Such so-called multistep processes involve several one-electron processes. Thus, the one-step, one-electron equations can often be modified to apply to the multistep process.

In many multistep mechanisms one single reaction is rate determining, because it proceeds much slower than the other reactions. This reaction is referred to as the rate determining step (rds).

As an example, the following overall reaction is considered:



with the partial reactions



and $n = n' + n'' + 1$.

Equation 2.1.2-13

Obviously, the overpotential-current characteristic is determined by the rds. Of course, the additional current, due to the reactions preceding and following the rds, has to be implemented in the corresponding equation. Therefore, if a true equilibrium exists for the overall reaction, Equation 2.1.2-7 can be adapted to the multistep system by assembling it for the rds and multiplying it by the number of transferred electrons:

$$I = n \cdot I_{0,rds} \left(\frac{C_{Red'}(0, t)}{C_{Red'}^{eq}} e^{\alpha_{af}\eta} - \frac{C_{Ox'}(0, t)}{C_{Ox'}^{eq}} e^{-\alpha_{cf}\eta} \right),$$

Equation 2.1.2-14

with exchange current $I_{0,rds}$ and transfer coefficients $\alpha_{a,c}$ of the rds and exchange current $I_0 = n \cdot I_{0,rds}$ of the overall reaction.

However, in order to apply this equation to a particular system, the intermediates' concentrations in equilibrium $C_{Ox',Red'}^{eq}$ and the corresponding time dependence $C_{Ox',Red'}(0, t)$ have to be known or assumed. In most cases, assumptions are made for these parameters, since they are not directly measurable in an experiment. Then the experimental data is compared to different assumed patterns to yield the best accordance. Such a procedure can become quite complex, especially when the intermediates are adsorbed on the electrode surface or when there are several educts and products taking part in the rds.

2.1.3 Electrochemical reactions at constant electrode potential

In the previous section, a general overpotential-current equation was derived (compare with Equation 2.1.2-8) for a one-step, one-electron process. In this equation current is not only dependent on overpotential. It is also related to the dependence of the concentration of the reducing and oxidizing species on the electrode surface $C_{Red}(0, t)$ and $C_{Ox}(0, t)$ on time. Although in some special cases, this dependence can be omitted from the equation, in many systems the surface concentrations vary with time, due to mass transport limitations. Hence, when more reactants at the electrode surface are consumed than the amount that can be supplied by diffusion, a depletion zone develops. In such a case the overpotential-current relation is not easily accessible experimentally. Therefore, potentiostatic single pulses are often used to determine the kinetic current for a certain overpotential. With this technique a constant overpotential is applied to the electrochemical cell via a potential pulse and the corresponding current transient is

measured. The current transient is then used to extrapolate the kinetic current. In this context the time-dependence of the surface concentrations $C_{Red}(0, t)$ and $C_{Ox}(0, t)$ has to be included in the overpotential-current relation.

Therefore, Fick's second law

$$\frac{\partial C_{Ox,Red}(x, t)}{\partial t} = D_{Ox,Red} \frac{\partial^2 C_{Ox,Red}(x, t)}{\partial x^2}$$

Equation 2.1.3-1

with distance x from the electrode surface, concentration $C_{Ox,Red}(x, t)$ and diffusion coefficient $D_{Ox,Red}$ of oxidizing and reducing agents, respectively, has to be solved [9, 53]. The boundary conditions are:

- (i) $t = 0$: $C_{Ox,Red}(0, x) = C_{Ox,Red}^*$
- (ii) $x \rightarrow \infty$: $\lim_{x \rightarrow \infty} C_{Ox,Red}(x, t) = C_{Ox,Red}^*$
- (iii) $x = 0$: $-FAJ_{Ox,Red} = -FAD_{Ox,Red} \left. \frac{\partial C_{Ox,Red}(x, t)}{\partial x} \right|_{x=0} = I$

Equation 2.1.3-2

Here $J_{Ox,Red}$ is the flux of the oxidizing or reducing species, which is related to the concentration gradient and diffusion coefficient by Fick's first law. With flux J the current flow I can be calculated, which in turn can be substituted by Equation 2.1.2-8.

A Laplace transformation of Fick's second law (Equation 2.1.3-1) together with the three boundary conditions (Equation 2.1.3-2), yields the time dependence of the surface concentrations

$$C_{Ox}(0, t) = C_{Ox}^* + \frac{B}{\lambda} (1 - e^{\lambda^2 t} \operatorname{erfc} \lambda \sqrt{t}),$$

$$C_{Red}(0, t) = C_{Red}^* - \frac{\sqrt{\kappa} B}{\lambda} (1 - e^{\lambda^2 t} \operatorname{erfc} \lambda \sqrt{t}),$$

Equation 2.1.3-3

with $B = \sqrt{D_{Red}} \lambda_{Red} C_{Red}^* - \sqrt{D_{Ox}} \lambda_{Ox} C_{Ox}^*$, $\lambda = \sqrt{D_{Red}} \lambda_{Red} + \sqrt{D_{Ox}} \lambda_{Ox}$, $\kappa = \frac{D_{Red}}{D_{Ox}}$,

$$\lambda_{Ox} = \frac{I_0 e^{-\alpha c f \eta}}{FAD_{Ox} C_{Ox}^*} \text{ and } \lambda_{Red} = \frac{I_0 e^{\alpha a f \eta}}{FAD_{Red} C_{Red}^*}.$$

Insertion of these equations (Equation 2.1.3-3) into the general overpotential-current relation (Equation 2.1.2-8) results in the time-dependent current relation

$$I(t) = I_0 (e^{\alpha a f \eta} - e^{-\alpha c f \eta}) e^{\lambda^2 t} \operatorname{erfc} \lambda \sqrt{t} = I_\eta e^{\lambda^2 t} \operatorname{erfc} \lambda \sqrt{t}.$$

Equation 2.1.3-4

An example of such a current transient is shown in Figure 2.1-5.

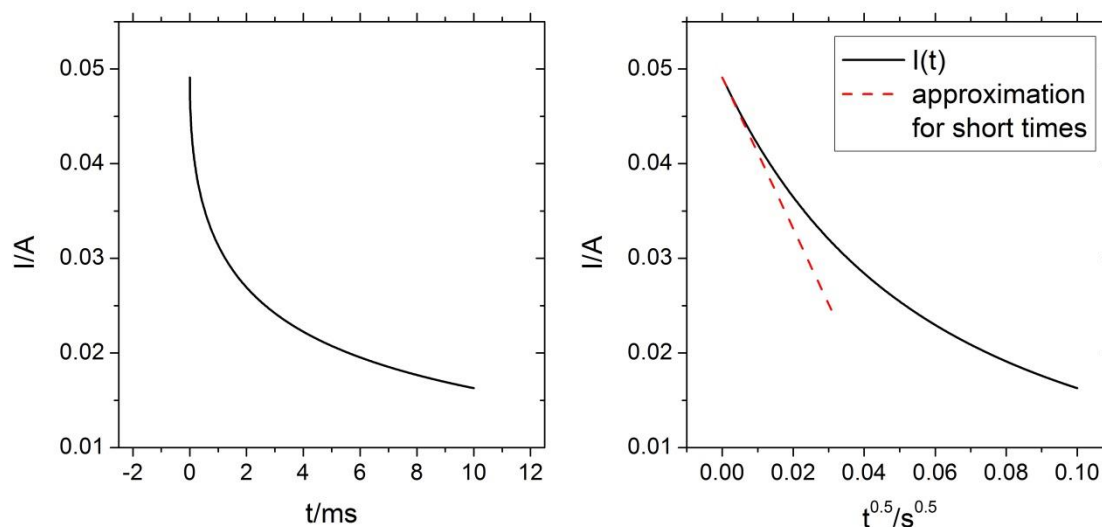


Figure 2.1-5 Current transients corresponding to the time-dependent current relation (black curves; compare with Equation 2.1.3-4) and to the simplified current relation for small times t (dotted red line; compare with Equation 2.1.3-5) calculated with the following parameters: $\alpha_{a,c} = 0.5$, $T = 298\text{K}$, $I_0 = 0.001\text{A}$, $\eta = 0.2\text{V}$, $A = 1\text{cm}^2$, $D_{Ox} = D_{Red} = 5 \cdot 10^{-5} \frac{\text{cm}^2}{\text{s}}$, $C_{Ox} = C_{Red} = 5 \cdot 10^{-6} \frac{\text{mol}}{\text{cm}^3}$.

Two special cases will be considered, because they are important for the evaluation of measured current transients: For short times t ($\lambda\sqrt{t} \ll 1$) the exponential function and the error function $\text{erf}(y)$ can be approximated by the first term of their Taylor series ($e^y = 1 + y + \dots$ and $\text{erfc}(y) = 1 - \text{erf}(y) = 1 - \frac{2}{\sqrt{\pi}}y + \frac{2}{\sqrt{\pi}}\frac{y^3}{3} - \dots$) and Equation 2.1.3-4 simplifies to

$$I(t) \approx I_\eta \left(1 - \frac{2\lambda}{\sqrt{\pi}}\sqrt{t} \right),$$

Equation 2.1.3-5

which is a linear function of \sqrt{t} . This equation is used as a basis for potentiostatic pulse measurements, in which a potential pulse with constant overpotential η is applied to an electrochemical system. The current transient recorded during the potentiostatic pulse is evaluated for short times t according to Equation 2.1.3-5 and yields the kinetic current I_η . Such pulses can be repeated for various overpotentials in order to obtain a Tafel plot and evaluate the exchange current I_0 .

For long times t Equation 2.1.3-4 is

$$I(t) \approx \frac{I_\eta}{\sqrt{\pi\lambda}} \cdot \frac{1}{\sqrt{t}}$$

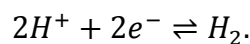
Equation 2.1.3-6

and therefore shows the $\frac{1}{\sqrt{t}}$ behavior of diffusion limited currents, which was confirmed by experiments (see e.g. [55]). The equation purely depends on diffusion polarization since exchange current I_0 and transfer coefficient α can be eliminated from the fraction $\frac{I_\eta}{\lambda}$.

2.2 Selected electrodes and charge-transfer reactions

2.2.1 The hydrogen reactions

The hydrogen evolution reaction (HER) and the hydrogen oxidation reaction (HOR) have been among the most intensely investigated electrochemical reactions since many decades. Hence, one should believe that the reactions are very well understood nowadays. However, in spite of this huge effort to identify the true reaction mechanism, there is much controversy in literature. At a first glance, the HER and the HOR seem to be very simple reactions, as composed of a two-step mechanism with only two different reaction pathways. But it turns out that the reactions take place right at the electrode surface (in the Helmholtz layer) and because of that also depend on electrode material and the state of the surface [54]. The HER and HOR can proceed via two different reaction pathways. The complete reaction is



Equation 2.2.1-1

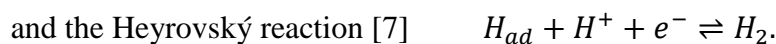
The corresponding elementary steps are



Equation 2.2.1-2



Equation 2.2.1-3



Equation 2.2.1-4

These reactions are valid for acidic electrolytes, but they can be written for alkaline electrolytes in a similar way. The following considerations will be made for acidic media, since the experiments throughout this thesis were performed in acidic electrolytes.

Hence, for hydrogen evolution, the reaction can either proceed via the Volmer-Tafel pathway, consisting of the adsorption of a proton on the electrode surface to form an adsorbed hydrogen atom H_{ad} and the recombination of two adsorbed hydrogen atoms to molecular hydrogen H_2 (forward directions of Equation 2.2.1-2 and Equation 2.2.1-3). The second possibility is the Volmer-Heyrovský pathway, for which the Volmer step is followed by the discharge of a proton at an adsorbed hydrogen atom (forward directions of Equation 2.2.1-2 and Equation 2.2.1-4). For the HOR, the backward directions of the different reactions have to be considered [10, 11].

In the following, the overpotential-current relation is derived for each single step. Mass transport limitations are neglected since this thesis is focused on the kinetic regime where mass transport does not play a role.

For the Volmer step the overpotential-current equation (compare with Equation 2.1.2-14) becomes

$$I_V = I_{0,V} \left(\frac{\Theta(I)}{\Theta_{eq}} e^{\alpha_{a,V} f \eta} - \frac{1 - \Theta(I)}{1 - \Theta_{eq}} e^{-\alpha_{c,V} f \eta} \right),$$

Equation 2.2.1-5

with the exchange current $I_{0,V}$, the transfer coefficients $\alpha_{a,V}$, $\alpha_{c,V}$ of the Volmer reaction and the coverage Θ of adsorbed hydrogen H_{ad} on the electrode surface in equilibrium and dependent on current. The surface concentration of adsorbed hydrogen is proportional to the coverage Θ and thus can be replaced by it.

For the Heyrovský step, the overpotential-current equation is

$$I_H = I_{0,H} \left(\frac{1 - \Theta(I)}{1 - \Theta_{eq}} e^{\alpha_{a,H} f \eta} - \frac{\Theta(I)}{\Theta_{eq}} e^{-\alpha_{c,H} f \eta} \right),$$

Equation 2.2.1-6

with the exchange current $I_{0,H}$ and the transfer coefficients $\alpha_{a,H}$, $\alpha_{c,H}$ of the Heyrovský reaction.

However, these two equations are very general and in this form cannot be compared to experimental results. Therefore, it is convenient to focus on some limiting cases. As an example, this will be done for the HER: The Volmer-Tafel and the Volmer-Heyrovský mechanism can each be assumed with one rds, such that four different scenarios arise.

Furthermore the variation in coverage Θ of adsorbed hydrogen is assumed to be small compared with the variation of the exponential term with overpotential: $\Theta(I) = \Theta_{eq}$. Then, the characteristic of the Volmer(rds)-Tafel mechanism is determined by the Volmer reaction

$$I = I_V = I_{0,V}(e^{\alpha_{a,V}f\eta} - e^{-\alpha_{c,V}f\eta}).$$

Equation 2.2.1-7

For high negative overpotential the equation simplifies to

$$I = -I_{0,V}e^{-\alpha_{c,V}f\eta} \text{ or } \eta = \frac{1}{\alpha_{c,V}f} \ln I_{0,V} - \frac{1}{\alpha_{c,V}f} \ln(-I).$$

Equation 2.2.1-8

with a Tafel slope $b = -\frac{0.06}{\alpha_{c,V}} \frac{V}{dec} = -0.12 \frac{V}{dec}$ (compare with Equation 2.1.2-12; for $\alpha_{c,V} = 0.5$). With the Heýrovský reaction being the rds, the same Tafel slope can be calculated for a transfer coefficient $\alpha_{c,H} = 0.5$.

Thus, Tafel slopes calculated with the assumption of one single rds are not unique, nor are the ones with more than one rds (compare with [10]). Hence, Tafel slopes are not sufficient to determine the reaction mechanism. Moreover, the transfer coefficient can also be different from 0.5, which makes it even more difficult.

It can be concluded that this method is not suitable to identify reaction mechanisms. However, it helps to determine the probability of reaction mechanisms.

2.2.2 The Au(111) surface

Around 50 years ago the preparation of clean and high-quality single crystal surfaces was difficult. Therefore, in the past ten to twenty years, preparation procedures have been refined and well-documented in order to guarantee equal surface quality and to achieve reproducible data [15, 56]. Since this thesis is focused on the electrochemical properties of Pt nanoparticles, it was important to put them on a substrate whose surface structure could be controlled in a systematic way. Hence, the Au(111) single crystalline surface was the substrate of choice.

The structure of an Au crystal is the fcc (face centered cubic) lattice, with a characteristic stacking sequence ABC of two-dimensional hexagonally close-packed layers [15, 57]. The three low-index planes of an fcc crystal are assigned by their Miller indices. The

arrangement of the surface atoms of the (111)-plane is hexagonal (see Figure 2.2-1), square for the (100)-plane and rectangular for the (110)-plane.

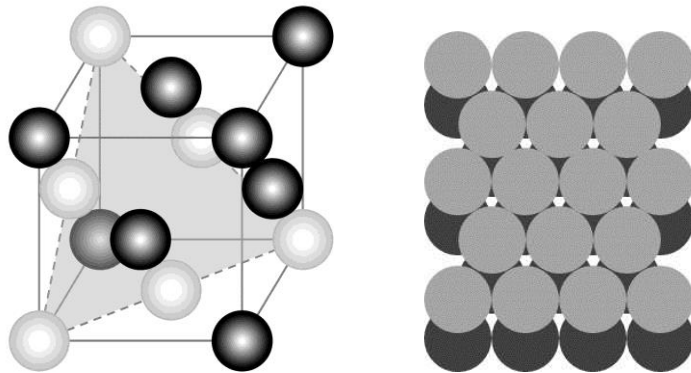


Figure 2.2-1 Scheme of the arrangement of the atoms in an Au crystal. The (111)-plane is indicated in gray (left). The surface atoms of the (111)-plane exhibit a hexagonal pattern (right).

A real crystal never has a perfectly planar surface. Due to inhomogeneities in the bulk and on the surface, defects, such as adatoms, vacancies, islands, holes, monoatomic high steps (height $\sim 0.24\text{nm}$ for Au(111) [58]) and screw dislocations are always present (compare with Figure 2.2-2, left) to a certain extent. On an Au(111) surface two different types of steps can be formed: A (111) or a (100) step (see Figure 2.2-2, right), which is less stable than the (111) step [59].

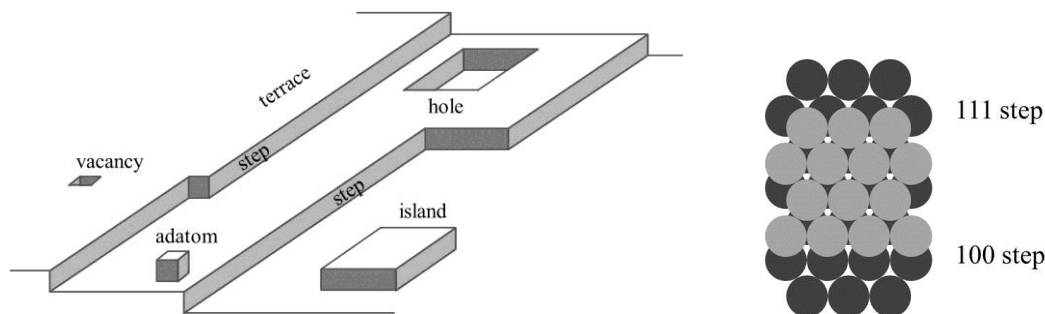


Figure 2.2-2 Left: Different types of defects on an Au(hkl) surface. Right: Two different types of steps can be formed on an Au(111) surface.

When an Au crystal is freshly annealed or kept in vacuum, the position of the surface atoms often differs from the expected ideal crystallographic position: A lateral displacement of the surface layer occurs, which is due to highly asymmetric forces affecting surface atoms, because their coordination number is much smaller than the one of bulk atoms. The surface layer tries to contract in order to increase its coordination, but is stopped by the forces originating from the bulk atoms, which are targeted on a commensurate structure. Hence, atoms can be found at places of lowest surface energy, which is called surface reconstruction. This phenomenon has been extensively

investigated under ultrahigh vacuum (UHV) conditions as well as in electrolytes [58, 60-63]. Au is the only fcc metal, for which reconstruction of the (111) plane occurs. The unit cell of the reconstruction contains 23 instead of 22 atoms of the original crystal lattice; therefore the surface layer is contracted by 4.4%. Due to this misfit of the reconstructed surface layer and the layers beneath a periodic pattern of pairs of parallel lines is formed by the terraces of the surface in $\langle 1\bar{1}2 \rangle$ direction, which separate fcc from hexagonal close packed (hcp) domains. In STM images the atoms of these dislocation lines appear $\sim 0.02\text{nm}$ higher than the surrounding atoms, because they occupy bridge sites instead of threefold hollow sites (compare with Figure 2.2-3). Neighboring pairs of lines have a distance of 6.3nm and the distance between the lines of one pair is 4.4nm .

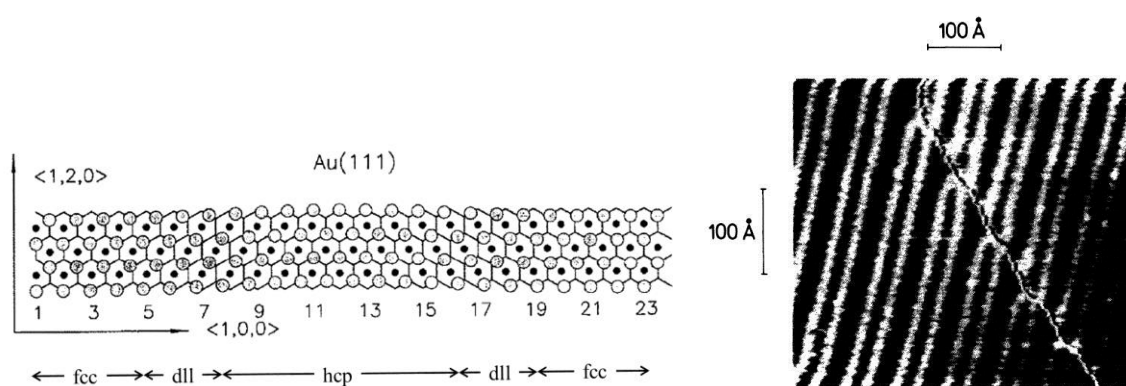


Figure 2.2-3 Left: Scheme of the positions of atoms in the first (empty circles) and second surface layer (solid circles) of a reconstructed Au(111) surface. In fcc and hcp domains atoms of the first surface layer are located in threefold hollow sites, whereas at the position of dislocation lines (dll) they occupy bridge sites. (upper part reprinted, see [64]) Right: STM image of a reconstructed Au(111) surface, which shows the dislocation lines (reprinted, see [65]).

The dislocation lines relieve the stress in the surface layer along the $\langle 1\bar{1}0 \rangle$ direction. However, a zigzag pattern of the paired lines, the so-called herringbone reconstruction, can also occur on wide terraces in order to further minimize the surface energy [60, 63]. As to the interaction of steps and dislocation lines, Repain and coworkers demonstrated that the orientation of dislocation lines perpendicular or parallel to steps depends on the atomic structure of the steps [63]. They found that (111)-microfaceted steps were crossed perpendicularly by the dislocation lines. In contrast to that, the bottom of (100) steps exhibited dislocation lines parallel to the step with lines perpendicular to the upper part of the (100) step (see Figure 2.2-4). These results were interpreted in terms of surface energy, arguing that the reconstruction behavior at (100) steps minimized their step energy.

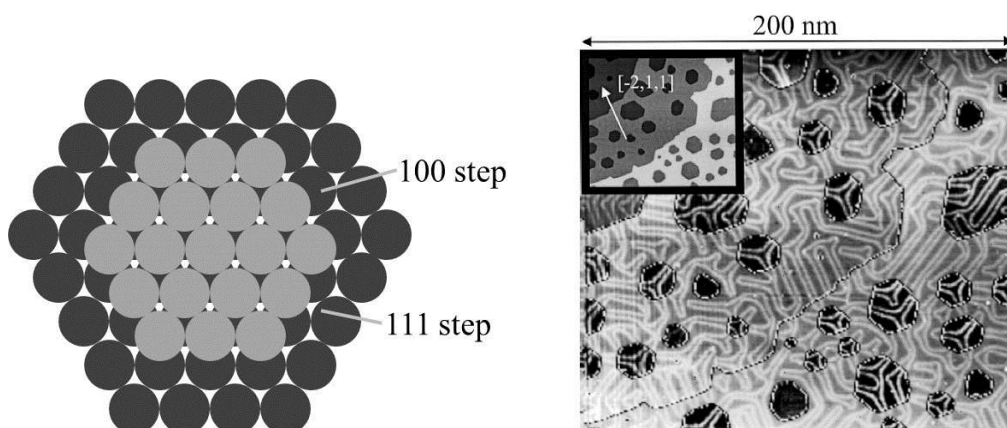
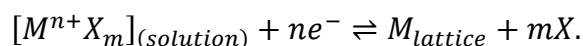


Figure 2.2-4 Left: Scheme of an Au(111) surface with an island and corresponding step orientations. Right: Ultrahigh vacuum scanning tunneling microscopy (UHV STM) image of a reconstructed Au(111) surface pretreated by Ar sputtering (reprinted, see [66]).

Similar observations were made with the EC STM, confirming that the Au(111) surface is also reconstructed in different electrolytes depending on potential. If a reconstructed Au(111) surface is immersed in sulfuric acid the reconstruction can be kept for potentials below 0.5V vs. RHE. At 0.5V vs. RHE the reconstruction is lifted [67] simultaneously with an adsorption of hydrogen sulfate anions, which results in an anodic peak of a CV. At 1.0V vs. RHE a disorder-order phase transition of adsorbed hydrogen sulfate anions occurs [68], which leads to another sharp, anodic or cathodic peak in a CV depending on scan direction. Above a potential of 1.4V vs. RHE surface oxidation sets in, which is accompanied by structural changes due to a high mobility of Au atoms. A similar behavior can be observed in perchloric acid solutions. However, the lifting of the reconstruction does not lead to a sharp peak in a CV, but proceeds more continuously. Oxidation of the surface occurs for potentials higher than 1.2V vs. RHE. Returning to a negative potential of -0.05V vs. RHE for several minutes makes the surface reconstruct again [69].

2.2.3 Metal deposition

If a conductive substrate, such as for example the Au(111) surface, is coated electrochemically by a foreign metal, the process is termed electrocrystallization. The metal M to be electrodeposited is added to an electrolyte solution as a compound containing precipitating neutral molecules and/or ions X (e.g. H_2O , Cl^- , CN^-) [52, 70]:



As described in section 2.1.1, this electrochemical reaction is characterized by a standard electrode potential U^\ominus , or at non-standard conditions by an equilibrium potential U_0 . At a potential $U < U_0$ the reduction reaction, i.e. metal deposition takes place and for $U > U_0$, the oxidation reaction, i.e. metal dissolution happens. In some cases however, when there is no foreign metal present on the electrode surface, metal deposition is possible even for potentials higher than the equilibrium potential. This so-called underpotential deposition (upd) happens, when the chemical potential of the first layer of the deposited metal is much smaller than the chemical potential of the bulk of the deposited metal. This is due to an interaction between the substrate and deposition metal. As examples the deposition of Pb or Cu on Au can be mentioned (see also section 3.4.4.1, p. 51 and section 4.2.1, p. 68ff.).

In detail, electrocrystallization may consist of the following steps [70]: (i) Diffusion of the hydrated metal ion to a position close to the electrode surface (to the Helmholtz plane). (ii) Electron transfer from the electrode to the metal ion and partial or complete dehydration. (iii) Diffusion of the metal atom on the electrode surface. (iv) Incorporation of the metal atom in the lattice of the substrate. In most of the cases deposited metal atoms incorporate into the lattice at sites of high coordination, such as vacancies, steps, islands or holes, which was experimentally and/or theoretically shown for e.g. Pd/Pt on Au(111) [40, 71-74]. Depending on the interaction of the metal atoms M with the substrate metal S the growth mode will be defined [54]: If the interaction between atoms M is stronger than the interaction between atoms M and substrate S, three-dimensional islands will grow on the substrate. This growth mode is called Volmer-Weber or three-dimensional island growth. An example for Volmer-Weber growth is the deposition of Au or Pt on HOPG: The interaction of Au/Pt with HOPG is very small, which leads to three-dimensional particles [22, 31]. In the case, in which the interaction between atoms M and substrate S is stronger than between atoms M, the growth mode still depends on geometric factors. If the crystal lattice of metal M and substrate S do not match, a layer of metal M will be grown on substrate S in a mostly non-pseudomorphic way. Thus, from the second layer on islands will form in order to counterbalance the strain in the first layer. This growth mode is known as Stranski-Krastanov growth. If, however, the mismatch between the two lattices is small, extended layers will be grown on the electrode surface. This growth mode is known as layer-by-layer or Frank-van-der-Merwe growth. In this mode the first few layers will be grown pseudomorphically, until the

lattice relaxes to its bulk value. Finally, the metal atoms M can exchange places with substrate atoms and form an alloy, which occurs for example when Ni is deposited on Au(111). Of course, also growth modes in between the described ones can be found. Considering for example the growth of Pd on Au(111) (lattice constants: $a_{\text{Au}}=0.408\text{nm}$, $a_{\text{Pd}}=0.389\text{nm}$ [75]), where the lattice mismatch is small ($\sim 5\%$), Pd deposits layer-by-layer for two pseudomorphic layers, but then starts to grow islands [72]. Also Pt ($a_{\text{Pt}}=0.392\text{nm}$ [75]) grows pseudomorphically on Au(111) for small coverages below one monolayer and then starts to grow islands instead of a closed layer. Furthermore, these growth modes can be modulated by application of different overpotentials [76, 77]. In general, high deposition overpotential yields a large number of nuclei that arrange randomly on the electrode surface without a strong influence of defect sites. In contrast to that, low deposition overpotential results in a smaller number of nuclei that deposit preferably at defect sites. The influence of the overpotential on the final structure of the deposit was for example shown for the growth of Pt on Au(111) [43, 71]: High overpotential led to three-dimensional particles, which deposited at random sites, whereas low overpotential yielded flat islands which were monoatomic in height and deposited preferentially at defect sites.

2.3 Bimetallic electrocatalysis – Interplay of support and catalyst material

As highlighted already in the introduction, “two-dimensional” Pt islands on Au(111) showed a better performance than bulk Pt in a comparison of the Pt-specific HER/HOR-current densities. Similar activity enhancement was demonstrated for several systems M/S with metal decoration M on bulk metal support S not only for submonolayer coverage but also for complete overlayers: Pd/Au [23-26], Pd/Pt, Pd/Ir, Pd/Ru [78, 79]. However, there are also M/S-systems, which do not show enhanced activities or activity diminishment [30, 31]. These findings were partly predicted, partly modeled after their experimental discovery by theoretical calculations. In the case of the HER for Pd submonolayers on Au(111), calculations by Eikerling and coworkers show that a spillover of adsorbed hydrogen atoms from the catalyst material to the support material can be a reason for the activity enhancement [41, 42]. Another influence on the HER/HOR may arise from defect sites on the support material. As mentioned in the previous section, electrochemical deposition preferably takes place at defect sites, where the electronic

structure of the support material differs from the bulk one. Thus, catalyst particles at these sites exhibit different properties than particles at defect free parts of the support. Finally, the most well-known and in many cases experimentally proven theory is related to the effects of tensile and compressive strain: DFT calculations show that strain in the lattice of metal M alters adsorption energies of reaction intermediates, such that the full multistep reaction is either promoted or constrained [35].

2.3.1 Strain and density functional theory

The strain effect is based on the expansion or compression of a metal decoration on a different bulk support. Via electrochemical deposition or alloying of decoration metals M on or in bulk metals S, a pseudomorphic arrangement of M on/in S can be achieved. Due to the lattice mismatch of both materials, the surface of one or several overlayers M is usually strained, if its height does not exceed a few monolayers and if the lattice constants of M and S deviate only by a few percent. In Figure 2.3-1 compressive and tensile strain is shown for a lattice constant of M exceeding that of S and vice versa.

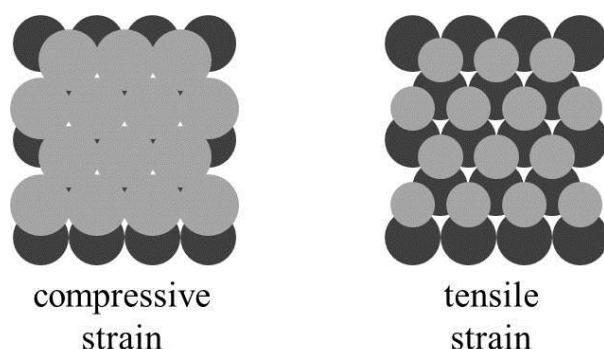


Figure 2.3-1 Different constellations of strain: Compressive strain occurs if the lattice constant of metal M is larger than that of the bulk metal S. The opposite is true for tensile strain, where the lattice constant of the overlayer metal M is smaller than that of the bulk metal S.

In contrast to experiments, the effect of strain on electrochemical reactions is easily implemented in computational methods by simply changing the lattice constant of the corresponding metal layer M to the lattice constant of the support layer S.

These computations rely on density functional theory (DFT) methods, since this approach – although an approximation – allows for the treatment of systems with more than 1000 electrons [80, 81]. DFT studies are ab initio or first-principles calculations, i.e. no experimental parameters are needed as input values. The fundamental simplification that makes such computations possible is the Born-Oppenheimer approximation. For the

investigated systems the motion of nuclei and electrons can be treated separately, because the nuclei move several magnitudes slower than the electrons. Since approximately 1990, DFT has become quite popular in the field of surface science thanks to Hammer, Nørskov and Groß, who focused on the determination of chemisorption energies of various atoms and molecules on different metal surfaces [33, 35, 37-39, 79, 82-84]. Via DFT calculations, ground state electron densities and therefore also ground state total energies are accessible by solving the Kohn-Sham equations, which are one-electron Schrödinger equations [80, 81].

One of the main drawbacks of DFT calculations for electrochemical systems is the impossibility to include the electrode potential in such equations. Further differences between experiment and simulations are temperature, which is 0K in simulations, and vacuum conditions, which are normally used in calculations. However, several groups already try to overcome these difficulties for example by calculating the influence of a water layer containing protons at the electrode surface to compensate for the electrolyte/electrochemical double layer. Additionally, different coverages of adsorbed species or an excess of electrons in the electrode material corresponding to different electrode potentials can be considered [85, 86].

According to the calculations of Hammer, Nørskov and coworkers, the d-band center of a pseudomorphic metal overlayer M on a metal support S shifts up or down, when the lattice constant of M is smaller or larger than the one of S, respectively. In the former case, this is due to a decrease of the local d-band width, which causes an upshift of the d-band center, because the filling of the d-band needs to be maintained (compare with Figure 2.3-2). If then an adsorbate interacts with the strained metal overlayer, the chemisorption bond gets stronger the higher the d-band center of M. This can be concluded from the antibonding adsorbate state appearing above the Fermi level, which is empty and therefore increases the bonding strength [80]. Thus, the strength of an adsorbate's chemisorption bond with a pseudomorphic overlayer M on support S increases in comparison with the chemisorption on bulk metal M, if the lattice constant of metal M is smaller than the lattice constant of the support metal S. The opposite is true for higher lattice constant of metal M with respect to metal S [34, 35, 39, 80, 82].

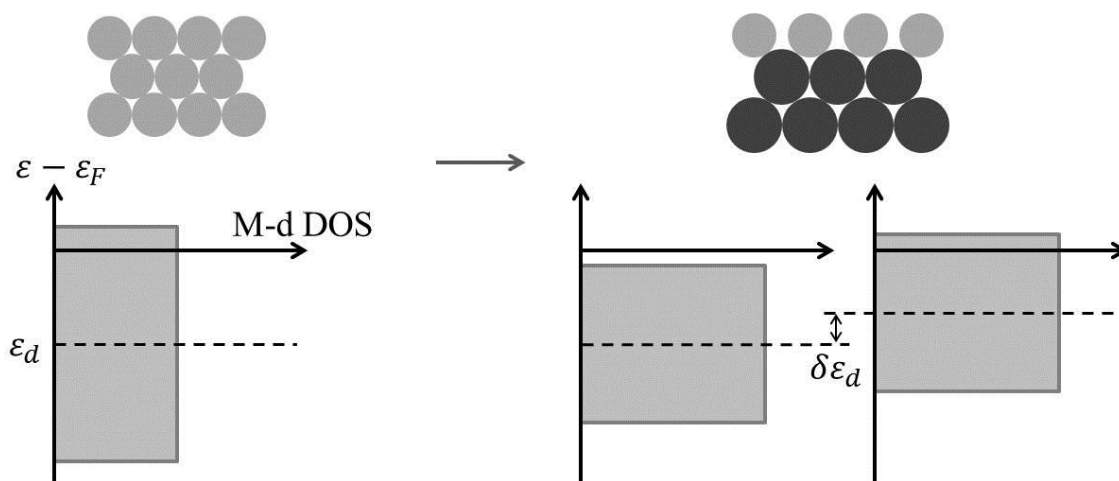


Figure 2.3-2 A metal overlayer M (light gray circles) is deposited pseudomorphically on the surface of metal S (dark gray circles), whose lattice constant is larger than the one of M . The local d -band width of the overlayer M is lowered and the d -band center shifts up in order to maintain the d -band filling.

In order to deduce the correlation of the theory of shifts in d -band centers and reaction rates the Sabatier principle combined with Volcano plots is often taken into account. The Sabatier principle [4] states that reaction intermediates, such as e.g. adsorbed hydrogen atoms in the HER, should neither bind too strong nor too weak on the electrode surface in order to achieve a high activity. The Volcano plot visualizes this principle by relating the exchange current I_0 , which is proportional to reaction rate, to adsorption energy (compare with Figure 2.3-3). For instance the free energy of hydrogen adsorption ΔG_H in the HER was found to be optimum at a value close to zero [34, 87].

Now applying the model of the d -band shifts to a pseudomorphic Pt or Pd overlayer on an Au(111) surface (lattice constants: $a_{Au}=0.408\text{nm}$, $a_{Pd}=0.389\text{nm}$, $a_{Pt}=0.392\text{nm}$ [75]) this means that hydrogen atoms adsorb stronger on the overlayer than on the surface of a Pt(111) or Pd(111) crystal [34]. Taking also the Volcano plot into account the bulk metals should be more reactive than the overlayers, which is schematically shown in Figure 2.3-3 for bulk Pd and a Pd overlayer on Au. Pašti and coworkers came to similar conclusions when studying hydrogen adsorption on Pt and Pd overlayers on the (111)-surfaces of Pd, Pt, Cu and Au for different adsorption sites (threefold hollow, bridge and atop site) [88].

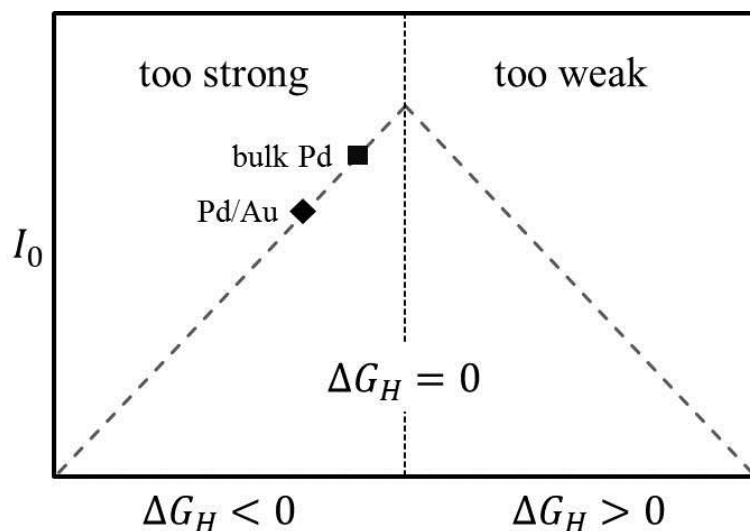


Figure 2.3-3 Scheme of a Volcano plot for hydrogen adsorption: The reactivity is maximum at $\Delta G_H = 0$. Hydrogen adsorption is too strong/weak for negative/positive adsorption energy, respectively.

In spite of this, Björketun and coworkers recently determined adsorption energies varying to a great extent, for hydrogen adsorption on various sites of pseudomorphic Pd_n islands on Au(111). For instance, ΔG_H was close to zero for hydrogen atoms adsorbed on the bridge position of rim sites of large Pd_n islands ($n \geq 3$), whereas hydrogen adsorption on threefold hollow sites of such islands was rather strong ($\Delta G_H \approx -0.3\text{eV}$) [40]. (It is important to note that ΔG_H for the bridge position is calculated taking a full monolayer of hydrogen atoms adsorbed on the threefold-hollow sites into account. This is necessary, because the bridge position would not be filled prior to the threefold-hollow sites, which bind the hydrogen atoms much stronger.)

Thus, such calculations have to be analyzed with care and adapted to specific systems, since the change in adsorption energy strongly depends on adsorbate coverage and the position of the adsorbate.

Hence, it has become clear that strain strongly influences adsorption characteristics. However, any specific system has to be investigated in detail and if possible needs to be compared to experimental data.

2.3.2 Defect density

DFT calculations, as introduced in the previous section, are also quite suitable for the investigation of the theoretical behavior of defined surface structures with particular defect sites. Different types of defect sites were already mentioned in section 2.2.2 and

schematically depicted in Figure 2.2-2 (p. 24). Naturally, not even the highest-quality single crystal is defect free, but exhibits a certain number of defect sites, which are not of the same type. Hence, what is easily done in theory, i.e. to compute the activity of a certain defect site, is impossible in experiments: A single crystalline surface with only one specific type of defect cannot be fabricated.

As a matter of fact, the preparation of well-defined single-crystalline surfaces was quite difficult in the past [15]. Thus, it was not easy to ascribe variations in activity of certain reactions to surface properties. Nevertheless, it has long been assumed and it was also demonstrated in several cases that specific surface sites allow for specific reactions in heterogeneous catalysis [6, 89-92]. One of the first reactions considered structure sensitive was ammonia (NH_3) synthesis on iron (Fe) [93-95]. In this context, Boudart and coworkers reported that the rate of NH_3 synthesis on Fe nanoparticles was dependent on the size of the nanoparticles and that their reactivity could be tuned by a synthesis-gas treatment. Further experiments showed that active sites for C-C, C-H and H-H bond breaking were steps and kinks on Pt(111) surfaces, because of high activities measured at stepped surfaces in comparison with defect poor Pt(111) [96-99]. More recent molecular beam experiments on hydrogen dissociation also show that step sites are more reactive than terrace sites [100, 101].

Similar to heterogeneous catalysis, electrocatalytic reactions were also believed to be site-dependent. However, systematic investigations at single crystalline surfaces exhibiting a majority of specific defect sites, such as (111) steps or kinks, were only performed in a few cases. The rate constant of CO adlayer oxidation in alkaline electrolyte, for instance, was found to increase with increasing number of step sites by comparing different Pt single crystal surfaces with varying number of (110)-step sites, with (100)-step sites and with kink sites [102-105]. The reaction proceeds via an adjacent adsorption of CO and an oxygen-containing species, the two of them forming CO_2 . The step troughs were determined to be the preferential adsorption site for the oxygen-containing species, the adsorbed CO diffusing rapidly on terrace sites in order to react with the oxygen-containing species at the step site. CO adsorbed on step sites was found to be less reactive, probably first converting into terrace species and diffusing to step-bound oxygen-containing species for the reaction to proceed.

Another example for the dependence of an electrocatalytic reaction on defect sites is the HOR and HER on Pd electrodeposited on stepped or defect rich Au(111). Hernandez and Baltruschat [29] found a constant current density during HOR and HER for Pd on stepped

Au(332) as long as Pd coverage was less than one monolayer. At higher coverage the activity decreased. After mechanical damage of the Au(332) crystal, introducing many defect sites at the Au surface, similar measurements showed an increased activity of Pd when compared with the activity of Pd on the non-damaged crystal. The results were interpreted in terms of the role of Pd on defect sites of an Au(111) surface: HOR/HER occurred with rather high activity on these sites, the samples with low Pd coverage, i.e. with a Pd-Au boundary showing the best performance. Also Kibler [23] found a dependence of HER reactivity of Pd monolayers electrodeposited on Au(111) on step density. The current density for HER was measured by CV for a Pd monolayer on Au(111) with a miscut smaller than 1° , i.e. on an Au(111) surface with few defect sites, and for a Pd monolayer on a defect-rich Au(111) crystal with a miscut of 6° . The current density of the Pd monolayer on Au(111) with high step density was approximately a factor of three higher than the one measured at the Pd monolayer on Au(111) with low step density.

Comparable systems were modeled theoretically to a large extent (see also section 2.3.1, p. 29ff.). Thus, in 1998 Mavrikakis, Hammer and Norskov argued that low-coordinated atoms, i.e. atoms of defect sites of a surface, can be compared to the atoms of strained metal layers [82]: The d-band center shifts up in energy with decreasing coordination number and therefore the adsorption energy on such sites is increased. However, theoretical calculations for the energy distribution at a metal deposit on defect sites of a support metal were not done so far. Yet, in a recent publication Björketun and coworkers mention the probability of a much enhanced activity of Pd-Au rim sites for the HER, based on DFT calculations of the hydrogen adsorption energy on a row of Pd atoms on an Au(211) step [40]. Furthermore, they studied the hydrogen adsorption on Pd clusters of different size on an Au(111) surface and determined several sites with free adsorption energy ΔG close to zero, such as e. g. the bridge position between two Pd atoms on the rim of a large Pd island, which forms a (100) step with the Au(111) surface (see Figure 2.3-4).

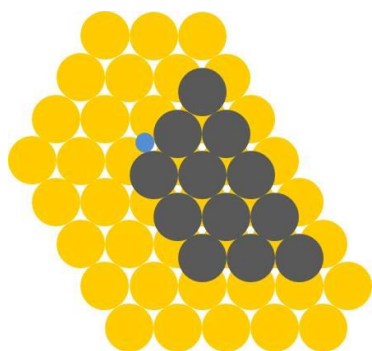


Figure 2.3-4 Hydrogen atom (blue circle) adsorbed at the bridge site of a Pd island (gray circles) on an Au(111) surface (yellow circles). (Hydrogen atoms adsorbed at threefold-hollow sites are not shown.)

With respect to the HOR it might be more important to look at H₂ dissociation on defect rich surfaces. Remarkably, there are several theoretical molecular dynamics/DFT studies on the H₂ dissociation on stepped Pd and Pt surfaces, since these computations are also important for the comparison with experimental heterogeneous catalysis. In this context a higher reactivity of stepped surfaces in comparison with defect poor surfaces was found, which was also demonstrated experimentally [106, 107]. Furthermore, it turned out that (111) steps on a Pt surface are more reactive than (100) steps, with the maximum enhancement factor of three when compared to a defect poor surface [106].

2.3.3 Spillover

Similarly to the influence of defect density on reactivity, the effect of spillover was first observed in heterogeneous catalysis [108-113]. The expression itself probably emerged because of its literal meaning: In linguistics the word spillover is closely related to an excess. This correlation prompts to the fundamental idea of spillover: If a catalytically active surface on an inactive support is fully covered by reactants, additional reactants adsorbing at the catalyst constitute an excess coverage. Under certain circumstances this excess coverage may spill over to the inactive support surface, although direct adsorption on the inactive support surface is inhibited because of too high activation energy (see Figure 2.3-5). Theoretically, spillover is also possible for systems without excess coverage of reactants on the catalyst. In any case the thermodynamic precondition is a high activation barrier for direct adsorption of reactants on the inactive support and a comparably low activation barrier for the transfer, i.e. the spillover, of adsorbed species from the active to the inactive material. This can be an endothermic or an exothermic

process, for which the reactant either adsorbs weaker or stronger on the support, respectively [113].

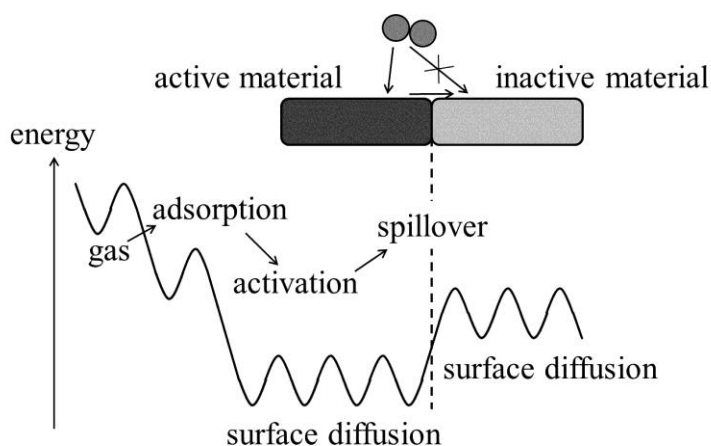


Figure 2.3-5 Scheme of the spillover effect in heterogeneous catalysis. A diatomic molecule in the gas phase diffuses in the bulk and is adsorbed on the catalytically active surface. The adsorbed species diffuse on the catalyst surface, reaching the catalyst-support interface, spillover to the support surface and diffuse there.

Since these prerequisites are also met in several electrochemical systems, spillover was observed in corresponding reactions [114-116]. For instance, Lipkowski and coworkers showed that hydrogen atoms, which were adsorbed on Pt, spilled over to a SiO_x-support surface, thereby considerably increasing the amount of adsorbed hydrogen on the electrode surface [115]. Hence, in most cases an enhanced reaction rate was the origin for the consideration of a spillover effect followed by a detailed investigation of the specific system.

In 2003, Eikerling and Stimming provided a kinetic model for a spillover effect during the HER on a single Pd nanoparticle on Au(111) [41], after the observation of an enhanced reactivity of small Pd nanostructures on Au(111) in comparison with Pd overlayers on Au(111) [25-27]. Their calculations matched experimental results of Meier and coworkers, who studied the influence of height and width of a single Pd nanoparticle on electrocatalytic activity [25, 117]. In 2010 the model was adapted to an extended Au(111) surface with a large number of pseudomorphic Pd nanoislands, generated by electrochemical deposition [42].

The underlying mechanism is comparable to the phenomenon of spillover in heterogeneous catalysis (see Figure 2.3-6): A proton, which is present in the electrolyte, approaches the catalyst, gets adsorbed on the particle by consuming an electron and thus forms an adsorbed hydrogen atom H_{ad} (1, Volmer reaction). The adsorbed hydrogen atom

H_{ad} diffuses on the catalyst surface (2). At the rim of the catalyst surface, it spills over to the support surface (3), where it possibly diffuses (4). It either recombines with a second adsorbed hydrogen atom H_{ad} to form molecular hydrogen H_2 (5a, Tafel reaction), or it reacts to H_2 with another proton, consuming one electron (5b, Heyrovsky reaction). After all H_2 desorbs from the support surface (6).

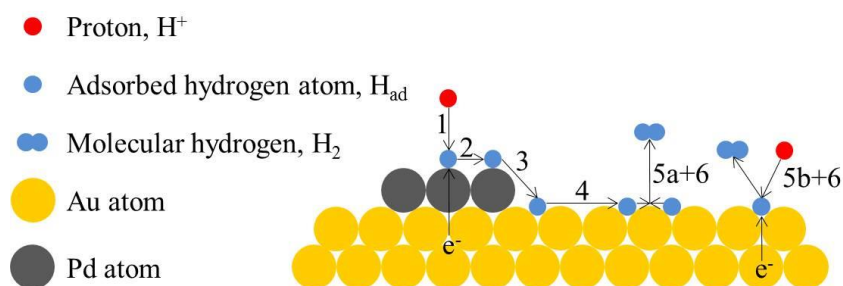


Figure 2.3-6 Scheme showing the spillover effect for the HER on Pd/Au(111): (1) A proton from solution diffuses in the bulk and gets reduced by consuming one electron at the catalyst surface (Pd), forming an adsorbed hydrogen atom H_{ad} . (2) H_{ad} diffuses on the Pd surface and (3) spills over to the support surface (Au). (4) H_{ad} diffuses on the Au surface. (5a+6) Two H_{ad} recombine to molecular hydrogen H_2 , which desorbs from the Au surface. (5b+6) One H_{ad} , a proton and an electron form H_2 , which desorbs from the Au surface.

A closer look on related theoretical values reveals the following correlation: The free energy of reaction ΔG for the Tafel and the Heyrovský reaction occurring on a Pd surface is 0.8eV and 1eV, respectively [118]. The corresponding ΔG for the reactions on an Au surface is 0.5eV and 0.7eV, respectively. These numbers imply that a spillover of H_{ad} from Pd to Au and a Tafel or Heyrovský reaction occurring on Au is probable if the adsorption energy of hydrogen atoms ΔG_H on the Pd surface is at maximum lower by 0.3eV than on the Au surface. The free adsorption energy ΔG_H of H_{ad} on Au is approximately 0.3eV for $\theta_H < 0.1$ [118]. As mentioned earlier, ΔG_H of H_{ad} on Pd is close to zero for specific adsorption sites, such as e.g. the bridge position of rim sites of Pd_n islands [40] (see also section 2.3.1, p. 32). Therefore, spillover is possible from a theoretical point of view.

With this effect catalyst surface sites are freed from adsorbed hydrogen H_{ad} by spillover and can adsorb another proton from solution. Moreover, H_2 desorption from the support is faster than from the catalyst surface due to lower binding energy. Both implications yield a higher total turnover rate and therefore enhance the HER activity.

The kinetic model, established by Eikerling et al. [41, 42], is based on Fick's first and second law in combination with reaction-rate equations, thereby describing the current

flow at the electrode surface. In principle, the model resembles the derivation of the overpotential-current relation, which was described in chapter 2.1.2. However, the spillover model accounts for the surface diffusion of adsorbed hydrogen on catalyst and support surface. Moreover, recombination of adsorbed hydrogen H_{ad} and desorption of molecular hydrogen H_2 via the Tafel step or H_2 desorption via the Heyrovský step is implemented (see also chapter 2.2.1 for reaction steps, p. 21f.). Thus, the calculation is very complex and was numerically solved in the case of the Volmer-Tafel path [41, 42]. The equation for the Volmer-Heyrovský path was solved analytically. The ideal radius of a circular Au surface surrounding a catalyst particle with a radius of 1-3nm was calculated to be between 30nm and 40nm. Experimental results could be reproduced for measurements on single Pd nanoparticles as well as for Pd nanoislands on an extended Au(111) surface by fitting theoretical curves to experimental values. In the latter case, accordance of experiment and theory was only achieved for the Volmer-Heyrovský mechanism. Several kinetic parameters were determined, such as the rate constant of hydrogen adsorption on the catalyst surface and the rate constant of the Heyrovský reaction on the support surface. They varied with Pd-nanoparticle/nanoisland size and were in line with the idea of spillover effect. Hence, the rate constant of H_2 desorption from the catalyst surface was much higher for a large Pd particle compared with a small one, demonstrating that most of the produced H_2 desorbed from the catalyst instead of the support surface. Thus, spillover was diminished at the large particle [41].

In principle, such a mechanism is also imaginable for the HOR on Pd/Pt nanostructures on Au(111) (compare with opposite pathway of Figure 2.3-6): H_2 transforms into H_{ad} via the Tafel or the Heyrovský pathway (6+5a/b), H_{ad} diffuses on the Au surface (4) and spills over to the Pd surface (3). H_{ad} diffuses on the Pd surface (2) and, by losing one electron, it desorbs as a proton (1). Thermodynamic prerequisites, such as an energetically favorable hydrogen dissociation on the Au(111) surface, were shown to hold for particular defect sites on an Au(111) surface and on Au clusters [119]. However, this mechanism implies that free defect sites are available on the Au(111) surface to dissociate molecular hydrogen. Since Pd and Pt preferably deposit on defect sites of an Au(111) surface, spillover is only possible at very low Pd/Pt coverage or at very high defect density on the Au surface. Hence, spillover during HOR is not only determined by the radius and spacing of catalyst structures on the Au surface, as in the case of HER, but additionally by the number and type of defect sites on the Au surface.

3 Materials and methods

3.1 Equipment and consumables

X-ray photoelectron spectroscopy (XPS) measurements were performed at Paul Scherrer Institute (PSI) using a VG ESCALAB 220iXL spectrometer (Thermo Fisher Scientific) equipped with a twin anode X-ray source (Mg K_{α} , Power: 300 Watt). The spectra were recorded in constant analyzer energy mode at a pass energy of 20 eV for high resolution acquisition of core level spectra. The XPS system was calibrated using the Ag $3d_{5/2}$, the Cu $2p_{3/2}$ and the Au $4f_{7/2}$ lines of sputter cleaned samples as reference signals. The data was evaluated using the Avantage software (v. 4.43, Thermo Fisher Scientific). EC STM measurements were performed with a PicoSPM base (Molecular Imaging), which was equipped with a Nanoscope IIIA controller (Veeco) and a bipotentiostat/galvanostat BP600 (EC-Tec). Therefore, a Teflon ring was fixed on the sample surface, which was then filled with electrolyte. Tips were prepared by etching a gold wire (Carl Schaefer, 99.99%) in HCl (32%, Merck, extra pure) and covering it with Apiezon wax (Plano). For tapping mode AFM investigations a Multimode EC STM/AFM system (Veeco) and n-doped Si cantilevers (Bruker) with a nominal tip radius of 8nm were used. All electrochemical measurements, except EC STM measurements, were carried out in glass cells with a standard three electrode configuration. An Autolab potentiostat (PGStat30N, Deutsche METROHM) provided potential and/or current control. For HOR-/HER-potentiostatic pulses on the Pt nanoislands on defect-poor/-rich Au(111) (see section 4.2, p. 67) a home-made potentiostat was used together with a function generator (Agilent Technologies) and an oscilloscope (Tektronix Inc.). Any glassware was cleaned in peroxymonosulfuric acid (Caro's acid) and rinsed and boiled in Milli-Q water (18.2M Ω cm, TOC<2ppb, Merck Millipore). Au wires (Carl Schaefer, purity: 99.99%), and for Cu underpotential deposition (Cu upd) a Cu wire (Alfa Aesar, Puratronic, purity: 99.9999%) were used as counter electrodes. A mercury sulfate electrode (MSE, Hg/Hg₂SO₄/SO₄²⁻ (0.1M K₂SO₄), Schott) in 1M sulfuric acid (H₂SO₄), was used as a reference electrode for electrochemical measurements in 1M perchloric acid (HClO₄) in glass cells ($E_{MSE(1M)}=0.675V$ vs. SHE). Only for Pt deposition, another MSE in 0.1M H₂SO₄ ($E_{MSE(0.1M)}=0.720V$ vs. SHE) was utilized. In the case of EC STM an oxidized Au

wire in 0.1M HClO₄ served as reference electrode ($E_{\text{Au}/\text{Au}_2\text{O}_3} \approx 1.25\text{V}$ vs. SHE). Working electrodes, which are described in more detail in section 3.2 (p. 40), were covered with a Teflon tape (CMC Klebetechnik) with a circular hole to guarantee a defined surface area. Contact was established with a gold wire on the WE surface, which was also covered by the Teflon tape. Only in the case of Au pillars on highly doped Si surfaces, the samples were contacted on the rear side of the sample. This side was treated with a drop of HF to remove the natural oxide and coated with silver paste. The Au wire was positioned on the silver paste to establish an Ohmic contact. Electrolytes were prepared with Milli-Q water and the following chemicals: H₂SO₄ and HClO₄ (96% and 70%, Merck, suprapur), potassium hexachloroplatinate(IV) (K₂PtCl₆) (Sigma Aldrich, purity: 99.99%) and copper sulfate (CuSO₄) (Alfa Aesar, purity: 99.999%). Pt micelles were fabricated with PS(1850)-b-P2VP(900) diblock copolymers (Polymer source Inc.), toluene (J.T. Baker, VLSI Grade, purity: >99.5%) and Potassium trichloro(ethylene)platinate(II) hydrate (K[PtCl₃(C₂H₄)]·H₂O, Zeise's salt) (Sigma Aldrich, Product No. 244953). Used gases were: Argon (Ar) and hydrogen (H₂) (4.8 and 5.0, Linde) and carbon monoxide (CO) (4.7, Messer Griesheim).

3.2 Support material

3.2.1 Gold films on glass

The working electrodes used for investigations on Pt nanostructures on Au(111) (see chapter 4, p. 57) consisted of a 250±50nm thick Au layer on 2.5±1.5nm chromium (Cr) on borosilicate glass (Dr. Schröer, Arrandee). The preferential orientation of these Au layers is 111, which is confirmed by X-ray diffraction (XRD) measurements. The samples were annealed with a Bunsen burner at about 900°C for several minutes until a light orange color was observed and then cooled with a drop of Milli-Q water in Ar atmosphere. The procedure was repeated three times. This yielded flat Au(111) islands on the surface of the sample, which consisted of single-crystalline domains, limited by grain boundaries. Each sample was then cycled in Ar-purged 1M H₂SO₄ between 0.33V and 1.08V vs. SHE (scan rate 0.1V/s) until a stable voltammogram was obtained. Within this potential range the reconstruction was lifted and peaks for the SO₄²⁻-phase transition at Au(111) terraces occurred at about 1V vs. SHE, as expected from literature data [62, 120]. The procedure was repeated in Ar-purged 1M HClO₄ between -0.08V and 0.92V vs.

SHE (scan rate 0.1V/s) to make sure that neither the Au surface nor the electrolyte were contaminated by impurities. Such samples are referred to as non-oxidized or defect-poor Au(111) and/or marked by a polarization current $I_p=0$ in the discussion of the electrocatalytic activity of Pt nanoislands on defect-poor and defect-rich Au(111) (section 4.2, p. 67ff.)

In order to generate a defect-rich Au(111) surface the sample was oxidized via a galvanostatic pulse for 5s at a current of 0.15A in Ar-purged 1M HClO₄ in a separate cell. The oxide was reduced via cyclic voltammetry (CV) and two more cycles were applied in the potential range of 0.04 to 1.76V vs. SHE (scan rate 0.1V/s). The CV was stopped at a potential where the Au surface was in a reduced state. These samples are in the following referred to as oxidized and reduced or defect-rich Au(111) and/or marked by a polarization current $I_p=0.15A$. Oxidation and reduction of Au surfaces is extensively discussed in literature [121-128]. It was shown that such surface treatment leads to an increased number of step and defect sites.

Since the pretreatment without galvanostatic oxidation yielded Au(111) surfaces with comparably low defect density, these samples are referred to as non-oxidized or defect-poor Au(111) surfaces and/or marked by a polarization current $I_p=0$.

3.2.2 Nanostructured gold surfaces

In the case of the nanostructured electrodes (see also chapter 4.4) working electrodes were boron (B) doped Si wafers (p/boron, (100), resistance: <0.002Ωcm, Si-Mat) with a very thin native oxide layer (~2nm) and Au nanostructures on top. The samples were fabricated in a clean room. Si wafers were cleaned with acetone and isopropanol (both solvents: Avantor Performance Materials B.V.) in an ultrasonic bath before the actual nanostructuring process.

In order to generate polymer lines on Au, a thin titanium (Ti) layer (4nm) followed by a 20nm-thick Au layer (Au: Permion, purity 99.999%, Alfa Aesar; Ti: purity 99.99%, Lesker Evaporation Materials) was either thermally (chamber pressure $\sim 10^{-6}$ mbar) or e-beam (chamber pressure $\sim 10^{-7}$ mbar) evaporated on the Si wafer. The thin Ti layer was necessary for adhesion of the Au layer on the substrate. A polymeric imprint resist (mr8010; Microresist Technologies) was then spin coated on the Au surface within 30s with 3000rpm. After thermal curing at 120°C for 2min, the resist layer was 100nm thick. This resulted in a 100nm-polymer/20nm-Au/4nm-Ti/2nm-SiO₂/Si structure [51]. Such

samples were utilized for nanoimprint lithography (NIL). The corresponding principle is depicted in Figure 3.2-1. A Si mold (dimensions 1cm x 0.5cm; IMS Chips), fabricated via e-beam lithography and consisting of 60nm wide lines with a spacing of 250nm, was functionalized by a self-assembled monolayer (SAM) in order to improve the hydrophobicity of the surface and thus provide a good delamination. Substrate and mold were placed on top of each other on the sample holder of the nanoimprinter (2.5 inch Nanoimprinter, Obducat). This stack was covered with aluminum foil and inserted into the pressure chamber of the nanoimprinter. The NIL process was started with an initial heating-up of the sample to 165°C, followed by the direct application of a pressure of 35bar for 7min. Subsequently, the mold-substrate stack was cooled down to a temperature of 80°C at a constant pressure of 35bar for about 5min. As soon as these two process steps were finished the stamp-substrate stack was taken out of the system. Then the mold was separated vertically from the substrate resulting in a grating in the polymer on top of the sample structure (compare with Figure 3.2-1). The residual layer was etched down by a brief oxygen plasma treatment according to previously calibrated etching rates. Since this is an isotropic process, the vertical etching of the polymer was accompanied by a lateral etching making the imprinted trenches wider while narrowing the spacing between two neighboring trenches. This method yielded ~100nm wide and ~75nm high polymer lines with a spacing of ~250nm on the Au surface. Acetone and isopropanol (chromasolv, Sigma Aldrich) were utilized to dissolve the polymer lines when needed.



Figure 3.2-1 Principle of nanoimprint lithography (NIL): The substrate is coated with a polymeric resist. A mold is pressed into the resist (a) to yield an imprinted pattern (b). By oxygen plasma etching, residues are removed (c).

For nanotransfer printing (nTP, compare with Figure 3.2-2), another Si mold (dimensions 0.3mm x 0.3mm, IMS Chips) with cylindrical pillars (diameter ~100nm, spacing ~200nm, height ~40nm) was functionalized with a SAM and coated with a 20nm thick Au layer followed by a 4nm thick Ti layer. The Au/Ti surface and the Si substrate were treated with an oxygen plasma to improve the adhesion of the metal structures on the Si surface. Substrate and mold were placed on top of each other on the sample holder of the nanoimprinter, covered with Al foil and inserted into the pressure chamber. At first, a

pressure of 30bar was applied for 1min and temperature was raised to 200°C at 30bar for 4min. After this process the mold-substrate stack was separated immediately. The back side of the nanostructured Si sample was treated with hydrofluoric acid (HF, 5%, BASF) and coated with a silver paste for electrical contact.

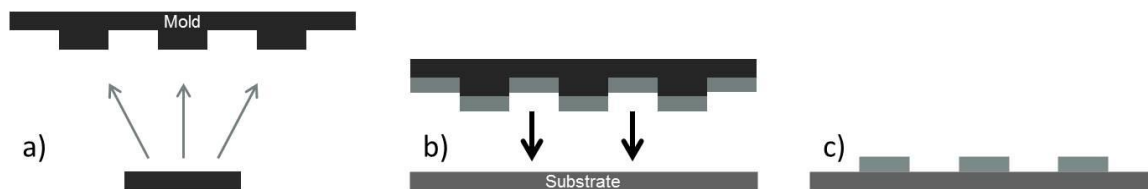


Figure 3.2-2 Principle of nanotransfer printing (nTP): The mold is coated with a metal (a) and pressed on a Si substrate (b), yielding metallic nanostructures on the Si surface (c).

3.3 Deposition of platinum islands and particles on gold

3.3.1 Electrochemical deposition

Electrochemical deposition of a metal is not only determined by elementary electrochemical steps such as diffusion, desolvation, electron transfer, nucleation and growth, but also by material properties such as crystal lattice constants or step/defect density. Furthermore, there are various procedures to electrochemically deposit a metal on another. In the case of Pt deposition on Au surfaces from 0.5mM K_2PtCl_6 + 1M $HClO_4$ electrolyte, the deposition potential is determined by two reactions: First, the Pt^{4+} -ion reacts to a Pt^{2+} -ion ($PtCl_6^{2-} + 2e^- \rightleftharpoons PtCl_4^{2-} + 2Cl^-$) at $U^\ominus = 0.74V$ vs. SHE, then the Pt^{2+} -ion reacts to metallic Pt ($PtCl_4^{2-} + 2e^- \rightleftharpoons Pt + 4Cl^-$) at $U^\ominus = 0.73V$ vs. SHE [129]. Theoretically, at a standard electrode potential U^\ominus of $\sim 0.73V$ vs. SHE the system is in equilibrium and no deposition happens. At a potential negative of U^\ominus deposition takes place and positive of U^\ominus Pt is dissolved. The equilibrium potential for the mentioned electrolyte concentration (0.5mM K_2PtCl_6 +1M $HClO_4$) was not known and therefore determined experimentally. Before and after the deposition routine was started, a potential of 1.12V vs. SHE was applied to the Au surface to make sure that no deposition occurred. After the deposition procedure the electrode was removed from the electrolyte, extensively rinsed with Milli-Q water and transferred to another electrochemical cell. Nevertheless, when **dipping** the Au electrode into the electrolyte at 1.12V vs. SHE and removing it immediately, a very small amount of Pt can be detected on the Au surface

with further characterization methods (for characterization techniques see section 3.4.4, p. 51ff.).

However, **cyclic voltammetry (CV)**, i.e. application of a triangular voltage and simultaneous recording of the current flow, at an Au(111) surface in 0.5mM K_2PtCl_6 + 1M $HClO_4$ electrolyte shows that deposition can only be detected at potentials below approximately 0.65V vs. SHE in the first negative scan (compare with Figure 3.3-1). The sample was immersed in the electrolyte at 1.12V vs. SHE and the CV was started with the negative scan (black curve). At 1.0V vs. SHE the $[PtCl_6]^{2-}$ -complex was most probably reduced to $[PtCl_4]^{2-}$, which is indicated by a negative peak [71]. Only at potentials smaller than 0.65V vs. SHE the $[PtCl_4]^{2-}$ -complex was reduced to metallic Pt. This may be due to the high stability of the adsorbed $[PtCl_4]^{2-}$ -complex on the Au surface [71]. The overpotential for Pt deposition is reduced, when Pt is already present on the surface, which can be seen from the negative current in the positive scan (red curve), in which deposition took place up to a potential of 0.8V vs. SHE.

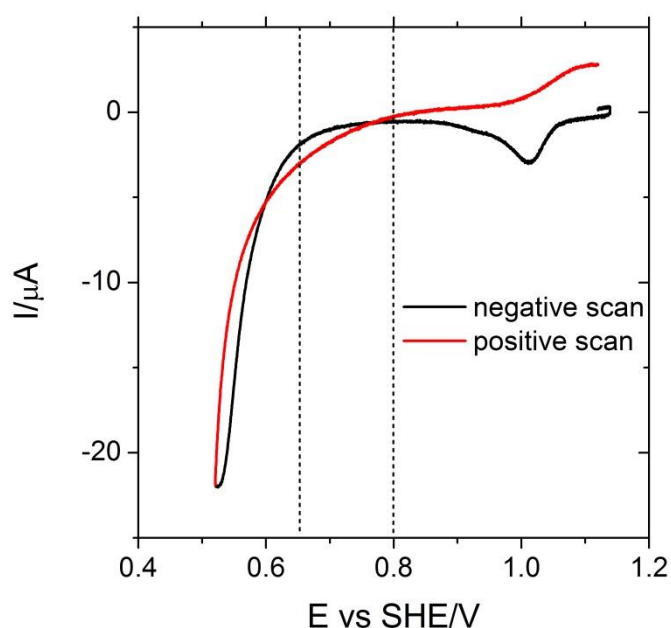


Figure 3.3-1 Pt deposition by cyclic voltammetry: CV at an Au(111) electrode in 0.5mM K_2PtCl_6 + 1M $HClO_4$ with a scan rate of 0.05V/s. Initially, deposition overpotential is relatively high, since Pt is only deposited negative of 0.65V vs. SHE, which can be seen from the negative scan. In the positive scan a negative current can be detected up to a potential of 0.8V vs. SHE. Thus, deposition overpotential is decreased, once Pt is present on the Au(111) surface. (The negative peak at 1.0V vs. SHE is probably due to the reduction of the adsorbed $[PtCl_6]^{2-}$ complex to $[PtCl_4]^{2-}$ [71].)

To effectively control the deposition process with regard to deposition rate/sites, number and size of deposited particles, either potentiostatic single or double pulse deposition is used. For **single pulse deposition**, the sample is immersed into the electrolyte at 1.12V vs. SHE. Then, a certain deposition overpotential η_{dep} is applied for a defined time t_{dep} and the potential is returned to 1.12V vs. SHE. In this case deposition overpotential η_{dep} can be chosen such that Pt preferably deposits at step/defect sites or at terrace sites. The higher deposition overpotential η_{dep} , the higher the number of Pt particles and the higher the fraction of particles, which deposit at terrace sites.

For **double pulse deposition**, the sample is again immersed into the electrolyte at 1.12V vs. SHE. Then, a first nucleation pulse with a rather high nucleation overpotential η_{nuc} , is applied for a very short nucleation time t_{nuc} , in order to generate a defined number of Pt nuclei on the Au surface. After that a comparably small growth overpotential η_{gro} is applied for a growth time t_{gro} . This procedure is advantageous when a defined deposition on Au terrace sites is pursued. Since Pt preferably grows at the Pt nuclei established in the nucleation process, the growth overpotential can be chosen such that deposition happens in the diffusion limited regime, i.e. all particles grow with the same velocity and are therefore very similar in size (for more details see [32]).

Whenever the deposition current was monitored, the corresponding charge flow could be calculated and was related to the amount of Pt present on the electrode surface. Pt deposition charge was estimated as $q=840\mu\text{C}/\text{cm}^2$ per Pt monolayer because of the Pt^{4+} state in the deposition solution.

In any case, the electrolyte was purged with Ar to remove all oxygen from the electrolyte, which was not stirred during the deposition process.

3.3.2 Micellar technique

Complementary to electrochemical deposition, hexagonally ordered Pt nanoparticle arrays were fabricated on Au(111) by diblock copolymer micelle lithography (BCML) [44, 45, 130, 131]. Whereas with electrochemical deposition randomly distributed Pt nanoislands with a height of one to about three atomic layers are formed on the Au(111) surface [43], with BCML an ordered array of spherical Pt nanoparticles is generated. Using this method, a variation in particle diameter is possible in the regime of 1-15nm by loading the micelles with different amounts of Pt-precursor. Additionally, the spacing of

the particles can be varied from 30 to 140nm by using diblock copolymers with different lengths of the blocks.

At first, poly(styrene)-*block*-poly(2-vinylpyridine) (PS-*b*-P2VP) diblock copolymers were dissolved in toluene at a concentration of 20g/l. Here, the PS block is preferentially dissolved and the P2VP is nearly insoluble. The solution was stirred for one week, resulting in the formation of spherical reverse micelles (compare with Figure 3.3-2). These micelles were treated with Zeise's salt ($\text{K}[\text{PtCl}_3(\text{C}_2\text{H}_4)] \cdot \text{H}_2\text{O}$) as a metal precursor with a loading factor of 0.5 and stirred for another week. The $[\text{PtCl}_3(\text{C}_2\text{H}_4)]^-$ ions were bound as counterions in the polar core of the micelles by protonating the pyridine units. The solution was then mixed with anhydrous hydrazine in dry toluene at which the $[\text{PtCl}_3(\text{C}_2\text{H}_4)]^-$ ions were reduced to form one Pt particle in each micelle. The size of the particle was controlled by the original amount of $[\text{PtCl}_3(\text{C}_2\text{H}_4)]^-$ ions in the core of the micelle, which was equal in all micelles.

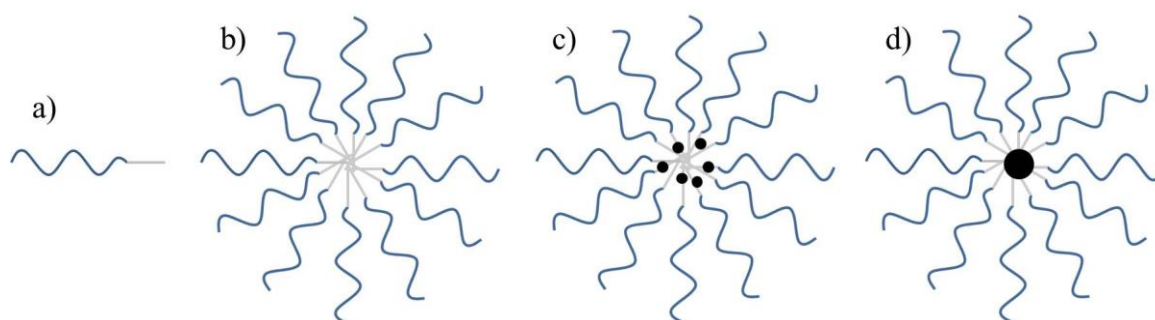


Figure 3.3-2 Diblock copolymers (a) form spherical reverse micelles (b), when dissolved in toluene. Then micelles are loaded with a metal precursor (c), which is reduced by adding hydrazine to the solution and forms one metal particle in the center of a micelle (d).

Au(111) supports were then dipped into the micellar solution at 90mm/min, pulled out at 7mm/min and dried in air. A hexagonally ordered micellar monolayer remained on the Au(111) surface (compare with Figure 3.3-3). Pt nanoparticles were formed by treating the micelle-decorated substrates with an H_2 plasma for 90min at 160W and 0.8mbar chamber pressure.



Figure 3.3-3 A hexagonally ordered micellar monolayer is established on the substrate after dipping it into the micelle solution (a). By a plasma etching step with H_2 , nanoparticles are formed on the substrate (b).

Furthermore two samples were subjected to a heat treatment for better adhesion of the Pt particles: The samples were placed in a RTP (rapid thermal processing) oven at 300°C in oxygen atmosphere. Sample #1 was not annealed, sample #2 was annealed at this temperature for 10s and sample #3 for 10min. The samples were cooled down in oxygen atmosphere. Before HER/HOR measurements, the samples were subjected to an activation procedure, i.e. mild oxidation and reduction via CV (for more details see chapter 4.3, p. 79ff.), to remove impurities from the sample surface.

With this procedure spherical Pt particles with a diameter of about 6nm and a spacing of 60nm were established on the Au(111) surface.

3.4 Characterization techniques

3.4.1 X-ray photoelectron spectroscopy

By XPS the chemical composition of the first few atomic layers of a surface can be detected [132]. A sample is irradiated with monoenergetic soft X-rays in vacuum, which interact with atoms in the surface region ($\approx 1-10\mu\text{m}$), and the energy of the emitted electrons is analyzed. The resulting spectrum is composed of the number of detected electrons per energy interval and their kinetic energy. Each element has a characteristic spectrum. Since the mean free path of electrons in solids is quite small, detected electrons originate only from the first few atomic layers. Quantitative data can be obtained by analyzing peak heights or areas. Concerning this thesis, however, identification of chemical states was important, which is possible through exact measurement of peak positions and separations and comparison with literature data.

In section 3.2.1 (p. 40ff.) the fabrication of a defect-rich Au(111) surface was discussed. The oxidation-reduction sequence applied in this context was a rather severe treatment of the electrode surface. Therefore, it was necessary to exclude that any oxide remained on the surface after reduction. Otherwise the defect-poor and defect-rich Au(111) surface hardly could have been compared, due to a different surface composition.

Thus, three different samples were prepared for XPS [133] according to the description in section 3.2.1: One sample was annealed and cycled in 1M H_2SO_4 and 1M HClO_4 in the double layer regime. This sample was not oxidized ($I_p=0$). A second one was pretreated like the one before and additionally oxidized and reduced ($I_p=0.15\text{A}$). A third sample was

pretreated like the first one and then galvanostatically oxidized only, i.e. the oxide was not reduced.

3.4.2 Scanning probe microscopy

In 1981 Binnig, Rohrer, Gerber and Weibel introduced their concept of vacuum tunneling through an adjustable gap between a metal tip and surface, which led to the establishment of the first STM in 1982 [134, 135]. The underlying principle is to scan a metal tip over a conducting surface with a distance of a few Ångström [136]. A voltage is applied between tip and surface resulting in a tunneling current I_t , which occurs due to the quantum mechanical tunneling effect, when tip and surface are close enough. The STM can be operated in the constant current mode, in which the tunneling current is used to adjust the separation between tip and sample surface and therefore an image of the electronic structure of the surface is generated. Since I_t is exponentially dependent on the separation and the work function of the sample surface, a very high resolution, in the best case atomic resolution, of the corresponding images can be reached. If the work function is constant the topography of the sample surface is imaged, as in the case of metals.

In 1986, the invention of atomic force microscopy [137] and electrochemical scanning tunneling microscopy [138-140] followed.

Electrochemical scanning tunneling microscopy (EC STM)

An EC STM operates identically to an STM, but a small electrochemical cell resides on the sample side, which is composed of a compartment filled with electrolyte on top of the sample surface, a reference and a counter electrode. A tip is dipped into this compartment and the potential at tip and sample, which are both working electrodes, as well as the voltage between these electrodes is controlled by a bipotentiostat, together with counter and reference electrode. To inhibit a substantial faradaic current flow through the tip, it is insulated with wax and only the very top of the apex is left uncovered to detect the tunneling current.

For EC STM measurements samples were pretreated and in several cases coated with Pt as described in section 3.3.1 (p. 43ff.). Pt surface area was analyzed by hydrogen adsorption only (see section 3.4.4.1, p. 51ff.) to image a surface very similar to the one used for electrocatalytic activity measurements. Each sample was fixed on a sample holder together with a Teflon ring, which was then filled with 0.1M HClO₄, to cover the sample surface. If not stated otherwise, the working electrode (WE) potential was

$U_{WE}=0.4V$ vs. SHE, the tip potential was $U_{tip}=0.5V$ vs. SHE. Thus, the applied potential difference between WE and tip was $\Delta U=0.1V$, with a tunneling current of $I_t=1nA$ in constant current mode.

Tapping mode atomic force microscopy (TM AFM)

Comparable to STM, for AFM a cantilever with a tip is scanned over the investigated surface. This surface, however, can also be an insulator or a semiconductor, since the operation principle is based on the forces between tip and sample surface. Depending on the particular configuration, mechanical contact forces, van der Waals forces, capillary forces, chemical bonding, electrostatic forces etc. are measured to monitor the surface. If this force is kept constant, the distance between tip and sample is maintained. The deflection of the cantilever is measured through a laser reflected from the back side of the cantilever onto an array of photodiodes. If the system is operated in tapping mode (TM), an alternating voltage is applied to the cantilever, which oscillates at nearly its resonance frequency. The forces between sample and tip influence the amplitude of this oscillation, which is measured and kept constant by adjusting the distance between sample and tip. In this way an image of the sample topography is generated.

If the features that are imaged and the tip radius are of approximately same size/diameter, the lateral resolution suffers from convolution. This is for example the case when imaging spherical Pt nanoparticles on an Au surface with a radius of about 10nm with a tip that has a radius of 8nm. Deconvolution of tip and particle shape can only be done, when the tip shape is known, which was not the case in the presented measurements. However, the detected height is not influenced by such a convolution.

3.4.3 Electrochemical impedance spectroscopy

Electrochemical impedance spectroscopy (EIS) is used to determine various properties of an electrochemical system by applying an alternating voltage, which is added to the electrochemical potential between working and reference electrode, and monitoring the corresponding current and phase shift. This is usually done with a frequency response analyzer (FRA) and the impedance Z is calculated. The frequency of the ac voltage or the electrochemical potential can be varied. When operated at a potential where faradaic reactions take place the charge-transfer resistance and therefore the exchange current can be evaluated. However, for this thesis frequency-dependent EIS at potentials in the double-layer regime was used.

In the double layer regime, an electrochemical cell can be modeled by a resistor R , which represents the Ohmic resistance R_{Ω} , in series with a capacitor C , which represents the double-layer capacitance C_{DL} [53]. If an ac voltage with various frequencies is applied to such an electric circuit, the dominating element in the high frequency regime is the resistor R and in the low frequency regime it is the capacitor C . Such a measurement can be presented either in a Bode or in a Nyquist plot (see Figure 3.4-1), from which R_{Ω} and C_{DL} can be determined. In a Bode plot, the logarithm of the absolute value of the impedance Z , $\log|Z|$ and the phase angle ϕ are plotted against the logarithm of the frequency $\omega=2\pi f$. In a Nyquist plot the imaginary part of the impedance Z'' is plotted against the real part Z' . In this plot, R_{Ω} corresponds to the value at the Z' -axis for $Z''=0$. In a Bode plot R_{Ω} is the value resulting from an extrapolation of the linear regime of the $|Z|$ curve at high frequencies ($10^5 s^{-1} - 10^7 s^{-1}$) to the $|Z|$ axis. C_{DL} is determined by evaluation of the slope of the linear regime of the $|Z|$ curve in the Bode plot at low frequencies ($1 s^{-1} - 10^3 s^{-1}$).

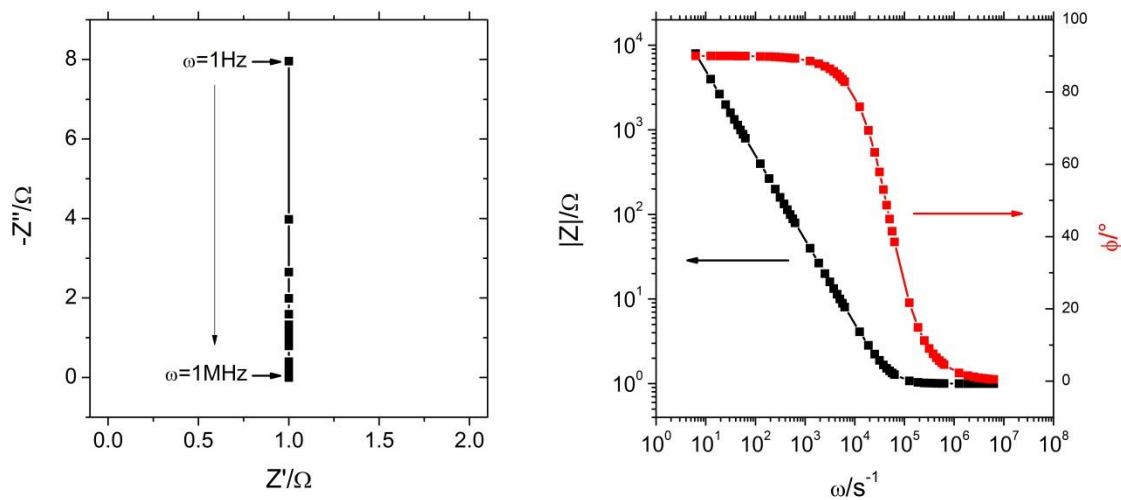


Figure 3.4-1 Example of a Nyquist (left) and corresponding Bode plot (right) for an EIS measurement of an electrochemical cell with an electrolyte resistance $R_{\Omega}=1\Omega$ and a double-layer capacitance of $C_{DL}=20\mu F$ in a frequency range from 1Hz to 1MHz. ($\omega \approx 6.3s^{-1} - 6.3 \cdot 10^6 s^{-1}$).

Frequency-dependent EIS was performed in Ar-purged 1M $HClO_4$ at different potentials in the double-layer region, $U=0.33V$, $0.23V$ and $0.13V$ vs. SHE, in a frequency range from 1Hz to 1MHz. A single sine wave with an amplitude of 0.01V was applied. With such measurements the Ohmic resistance of the electrolyte R_{Ω} was measured, as well as the double layer capacitance C_{DL} . These values were used to identify the time range, in

which double layer charging dominated the current flow during potentiostatic pulse measurements (see also section 3.4.5, p. 53ff.).

3.4.4 Cyclic voltammetry

Cyclic voltammetry (CV) is the most common technique in electrochemistry for the characterization of electrode surfaces. A triangular voltage is applied between the investigated, so called working electrode (WE) and the reference electrode (RE). Simultaneously, the current flow through the WE is measured. This results in a voltage-current plot, which shows characteristic features depending on the types of processes happening at the WE surface, such as ad- and desorption, oxidation or reduction. When the properties of an investigated sample change, the CVs may show different characteristic features, which can be interpreted in terms of e.g. crystal structure or size of nanoparticles present on the surface.

In this work, CV was mainly applied to determine the Au and Pt surface area of the various samples that were investigated. The general procedure is to integrate the measured current for a specific process, such as deposition or reduction of an oxide, over time, which yields the corresponding charge flow. This charge can be compared to literature values and related to a certain surface area. The Pt coverage will be given as a certain fraction of one monolayer (ML) throughout the experimental sections. This fraction is calculated by relating the Pt surface area to the geometric surface area of the electrode, for Pt nanoislands, which are one atomic layer in height as well as for Pt nanoparticles, which are several atomic layers in height. Hence, in the case of “two-dimensional” Pt nanoislands a Pt coverage of x monolayers means that a fraction of $(1-x)$ of the electrode surface is not covered by Pt. However, in the case of three-dimensional Pt nanoparticles, more than the fraction of $(1-x)$ of the electrode surface is not covered by Pt. If not denoted otherwise, any CV measurements were conducted in 1M HClO₄ with a scan rate of 0.1V/s.

3.4.4.1 Ad/desorption-, oxidation- and reduction-charge evaluation

One of these processes was **Cu underpotential deposition** (Cu upd), which was used to determine the Au surface area of several samples. The expression underpotential deposition is chosen for a deposition that starts at a potential positive of the corresponding equilibrium potential U_{eq} , where normally dissolution of the component would take place

(compare with section 2.2.3, p. 26). The standard potential in this case is 0.35V vs. SHE [129]. However, deposition already starts at 0.66V vs. SHE, since Cu atoms are more strongly bound to Au than to Cu itself [141] (and references therein). Via CV in 10mM CuSO₄+1M H₂SO₄ between 0.30V and 0.96V vs. SHE (scan rate 0.02V/s) Cu was deposited and subsequently dissolved. From the shape of the CV the potential at which one monolayer of Cu is present on the Au surface can be clearly determined [142, 143]. At that potential the scan direction was reversed and the monolayer was dissolved again. The corresponding charge was evaluated and related to a charge density $q=440\mu\text{C}/\text{cm}^2$ per monolayer Cu.

Another means to determine Au surface area is **Au oxidation**. Au oxidation starts at about 1.2V vs. SHE, when scanning in positive direction. The oxidation regime exhibits one or more peaks, depending on the properties of the Au surface (crystal orientation, defect density) [15]. Then, current decreases to a minimal value at $U_{\text{min}}\approx 1.7\text{V}$ vs. RHE until Au oxidation continues and oxygen evolution starts, which is reflected in a steeply increasing current. The charge in the first oxidation regime (double-layer corrected) can be related to $q=400\mu\text{C}/\text{cm}^2$, when integrating from the beginning of Au oxidation to U_{min} [144]. This relation was found by Burshtein and coworkers by varying electrode size, electrolyte temperature and sweep rate. They stated that in the corresponding potential range chemisorption of one oxygen atom per Au atom takes place.

Au_yO_z reduction can also serve as a (qualitative) measure for Au surface area, which was analyzed by comparing the charges of Au oxidation and reduction regimes of several Au electrodes with different geometrical surface area. Au oxidation occurs between 1.24V vs. SHE and U_{min} (~1.7V vs. SHE), the potential of the local minimum after the first oxidation peak(s). Au_yO_z reduction occurs between 1.36V and 0.91V vs. SHE. The variation in Au-reduction charge was in line with the variation in geometrical surface area ($q\approx 400\mu\text{C}/\text{cm}^2$). However, when the polarization potential is increased into the regime of further Au oxidation and oxygen evolution reaction (OER), Au-reduction charge also increases, whereas Au-oxidation charge in the first oxidation regime stays constant. Therefore, Au-oxidation charge is more accurate and reliable for the determination of Au surface area.

Additionally to the evaluation of the Pt coverage by the deposition current, the Pt coverage on the different Au surfaces was determined via evaluation of the charge flow during hydrogen ad- and desorption, CO-adlayer oxidation and PtO_x reduction. These methods are very well suited for the determination of the Pt surface area, since CO and

hydrogen only adsorb on Pt, not on Au, and PtO_x reduction is clearly separated in terms of potential range from Au_yO_z reduction.

For **CO-adlayer oxidation**, CO was adsorbed on Pt at $U=0.16\text{V}$ vs. SHE by purging the electrolyte with CO for 10min. Afterwards, the electrolyte was purged with Ar for 40min to remove CO. Starting from 0.16V the potential was then cycled in the negative direction from 0.16V to 0.04V and in positive direction from 0.04V to 1.56V vs. SHE (scan rate 0.1V/s). Initially, the whole Pt surface was covered by CO, which can be inferred from the complete suppression of hydrogen adsorption in the first scan. The adsorbed CO was oxidized between 0.7V and 1.4V vs. SHE. In the second cycle, hydrogen adsorption and desorption could be observed again and did not change during three additional CVs, which proves that any adsorbed CO was completely oxidized in the first scan. Pt coverage was evaluated by subtracting the current in the second scan from the current in the first scan for same potentials and integrating the resulting current. The calculated charge was related to surface coverage due to values established by Friedrich et al., who found an increasing CO coverage per unit area with decreasing Pt-particle size [145].

To determine the charge flow during **hydrogen ad-/desorption**, the current in the potential range from 0.1V to 0.36V vs. SHE was integrated after subtraction of double-layer current. This charge was related to $q=205\mu\text{C}/\text{cm}^2$ per Pt monolayer, which was measured for a bulk Pt(111) crystal.

When cycling Pt/Au-electrodes in a potential range from 0.05V to 1.55V vs. SHE, **PtO_x reduction** occurs in a potential range from 0.91V to 0.41V vs. SHE, which is well separated from Au_yO_z reduction, occurring in a potential range from 1.36V to 0.91V vs. SHE. The charge under the PtO_x -reduction peak (double-layer corrected) was related to $q=440\mu\text{C}/\text{cm}^2$ per Pt monolayer for a maximum polarization potential of 1.55V vs. SHE [146].

3.4.5 Potentiostatic single pulse technique

The potentiostatic single pulse technique was already theoretically discussed in section 2.1.3 (p. 18ff.). It is a very useful technique for the investigation of electron transfer reactions that are hampered by diffusion limitation, such as the HOR. By application of potentiostatic single pulses, it is possible to evaluate the kinetic current for the HOR. Another advantage of this technique is that high overpotentials can be applied without destroying the electrode because of the short pulse times, which are typically in the range

of milliseconds. Thus, such measurements are also suited for HER investigations. There is, however, also a difficulty: When applying a potentiostatic pulse the first response of an electrochemical system is the double layer charging current. Therefore, it is necessary to evaluate involved time constants carefully: The current response of an electrochemical system, which is due to double layer charging, can be modeled by a resistor, which represents the electrolyte, in series with a capacitor, which represents the electrochemical double layer (compare with section 3.4.3, p. 49ff.). The time-dependent current of such an RC-circuit caused by a voltage pulse U_{0a} is $I(t) = I_{0a}e^{-t/\tau}$, where $I_{0a}=U_{0a}/R$ and $\tau=RC$. The time t when $I(t)$ is negligibly small, i.e. when the capacitor/the electrochemical double layer is nearly completely charged, has to be considered. For example if $t=6\tau$, 10τ or 20τ , the current has decayed to $I(t)=0.0025I_{0a}$, $4.5 \times 10^{-5}I_{0a}$ or $2.1 \times 10^{-9}I_{0a}$, respectively. Therefore current transients were only analyzed in the time regime after $t=6\tau$ for the studies presented in section 4.1(p. 57ff.) and after $t>10\tau$ in section 4.2 (p. 67ff.); these values depended on system parameters such as working electrode size.

Furthermore, HOR- and HER-current transients for corresponding overpotentials $|\eta|$ were compared. The HER is hardly affected by diffusion limitation, because of the high amount of protons in the electrolyte used for such measurements and the rather high mobility of protons ($\mu = 3.6 \cdot 10^{-3} \frac{cm^2}{Vs}$ in water [147]). Thus, the HOR and HER curves are very similar in the double-layer regime, but differ from a certain time t_{kd} , when in the case of HOR pronounced diffusion limitation sets in (diffusion coefficient of H_2 in H_2SO_4 : $D = 3.7 \cdot 10^{-5} \frac{cm^2}{s}$ [148]). Then, the HOR current is kinetically and diffusion controlled, whereas the HER current is approximately constant and predominantly controlled by kinetics. The HOR current keeps on decaying until the concentration of H_2 at the electrode surface is zero, at which the current is exclusively diffusion controlled. Evaluation of the HOR-current transients was therefore done after time t_{kd} .

Both methods, i.e. consideration of the double-layer charging behavior and comparison of HER- and HOR-current transients, were applied to find an appropriate time regime for the derivation of kinetic currents. By these means an evaluation of the double-layer charging current instead of the kinetic current could be prevented.

HOR/HER-activity measurements were performed via potentiostatic single pulses with positive and negative overpotentials, respectively, in 1M $HClO_4$, which was purged with

H₂ for at least 10min (compare with [133]). In the case of HOR the pulse duration was 2ms, for HER it was either 5 or 50ms.

HOR/HER-current transients were analyzed and the kinetic current was evaluated with the method discussed in section 2.1.3 (p. 18ff.). The current was plotted versus the square root of time and fitted in its linear region to yield the kinetic current from the intercept of the fit, with $t=0$ at the current-maximum I_{0a} (compare with Figure 3.4-2), i.e. the signal-rise time was not included in the evaluation. The linear fit was performed in a time slot $\Delta t \approx 50\mu\text{s}$ after the double-layer charging current had decayed to a negligible value and before diffusion limitation completely controlled the current response.

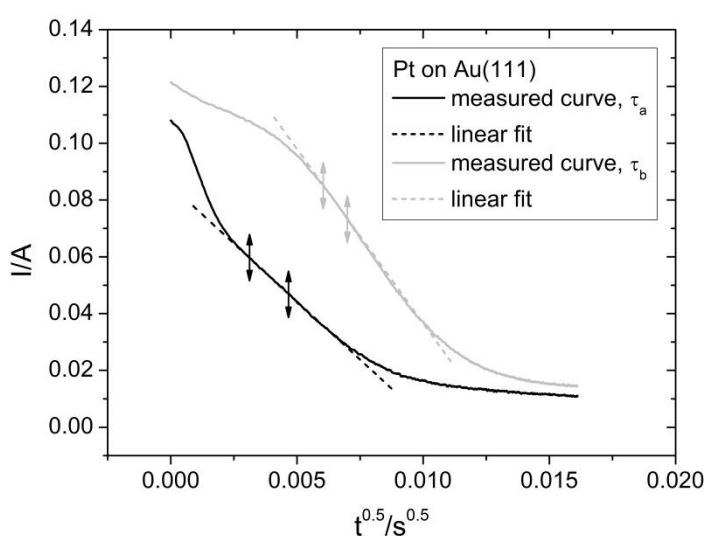


Figure 3.4-2 $t^{0.5}$ -current graph for the HOR corresponding to a potentiostatic single pulse at an overpotential $\eta=0.2V$ (without iR -correction) at different electrodes consisting of Pt nanoislands on Au(111) in 1M HClO₄ for different time constants τ : $\tau_a < \tau_b$. Kinetic current was evaluated from this plot through a linear fit between $t_1 > 10\tau_{a,b}$ and t_2 . The regime is indicated by two arrows per curve and the linear fit as a dashed line.

Double-layer charging behavior was determined with EIS (see section 3.4.3, p. 49ff.): via Ohmic resistance R_Ω and double layer capacity C_{DL} assuming an equivalent circuit consisting of R_Ω and C_{DL} in series, the RC-time constant $\tau=R_\Omega C_{DL}$ was calculated. However, EIS data was not always absolutely reliable concerning R_Ω , because of some scatter in the high-frequency regime, which is dominated by the Ohmic drop in the electrolyte. Therefore, these data were double-checked by evaluation and comparison of the peak currents $I_{0a}=U_{0a}/R_\Omega$ for selected potentiostatic pulses and corresponding potentials U_{0a} . In some cases the Ohmic drop evaluated by EIS had to be replaced by the value calculated by comparison of peak currents I_{0a} . The corresponding error was then set

as the discrepancy between EIS and pulse data. To make sure that double-layer charging current I_{DL} was negligibly small the linear fit was started at $t_1 \approx 6\tau$ or 10τ .

The HER-current transients evaluated for Tafel plots shown in section 4.2.3 (p. 76ff.) were analyzed via averaging the measured current in a time regime from 2ms to 3ms after starting the potentiostatic pulse, where it was nearly constant.

The HOR- and HER-current densities evaluated by these two different methods differ in most of the cases: HER-current densities are normally smaller than HOR-current densities, which can be due to a higher activity of Pt for the HOR. A comparison of current densities found in the presented studies with literature data also shows, that absolute current densities differ. However, absolute current densities are influenced by many factors, such as e.g. the quality of the single-crystalline surface, the measurement routine or the applied potential range. Apart from potentiostatic pulses, measurement routines like slow CV in a very small overpotential regime (often referred to as “micropolarization”) or rotating ring disc measurements (for details see e.g. [149]) are also frequently used in electrocatalysis [19].

4 Results

As already pointed out in chapter 1, there have been many studies on the hydrogen reactions for Pt nanostructures on Au. However, the question of the true reaction mechanism and of the origin of an enhancement of Pt activity is still not fully answered. The latter is addressed in this thesis: the influence of spillover, strain and defect-density effect on the HOR and the HER at Pt on Au is investigated, with the aim to separate spillover effect and verify its theoretically predicted and experimentally assumed existence.

4.1 Platinum nanoislands on Au(111) – Variation of deposition sites and coverage

In the following, investigations of the electrocatalytic activity of Pt nanoislands, which were electrochemically deposited on Au(111) by various deposition routines, are presented. This study was carried out in order to analyze the dependence of the electrocatalytic activity of Pt on deposition sites and on Pt-nanoisland number and geometry. Since for low deposition overpotentials Pt preferentially deposits on step and defect sites of the Au(111) surface (compare with section 2.2.3, p. 26ff.), the primary objective was the demonstration of the applicability of double pulse deposition for the Pt/Au(111) system: A deposition of Pt nanoislands on terrace sites and a systematic variation of number and size of Pt nanoislands depending on deposition parameters was aimed at. Increasing nucleation overpotential η_{nuc} was expected to yield an increasing number of Pt nanoislands and increasing growth time t_{gro} was expected to yield an increasing size of Pt nanoislands (compare with section 3.3.1, p. 43ff.). For comparison, potentiostatic single pulses, dip coating and CV were used for deposition. In all cases the Pt deposit was analyzed and the electrocatalytic activity was measured. Furthermore, the activity of a Pt(111) single crystal was determined.

4.1.1 Characterization of platinum deposit

Pt was deposited on Au(111) by the four deposition routines, dipping (D), CV, single and double pulse technique (SP and DP), described in section 3.3.1 (p. 43ff.). Pt coverage was determined by evaluation of deposition, hydrogen-ad/desorption, CO-adlayer oxidation and PtO_x-reduction charges. The samples were additionally characterized by EC STM.

Characterization by CV

A mean coverage was calculated from hydrogen-ad/desorption, CO-adlayer oxidation and PtO_x -reduction charges for each sample. Deposition charge was not included in the calculation of the mean coverage, since the error was either rather large or the nanoislands were more than one atomic layer in height. In that case deposition charge does not result in a correct estimation of Pt surface area.

CVs showing the hydrogen ad/desorption and Pt/Au oxidation and reduction are depicted in Figure 4.1-1 for selected samples. Hydrogen is adsorbed between 0.36V and 0.1V vs. SHE in the cathodic scan and desorbed between 0.1V and 0.36V vs. SHE in the anodic scan (see dashed region in the inset in Figure 4.1-1, left). Current densities in these regimes were integrated and related to Pt coverage for each sample. Similarly, the PtO_x -reduction charge was computed from the current flow between 0.91V and 0.41V vs. SHE in the cathodic scan (compare with inset, dashed shaded region). This is possible, because PtO_x and Au_yO_z reduction occur in separate potential-regimes, unlike Pt and Au oxidation, which overlap. A closer look at the evaluated curves reveals that for increasing Pt coverage the PtO_x -reduction peak increases, whereas the Au_yO_z -reduction peak decreases. Thus, the Pt nanoislands grow mostly two-dimensional, otherwise the Au_yO_z reduction peak would stay the same and only the PtO_x -reduction peak would increase.

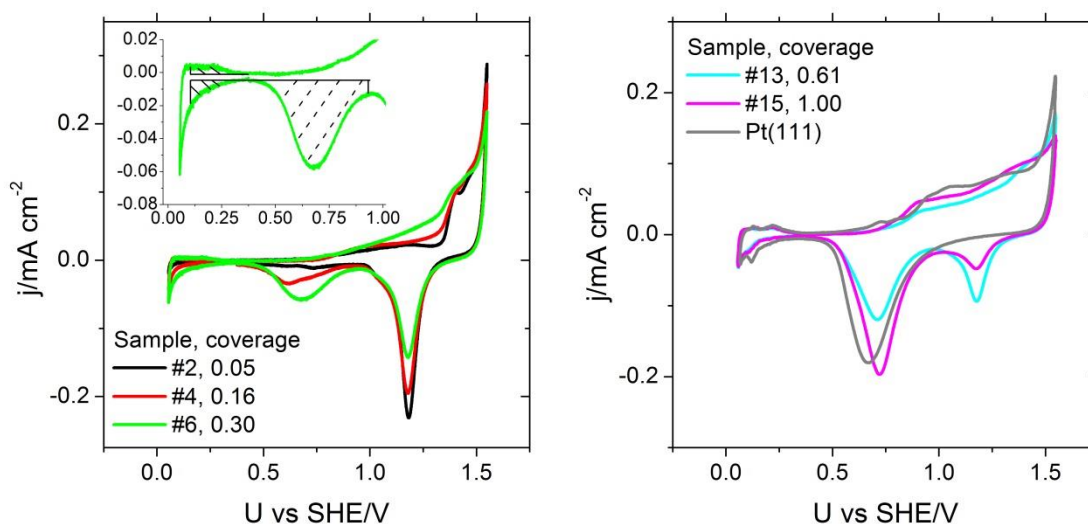


Figure 4.1-1 Hydrogen ad/desorption and Pt oxidation and reduction as measured via CV. Curves are shown for selected samples with different Pt coverage. Hydrogen adsorption/desorption occurs between 0.36V and 0.1V vs. SHE in the negative/positive scan (see inset). Pt and Au are oxidized between 0.76V and 1.55V vs. SHE in the positive scan. Oxide reduction is well separated for Au and Pt: Au_yO_z is reduced between 1.36V and 0.91V vs. SHE and PtO_x is reduced between 0.91V and 0.41V vs. SHE in the cathodic scan (see inset).

In Figure 4.1-2 CO-adlayer oxidation CVs are shown for selected samples. The number of peaks, their height and intensity vary non-linearly with Pt coverage: A rather high CO-oxidation charge density at very small Pt coverage is for example in contrast to a comparably small CO-oxidation charge density at high Pt coverage. A similar observation was already documented by Friedrich et al. [145], who investigated the CO adlayer oxidation for spherical Pt nanoparticles on polycrystalline Au. In Figure 4 of the mentioned publication by Friedrich et al., CO-adlayer oxidation CVs are shown for 3nm-sized Pt nanoparticles on Au. Three peaks, with maximum peak height at 0.87V, 1.0V and 1.2V vs. RHE, were observed. The latter two occurred for small coverages up to 0.24 ML, an additional third one at 0.87V occurred for a coverage of 0.38 ML. The investigations for this thesis show features, which are similar to Friedrich's data: The peak positions at 0.86V and 1.08V vs. SHE in the CVs shown in Figure 4.1-2 (left) match well with the ones of the mentioned publication, although a prominent peak at 1.2V vs. SHE could not be observed in this study. (Note that the SHE-scale is approximately equal to the RHE-scale of Friedrich's study, since 1M HClO₄ with an activity close to one was used as electrolyte.)

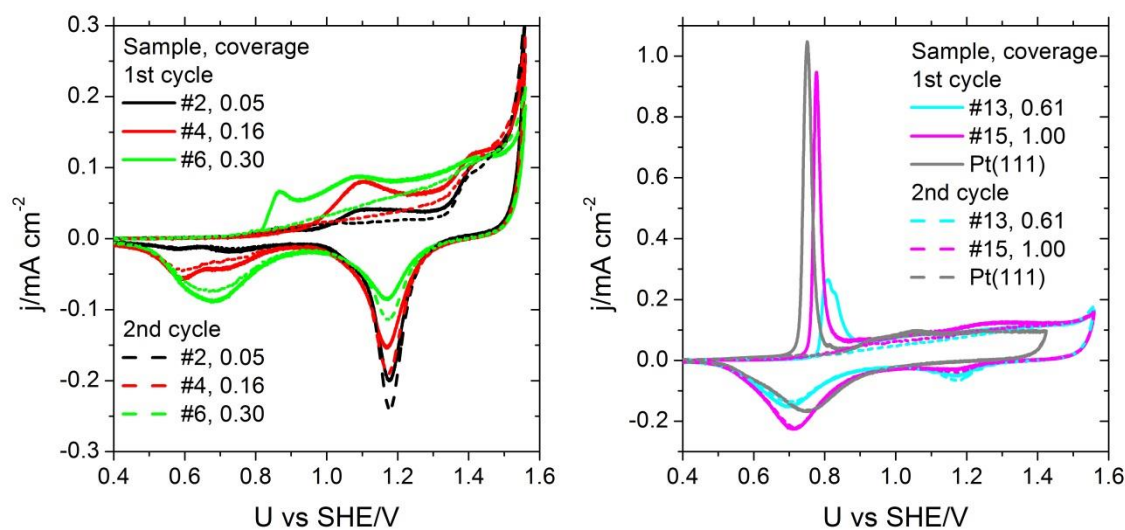


Figure 4.1-2 First and second cycles of the CO-adlayer oxidation on Pt nanoislands on Au(111) in 1M HClO₄. CVs are shown for different Pt coverages. The peak positions and intensities vary with coverage. A general trend for decreasing oxidation potential with increasing coverage can be observed.

Due to the good agreement of Friedrich's and these measurements, Pt coverages were determined with respect to the charge-coverage relations found by Friedrich et al., via comparison of the CVs. These relations are summarized in Table 1. However, the shape of the CO-adlayer oxidation peak of the sample with the highest coverage was very similar to the one of a Pt(111) single crystal, although slightly positive, and was thus related to the bulk

value of $q_{co}=320\mu\text{C}/\text{cm}^2$ (compare with [117, 150]). A comparison of the coverages determined by this method with the coverages determined by hydrogen ad/desorption and PtO_x reduction showed good agreement (see Table 8 of the Appendix, p. 123). Therefore, the q_{co} values can also be used for Pt nanoislands on Au(111).

Table 1 Charge-coverage relations q_{co} for spherical, 3nm-sized Pt nanoparticles on polycrystalline Au, as found by Friedrich et al. [145] for CO-adlayer oxidation. (The values were given as charges for the corresponding coverage in the publication and were calculated for one ML of Pt in the table for better comparability.)

Coverage/ML	Peak position(s)/V vs. RHE	Dominant peak/V vs. RHE	$q_{co}/\mu\text{C cm}^{-2}$ per ML Pt
0.05	1.0 and 1.2	no dominant peak	1200
0.24	1.0 and 1.2	1.0	600
0.38	0.87, 1.0 and 1.2	0.87	418

The different deposition techniques and times, as well as the mean Pt coverage are summarized in Table 2. Sample 2 was dipped into the deposition solution at a potential of 1.12V vs. SHE, which is actually positive of the deposition potential. A coverage of 5% of a monolayer Pt was determined by electrochemical characterization methods on this sample. This is most probably due to adsorption of the $[\text{PtCl}_6]^{2-}$ complex on the Au surface at the immersion potential [71]. For a hydrogen adsorption measurement after deposition, the potential is decreased. Then, the complex is first reduced to $[\text{PtCl}_4]^{2-}$ and finally to metallic Pt. This can be the reason for the first scan of the hydrogen adsorption cyclic voltammograms yielding a higher cathodic current, than the following ones (see Appendix, p. 128). Experiments to desorb the complex in order to get a smaller Pt coverage were not successful: Rinsing the sample extensively with water was not a suitable method to get rid of the adsorbed Pt complex. Desorption of a small fraction of the adsorbed Pt complex was achieved by oxidation of the sample, but yielded just an insignificantly reduced Pt coverage. Since this procedure influences the surface structure of the whole sample it was not used in these investigations.

Firstly, this means that a smaller coverage than about 5% of a ML cannot be reached with the used electrolyte unless Pt is dissolved after deposition. Secondly, for any deposition method used here the adsorption of the $[\text{PtCl}_6]^{2-}$ complex has to be considered, since each sample is immersed into the electrolyte at 1.12V vs. SHE. It is very probable that these 5% of a ML Pt are situated at the lower terrace of Au steps/defects (compare with Figure 4.1-3), since this is the preferred deposition site for Pt on Au (compare with section 4.2, p. 67ff.).

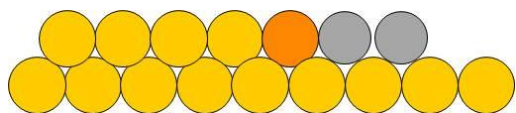


Figure 4.1-3 Sketch of Pt atoms (gray circles) deposited on the lower terrace of a step/defect site (orange circle) on an Au(111) surface. (Au atoms: yellow and orange circles)

Table 2 Deposition routines and corresponding parameters used for studying the dependence of electrocatalytic activity on Pt coverage. D: dipping, DP: double pulse deposition, SP: single pulse deposition, CV: cyclic voltammetry, ML: monolayer.

Sample #	Deposition method	Deposition properties				Mean Pt coverage/ML
2	D	Dipping by hand, dipping time ~ 1s				0.05±0.01
	Double pulse	$\eta_{\text{nuc}}/\text{V}$	$t_{\text{nuc}}/\mu\text{s}$	$\eta_{\text{gro}}/\text{V}$	t_{gro}/s	
4	DP1	-0.21	30	-0.01	500	0.16±0.05
5	DP1	-0.21	30	-0.01	200	0.12±0.04
6	DP2	-0.31	30	-0.11	50	0.30±0.04
7	DP2	-0.31	30	-0.11	5	0.15±0.03
8	DP2	-0.31	30	-0.11	1	0.13±0.03
	Single pulse	$\eta_{\text{dep}}/\text{V}$		t_{dep}/s		
10	SP	-0.26		1		0.32±0.07
11	SP	-0.26		0.01		0.05±0.01
12	SP	-0.26		0.00001		0.06±0.02
	CV	scan rate/ V s^{-1}		number of cycles		
1	CV	0.05		2		0.34±0.06
13	CV	0.05		5		0.61±0.05
15	CV	0.05		5		1.00±0.22

Characterization by EC STM

The characterization of several samples by EC STM is discussed in the following part. These samples were fabricated like described, however, their electrocatalytic activity was not determined. Also, CO-adlayer oxidation and PtO_x-reduction measurements were skipped, since the reactions would have been accompanied by surface oxidation and resulted in a changed surface structure. If a surface coverage was calculated from the EC STM images, 2% coverage was subtracted, since the unreconstructed Au(111)-surface reveals about 2-3% of a monolayer of Au islands with a size comparable to that of the Pt islands.

An exception to that represents the first sample (see Figure 4.1-4, sample #1, deposition via CV), which was imaged via EC STM subsequently after activity and characterization measurements. Pt nanoislands were 2-3 atomic layers high and had a diameter of about 2-4nm. They deposited preferably in the vicinity of step sites. By assuming a cylindrical shape of the islands with a mean diameter of 3nm and a mean height of 0.6nm, a Pt coverage of (32±5)% of a ML was calculated after counting the Pt islands (550 islands) of two 100nm x

100nm sized parts of the image shown below. This value is very close to the one determined by adsorption and reduction measurements (compare with Table 2).

The images shown in Figure 4.1-5 were taken of a surface that resembled the one of sample #5 (double pulse deposition DP1, parameters see Table 2). Yet, the growth time t_{gro} was only 150s. The bigger Pt nanoislands were 1-2 atomic layers high and had a diameter of 4-7nm, however, there was also a considerable number of very small islands with a diameter of 1-2nm. The big islands formed exclusively on terrace sites, whereas the small ones were only found in the vicinity of step sites. It is very probable that the bigger islands were formed due to the double pulse deposition, for which nuclei should have formed on the terraces due to the high overpotential. By assuming a cylindrical shape of the islands, a Pt coverage of $(12\pm 8)\%$ of a ML was calculated after counting the Pt islands (171 islands) of the two images shown below. This coverage is very similar to the one determined in electrochemical adsorption and reduction measurements. Furthermore, the steps on the Au surface seem very rough, which leads to the conclusion that Pt deposited also on these sites.

In Figure 4.1-6 images of a surface that was fabricated like sample #7 (double pulse deposition DP2, parameters see Table 2) are shown. The Pt nanoislands were one but mostly two atomic layers high and had a diameter of 3-4nm. The islands deposited mostly on terrace sites, some of them in the vicinity of step sites. By assuming a cylindrical shape of the islands, a Pt coverage of $(14\pm 3)\%$ of a ML was calculated after counting the Pt islands (229 islands) of the two images shown below. This coverage is comparable to the one determined by ad/desorption and reduction measurements. It seems that Pt also deposited on step sites, however the steps on the Au surface are not as rough as observed for the previous sample.

Comparing Figure 4.1-5 and Figure 4.1-6, the theoretical relation of island number and size to nucleation overpotential and growth time was confirmed (compare with section 2.2.3, p. 26ff.): Island diameter decreases with decreasing growth pulse time t_{gro} . Furthermore, the number of islands increases with increasing nucleation overpotential. The island height doesn't increase, so islands grow in horizontal but not in vertical direction. Hence, a preferential growth of Pt on combined Pt/Au sites can be concluded. These results are contrary to double pulse deposition of Pt on HOPG and diamond [30, 31]. On these substrates Pt grows hemispherical, since the interaction of Pt with HOPG and diamond is smaller than with Au.

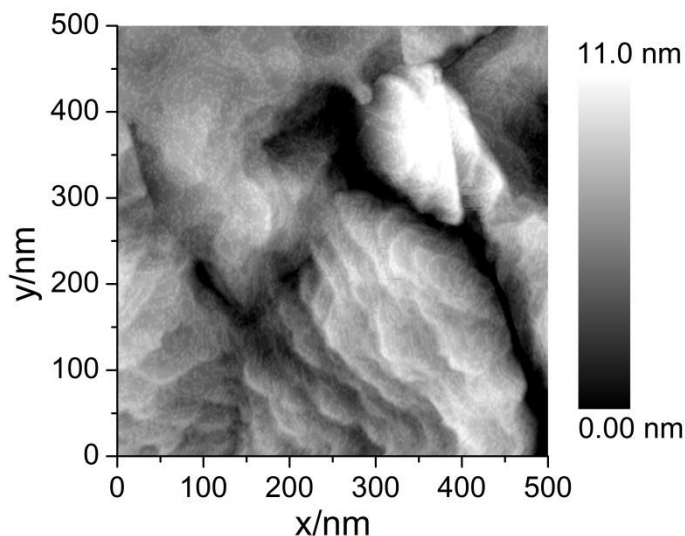


Figure 4.1-4 EC STM image of Pt on Au(111), sample #1, in 0.1M HClO₄. Pt was deposited via CV, in two cycles with a scan rate of 0.05V/s. The Pt coverage determined by electrochemical measurements is 34% of a ML. Pt nanoislands are 2-3 atomic layers high and have a diameter of about 2-4nm.

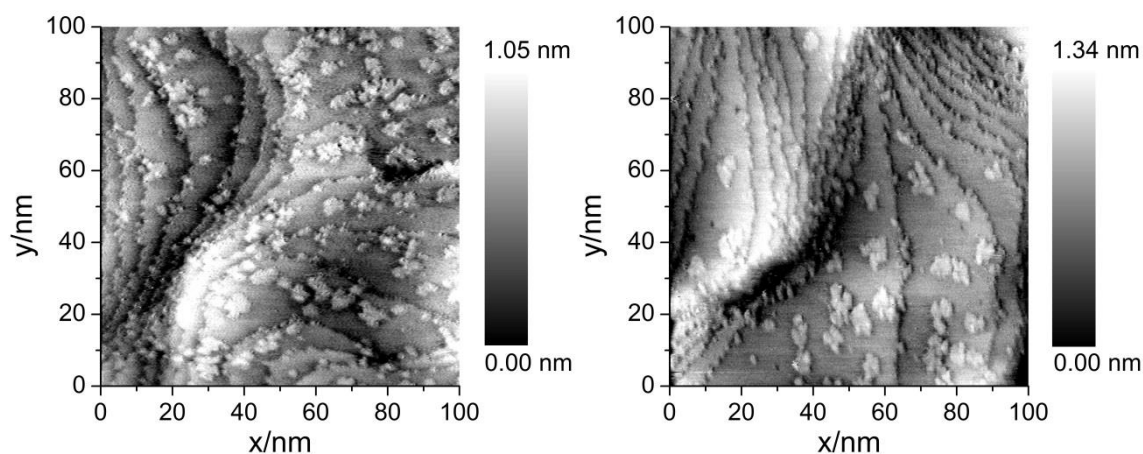


Figure 4.1-5 EC STM image of Pt on Au(111), a sample similar to #5, in 0.1M HClO₄. Pt was deposited via double pulse deposition, with a nucleation overpotential and time of $\eta_{nuc} = -0.21V$ and $t_{nuc} = 30\mu s$ and a growth overpotential and time of $\eta_{gro} = -0.01V$ and $t_{gro} = 150s$. Pt coverage, as determined by electrochemical measurements is 12% of a ML, equal to the one determined by EC STM images. The bigger Pt nanoislands are 1-2 atomic layers high and have a diameter of 4-7nm. The smaller islands have a diameter of 1-2nm.

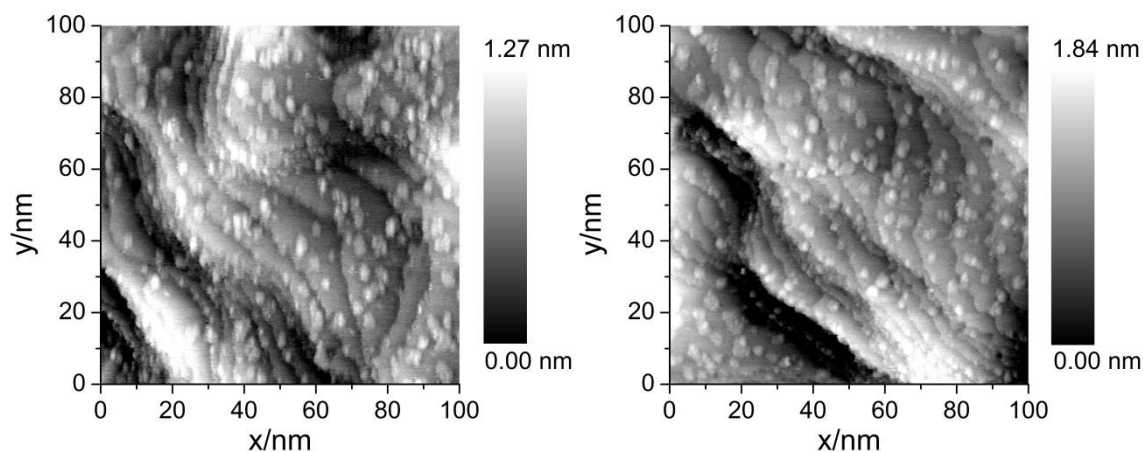


Figure 4.1-6 EC STM image of Pt on Au(111), a sample similar to #7, in 0.1M HClO₄. Pt was deposited via double pulse deposition, with a nucleation overpotential and time of $\eta_{nuc}=-0.31V$ and $t_{nuc}=30\mu s$ and a growth overpotential and time of $\eta_{gro}=-0.11V$ and $t_{gro}=5s$. Pt coverage determined by electrochemical measurements is 16% of a ML, which is very similar to the one determined by EC STM images of 14% of a ML. The Pt nanoislands are one but mostly two atomic layers high and have a diameter of 3-4nm.

4.1.2 Dependence of electrocatalytic activity on coverage

In Figure 4.1-7 Tafel plots of the kinetic and Pt-specific HER- and HOR-current densities are shown for selected samples with different Pt coverage and a Pt(111) single crystal. Pt-specific current density j_{Pt} was calculated as ratio of kinetic current density and mean Pt coverage (compare with Table 2) for each sample. The kinetic current density was evaluated as described in section 3.4.5 (p. 53ff.). Therefore, the RC-time constant $\tau=R_{\Omega}C_{DL}$ was calculated, which was about $5\mu s$ for all samples and the linear fit was performed in a time range of $30\mu s$ to $100\mu s$. The influence of the double-layer charging current in this time range of about $0.0025I_{0a}$ (compare with section 3.4.5) is very small. Thus, the error due to double-layer charging is quite small.

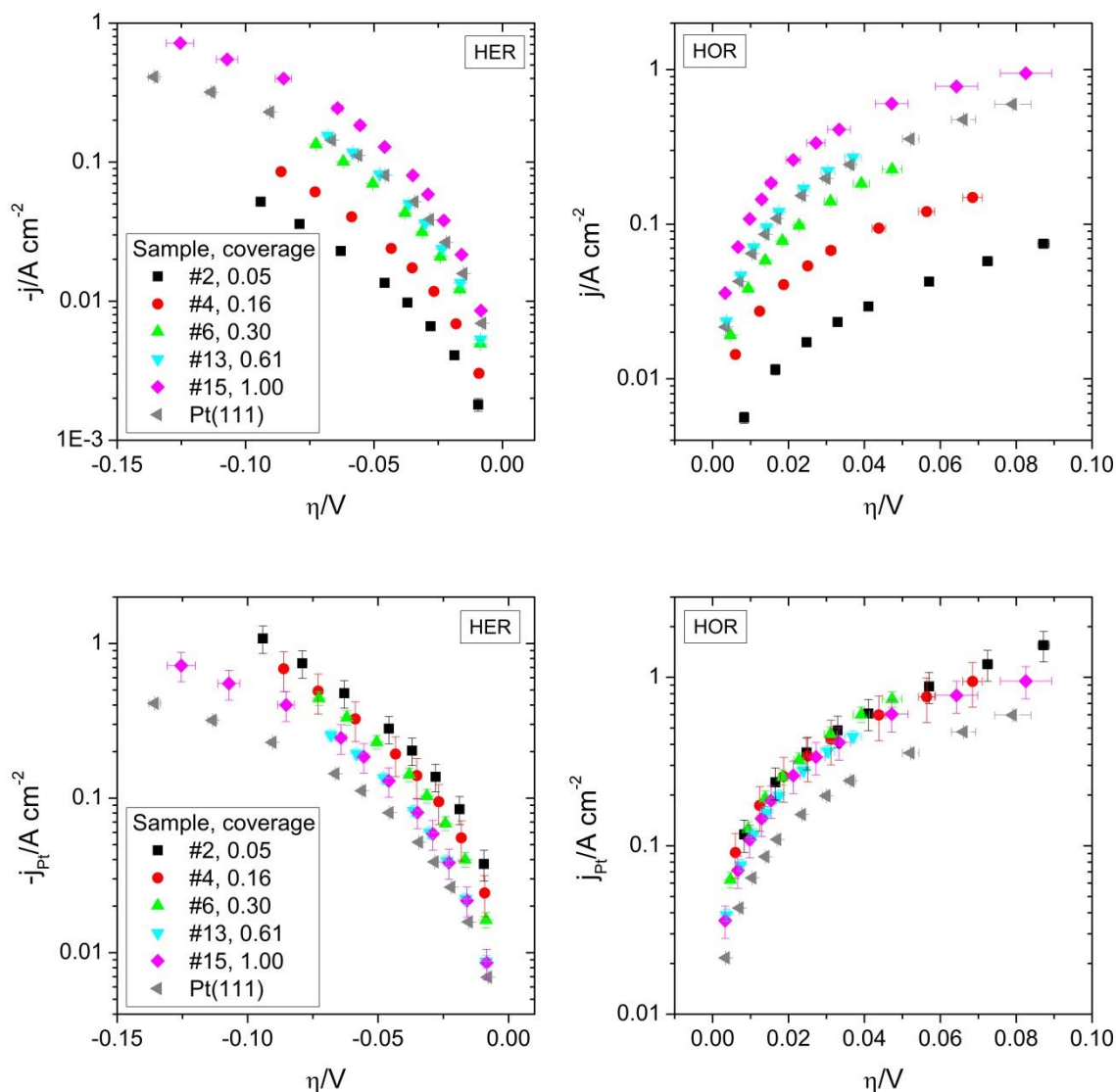


Figure 4.1-7 Tafel plots of the kinetic current density j (upper part) and the Pt-specific current density j_{Pt} (lower part) for the HER (left) and the HOR (right) conducted at Pt nanoislands on Au(111) and at Pt(111) in 1M HClO₄. The electrolyte was saturated with H₂.

The Tafel plots of the kinetic current density for HER and HOR show an increasing current density for increasing Pt coverage, except for the samples with coverages of 0.61 and 1.00. The current density for a Pt coverage of 0.61 is very similar to the one for Pt(111). The current density for a Pt coverage of 1.00 ($\Theta = A_{Pt}/A_{Au} = 1.00$) is higher. The Tafel plot of the Pt-specific current density j_{Pt} for the HER shows an increasing current density for decreasing Pt coverage. For HOR, an increase from bulk Pt(111) to Pt nanoislands on Au(111) can be recognized. However, in this case the differences in current densities for various coverages of Pt on Au(111) are small on the logarithmic scale. These data are better represented by a plot of the Pt-specific current density at a specified overvoltage versus the Pt coverage (see Figure 4.1-8). The Pt-specific current densities at specified overvoltages $j_{Pt,\eta}$ were derived by linear

interpolation/extrapolation of the $\eta - j_{Pt}$ curves of Figure 4.1-7. An enhancement for decreasing coverage can also be deduced from these curves. In the case of the HER, the activity is enhanced by more than a factor of three and the trend of increasing current density with decreasing coverage is obvious. Moreover, this trend is the same for all three overpotentials η , for which the Pt-specific current density was determined. However, in the case of HOR an increasing current density is only clear for the transition from bulk Pt(111) to monolayer and submonolayer coverages of Pt on Au(111). Current densities for decreasing Pt coverage vary to some extent, but lack a clear trend. Again, the different overpotentials have no influence on this behavior.

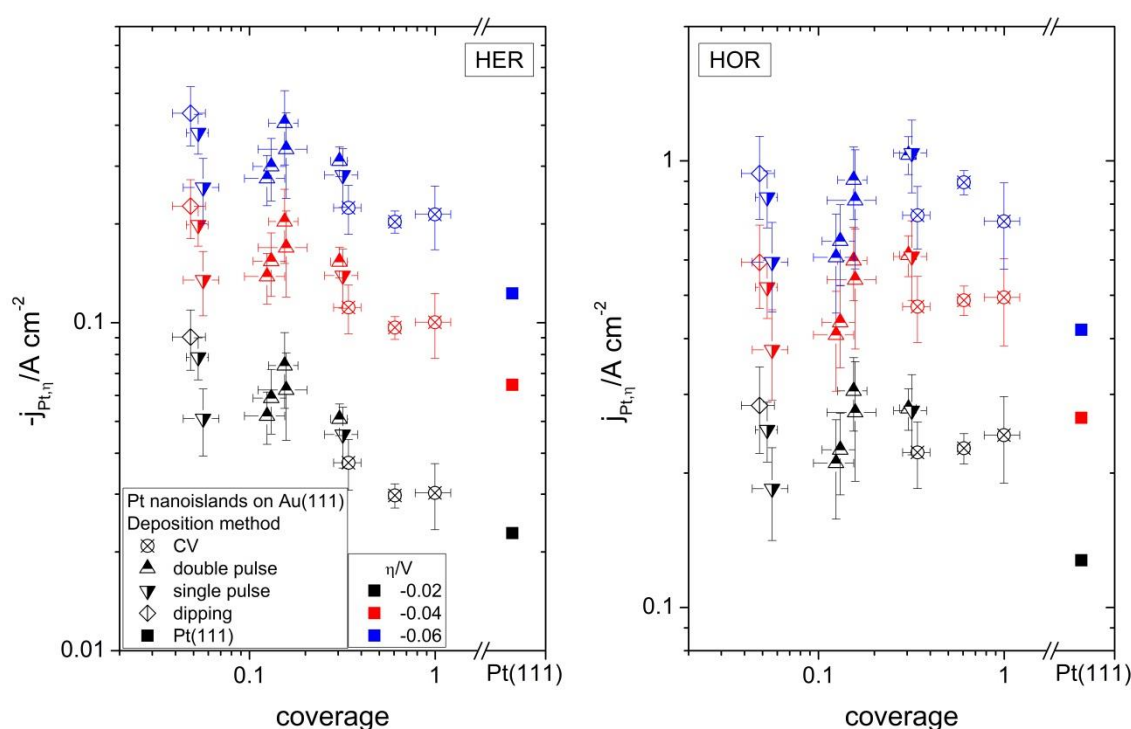


Figure 4.1-8 Pt-specific current density $j_{Pt,\eta}$ evaluated from HER- (left) and HOR-Tafel plots (right) at overpotentials $\eta = +/-0.02V$, $+/-0.04$ and $+/-0.06V$, plotted versus coverage for different deposition methods. A general trend of increasing current density $j_{Pt,\eta}$ with decreasing Pt coverage can be seen.

The influence of the deposition procedure on catalytic activity cannot easily be determined. In the case of HER, the highest activity is found for a sample which was dip-coated and for which Pt nanoislands deposited preferably on the lower terrace of the rim sites of steps/defects. For both reactions, an enhancement is also seen, when comparing Pt(111) with an Au(111) surface that is almost completely covered by Pt (coverage ~ 1). As already discussed in the previous section, the Pt islands/layers are about 2-3 atomic layers high, which

means that strain is still present in the topmost Pt layer [43]. Moreover, the islands are preferentially situated at step/defect sites of the Au(111) surface, which can be a reason for the higher activity. As to the Pt deposited via double pulse deposition, current densities are very close to each other, such that no statement about the influence of size and/or number of Pt nanoislands can be made.

4.2 Platinum nanoislands on Au(111) – Variation of defect density on the Au(111) surface

The importance of defects on the Au(111) surface and their influence on Pt deposition and Pt activity was already discussed in the previous section. Another particular effect, which is ascribed to specific defect sites on an Au surface, is spillover for the HOR (compare with section 2.3.3, p. 35ff.). Therefore, the influence of defect density on an Au(111) surface on electrocatalytic properties of deposited Pt nanoislands was evaluated [133]. The goal of these measurements was to demonstrate that spillover takes place during the HOR at Pt nanoislands on Au. This aspect was assumed to lead to an activity enhancement for the HOR at Pt nanoislands on defect-rich Au(111) when compared with Pt nanoislands on defect-poor Au(111). Such a behavior was expected to result from H₂ dissociation at specific defect sites of the Au(111) surface (Tafel or Heyrovský reaction), spillover of the thus-generated adsorbed hydrogen atoms from the Au to the Pt surface and its oxidation to a proton via the Volmer reaction. Since for HER, the spillover effect should depend much less on defect sites on the Au surface, Pt activity was thought to be the same for Pt nanoislands on defect-rich and on defect-poor Au surfaces.

In order to generate a high defect density on the Au(111) surface it was oxidized and subsequently reduced in 1M HClO₄. Au surface area was determined by Cu upd. Pt nanoislands were electrochemically deposited from 0.5mM K₂PtCl₆ + 1M HClO₄ solution via the potentiostatic single pulse method. A low overpotential was applied for deposition, so nanoislands grew mostly at step and defect sites of the Au(111) surface. HOR and HER currents at these samples were subsequently recorded in H₂-purged 1M HClO₄ after application of potentiostatic pulses. The Pt surface area was determined by hydrogen adsorption, CO-adlayer oxidation and PtO_x reduction. Additionally, EC STM images were recorded.

4.2.1 Defect-poor and defect-rich Au(111)

Defect-poor and defect-rich Au(111) surfaces were fabricated following the procedure discussed in section 3.2.1 (p. 40ff.). Since in this context the Au(111) surface structure is of fundamental importance, it will be discussed in more detail than in the previous section. In Figure 4.2-1 EC STM images of the annealed Au(111) surface, which was immersed in 0.1M HClO₄ at a potential of 0V vs. SHE, are shown [151]. At 0V vs. SHE the Au surface is in the reconstructed state (compare with section 2.2.2, p. 23ff.). Therefore, the dislocation lines can be seen (compare with Figure 2.2-3, p. 25). Neighboring pairs of lines have a distance of $(6.0\pm 0.5)\text{nm}$ and the distance between the lines of one pair is $(4.0\pm 0.5)\text{nm}$. Within accuracy these values are in line with the ones measured in UHV. The dislocation lines are mostly perpendicular to the step edges on the lower as well as on the upper terrace, except for two Y-shapes on the lower right part of the step. Thus, the step has a preferential (111) orientation [63], which is not surprising, because this is the more stable configuration [59] (compare with section 2.2.2, p. 23ff.). Therefore, it is suggested that in general steps on the used Au(111) surfaces preferably arrange such that (111) microfacets are formed.

In the upper right corner of the image on the right hand side of Figure 4.2-2 the Au(111) surface is shown after CV to a maximum potential of 1.4V vs. SHE. The reconstruction was lifted during this procedure and the excess of Au atoms of the upper, formerly reconstructed layer agglomerated to Au islands.

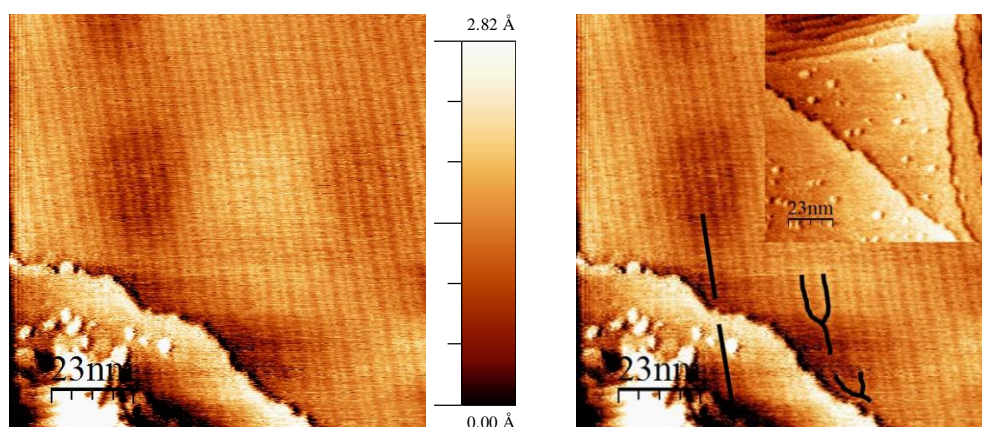


Figure 4.2-1 EC STM image of Au(111) in 0.1M HClO₄. The sample was immersed in the electrolyte after the annealing procedure, at a potential of $U_{WE}=0\text{V}$ vs. SHE ($U_{tip}=0.01\text{V}$ vs. SHE, $\Delta U=0.01\text{V}$, tunneling current $I_t=1\text{nA}$). Thus, the surface is in the reconstructed state and the dislocation lines, which are indicated by black lines in the right image, can be observed. This image also shows the surface after lifting of the reconstruction by CV in the upper right corner at a potential of $U_{WE}=0\text{V}$ vs. SHE ($U_{tip}=-0.05\text{V}$ vs. SHE, $\Delta U=0.05\text{V}$, $I_t=1\text{nA}$).

Returning to the Au(111) surfaces used and investigated in this study, the left image of Figure 4.2-2 shows a defect-poor Au(111) surface. The Au islands have a width of (2.6 ± 0.3) nm and a height of one atomic layer. The islands cover $(3 \pm 1)\%$ of the surface. On the right side of Figure 4.2-2 a defect-rich Au(111) surface is depicted: After galvanostatic oxidation and reduction via CV, additional step sites, holes and Au clusters can be found on the surface. The holes/clusters are two to four monolayers deep/high and 10-20 nm in diameter. Smaller, 3 nm-wide Au islands as observed after lifting of the reconstruction or on the defect-poor Au(111) surface have disappeared. This can for example be due to dissolution of such islands or to their coalescence with steps. The holes and clusters, apart from (111)-step sites, have to form (100)-steps sites on the Au(111) surface as well, such that the number of (100)-step sites is higher on the defect-rich than on the defect-poor surface.

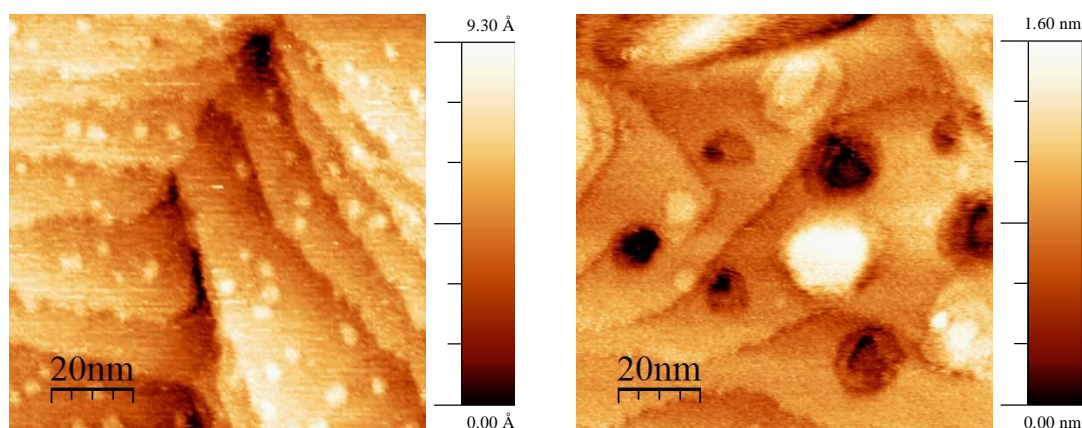


Figure 4.2-2 EC STM image of a defect-poor (left) and a defect-rich (right) Au(111) surface in 0.1M HClO₄. Both images were recorded at a potential at which the surfaces were in a reduced state. ($U_{WE}=0.05V$ vs. SHE, $U_{tip}=0.35V$ vs. SHE, $\Delta U=-0.3V$, $I_t=1nA$.)

EC STM measurements were complemented by XPS, which was performed to investigate the chemical composition of the differently pretreated surfaces. A comparison of the XPS graphs (see Figure 4.2-3) of a defect-poor, a defect-rich and a galvanostatically oxidized Au(111) surface, shows that no oxide is left on the surface after **reduction** of the galvanostatically oxidized (defect-rich) sample. Curves for non-oxidized, i.e. defect-poor, and oxidized and reduced, i.e. defect-rich, Au surface are identical. The peaks at binding energies of 84.1 eV and 87.8 eV are characteristic for Au 4f_{7/2} and 4f_{5/2} electrons. Only the XPS-graph of the galvanostatically oxidized Au surface that was **not reduced** afterwards clearly reveals a peak for the Au³⁺ state (e.g. from Au₂O₃) at a binding energy of 86 eV (compare with [122] and references therein).

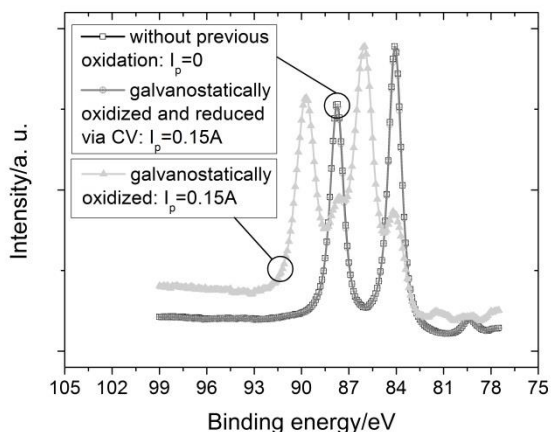


Figure 4.2-3 XPS Au 4f spectra of differently pretreated Au(111) surfaces: (i) Defect-poor Au(111): The surface was not oxidized (black squares; barely seen because of overlap with dark gray circles). (ii) Defect-rich Au(111): The surface was galvanostatically oxidized and reduced via CV (dark gray circles). (iii) Galvanostatically oxidized Au surface, which was not reduced (light gray triangles).

Figure 4.2-4 shows the comparison of Cu upd on defect-poor and defect-rich Au(111): The Au surface area, determined via evaluation of Cu deposition and Cu dissolution charge for three samples of each configuration, is constant within accuracy (see Table 3). Thus, the oxidation and reduction routine used for the fabrication of defect-rich Au(111) surfaces does not lead to an increased Au surface area.

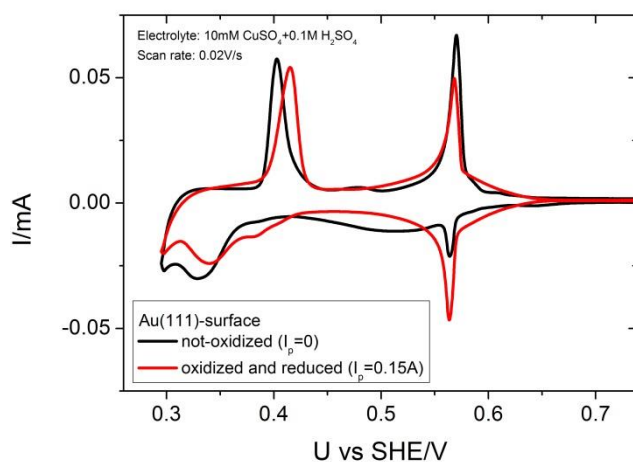


Figure 4.2-4 Cu upd from 10mM CuSO₄+1M H₂SO₄ on defect-poor and defect-rich Au(111): Au surface area, determined via evaluation of deposition and dissolution charge, of the differently pretreated samples is identical.

Table 3 Au surface area calculated from Cu upd charge for defect-poor ($I_p=0$) and defect-rich ($I_p=0.15A$) Au(111).

Au surface treatment prior to Cu upd	I_p/A	Au surface area/cm ²
No oxidation/reduction	0	0.40±0.01
		0.40±0.01
		0.40±0.01
Galvanostatic oxidation, reduction via CV	0.15	0.40±0.01
		0.40±0.01
		0.40±0.01

Cu upd starts at approximately 0.66V vs. SHE, which can be seen from the negative current in the cathodic scan (see Figure 4.2-4). The negative peak at a potential of about 0.57V vs. SHE, which is due a phase transition of randomly deposited Cu on terraces to a $(\sqrt{3}\times\sqrt{3})R30^\circ$ -structure at a coverage of $\Theta_{Cu}=2/3$ [143], is located at the same potential for defect-poor and defect-rich Au surface. However, the peak heights are different. The phase-transition of deposited Cu atoms (cathodic scan) from $(\sqrt{3}\times\sqrt{3})R30^\circ$ to (1x1), which occurs at a potential of 0.33V and 0.34V vs. SHE on defect-poor and defect-rich Au(111), respectively, illustrates that defect density is higher on the defect-rich Au surface: The shift to more positive potentials indicates that the phase transition is facilitated at step/defect sites [143, 152]. In both cases there is no sharp phase-transition peak because of varying terrace widths, which causes a broadening of the peak. The mean Au surface area was calculated to be $(0.40\pm 0.01)\text{cm}^2$. These samples were not used for HOR/HER activity measurements, because a Cu contamination could not be excluded.

4.2.2 Characterization of platinum deposit

Pt was electrochemically deposited on Au(111) using potentiostatic single pulses with a rather low overpotential of $\eta_{dep}=-0.06V$ for 0.5s. Pt coverage was determined via evaluation of deposition, hydrogen ad- and desorption, CO-adlayer oxidation and PtO_x reduction charge. However, the evaluation of the Pt deposition charge is not very reliable due to the large error caused by a rather high current range needed for double-layer charging during deposition (compare with Table 4). Therefore, the value was not used to calculate a mean coverage.

In Figure 4.2-5 hydrogen ad/desorption and oxidation and reduction cycles of the different Pt/Au samples are shown. The hydrogen ad/desorption and PtO_x reduction charges were determined as described in section 3.4.4.1 (p. 51ff.) and section 4.1.1 (p. 57).

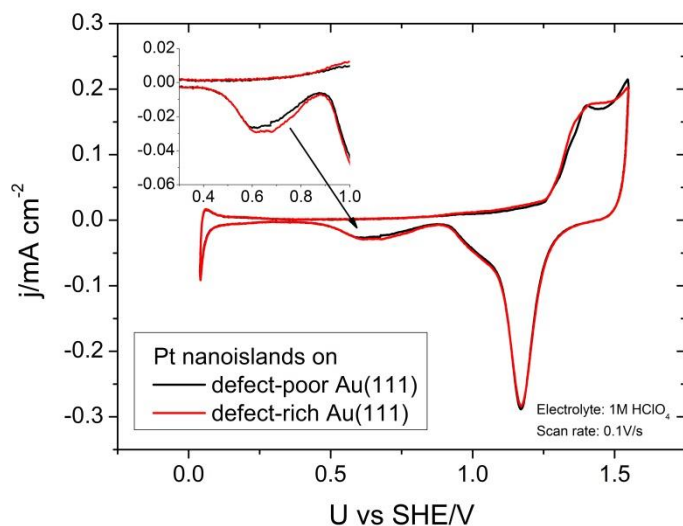


Figure 4.2-5 Cyclic voltammograms of the hydrogen ad/desorption on and the oxidation/reduction of Pt islands on defect-poor and defect-rich Au(111) in 1M HClO₄. The electrolyte was saturated with Ar. (reprinted, see [153])

In Figure 4.2-6 the first and second CVs of CO-adlayer oxidation can be seen for Pt islands on a defect-poor and on a defect-rich Au(111) surface. Here, the measured current in the second CV was subtracted from the one in the first CV for corresponding electrode potentials. The charges under the CO-oxidation peaks were calculated from the resulting potential/time-dependent current flow and related to $q=600\mu\text{C}/\text{cm}^2$ per Pt monolayer. This value was determined by Friedrich et al., who found out that the value for bulk Pt is not valid for small amounts of Pt and small particle sizes on polycrystalline Au [145]. The shape of the CO-adlayer oxidation CV of our measurements is very similar to the curve shown in Figure 4 of the aforementioned publication for similar sized Pt particles with a mean diameter of 3nm and a Pt coverage of 0.24 monolayers (circles as symbols). Thus, we related our CO-adlayer oxidation charge to the value found in the described paper. For Pt on defect-poor Au(111) we found a pronounced first oxidation peak at 1.10V vs. SHE and another smaller one at 1.30V vs. SHE. The latter could not be observed for Pt on defect-rich Au(111), whereas the first peak, with its maximum at 1.09V vs. SHE, is more pronounced than for the defect-poor sample (see inset of Figure 4.2-6). Similar observations were made for CO-adlayer oxidation on a Pd monolayer, which was deposited on well-ordered and vicinal Au(111) electrodes [154]. Kibler et al. found two peaks, the first one at 0.6V and the second one at 0.8V vs. SCE, with changing width and height corresponding to different step densities. The height of the peak at 0.6V vs. SCE increased with increasing step density whereas the one at 0.8V vs. SCE decreased. Therefore, the peak at 1.10V vs. SHE in our measurements can be due to CO-adlayer oxidation at Pt islands on defect sites, which is rather broad due to a variety of

different types of defects. The peak at 1.30V vs. SHE could then be ascribed to CO-adlayer oxidation at Pt islands on terraces. On defect-rich Au(111) the attraction of defect sites for Pt islands is obviously very strong, such that all Pt deposits on the defect sites.

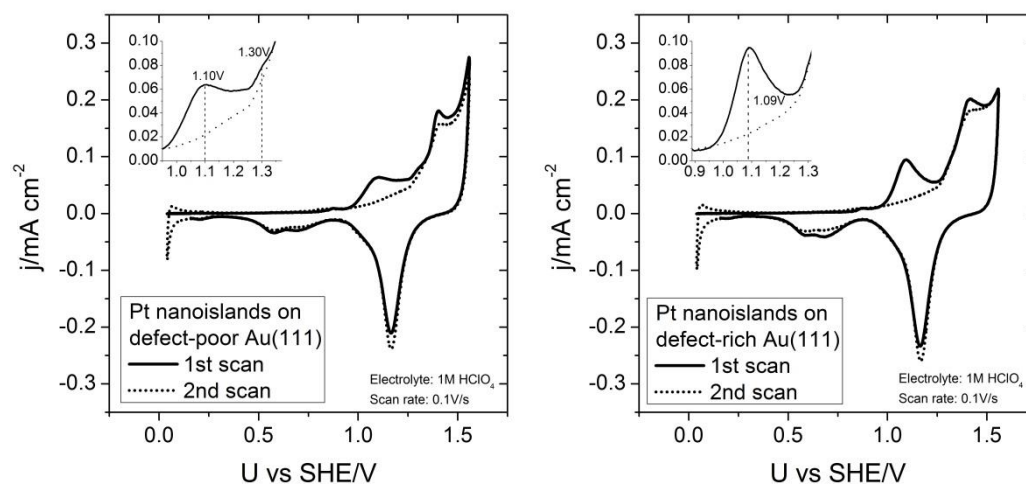


Figure 4.2-6 First and second cycle of the CO-adlayer oxidation on Pt islands on defect-poor and defect-rich Au(111) in 1M HClO₄. One rather pronounced peak occurs at 1.10V and a considerably smaller one at 1.30V vs. SHE for the defect-poor sample. A rather broad peak occurs at 1.09V vs. SHE for the defect-rich sample. (reprinted, see [153])

In Table 4 Pt coverages are listed for four samples. When comparing the Pt coverage determined through Pt deposition, hydrogen ad-/desorption, CO-adlayer oxidation and PtO_x reduction for each sample, very similar values are found with respect to the corresponding errors. Comparison of the mean coverage on all four samples shows that Pt coverage was slightly higher on defect-rich Au(111). However, differences are rather small, such that a coverage-determined effect on electrocatalytic activity can be excluded, because this effect did not show up between coverages from 10-20% of a monolayer of Pt (compare with [28]). This was quite an important prerequisite to separate support effect from coverage effect.

Table 4 Comparison of Pt coverage on the different samples, determined via evaluation of the charge recorded during Pt deposition, hydrogen ad-/desorption, CO-adlayer oxidation and PtO_x reduction. The mean coverage was calculated from all values listed, except Pt deposition coverage, which had a very large error. (reprinted, see [153])

Sample #	Description of Au surface	Pt coverage/ML, determined via				Mean coverage/ML
		Pt deposition charge	Hydrogen ad-/desorption charge	CO-adlayer oxidation charge	PtO _x reduction charge	
1	Defect-poor	0.11±0.18	0.16±0.04	0.14±0.02	0.14±0.02	0.15±0.02
2		0.12±0.18	0.14±0.04	0.13±0.02	0.14±0.02	0.14±0.01
3	Defect-rich	0.14±0.18	0.15±0.04	0.16±0.02	0.15±0.02	0.15±0.01
4		0.14±0.18	0.16±0.04	0.17±0.02	0.16±0.02	0.16±0.01

Furthermore, equally pretreated samples were characterized via EC STM: In Figure 4.2-7 and Figure 4.2-8 EC STM images of Pt nanoislands on defect-poor and defect-rich Au(111) are shown: On each sample monoatomic high steps were found. However, there were considerably more steps as well as large Au islands (10-20nm in diameter) and holes on the defect-rich Au surface compared to the defect-poor Au surface. Pt islands on defect-poor Au(111) deposited in the vicinity of monoatomic high Au steps but also on extended terraces (compare with Figure 4.2-7). The islands are mostly monoatomic in height; about 7% of the islands are two monolayers high. The diameter of the islands ranges from 1nm to 7nm (see also Figure 4.2-9), the mean diameter is 1.5nm. The fraction of Au islands on a defect-poor Au(111) surface, which are present due to the lifting of the reconstruction is $(3\pm 1)\%$ of a monolayer (compare with previous section). Therefore, Pt coverage, calculated from the island-diameter distribution via assuming a circular shape and subtracting Au islands, is $(6.2\pm 1.6)\%$ of a monolayer. Comparing this coverage with the value determined in purely electrochemical measurements ($\approx 14\%$ of a monolayer; see Table 4), we find that about $(44\pm 12)\%$ of all islands could be visualized. Pt islands on defect-rich Au are nearly exclusively found in the vicinity of monoatomic high steps and islands; islands on terrace sites can hardly be observed (see Figure 4.2-8). The number of islands with a height of more than one monolayer is negligibly small. Here, the diameter of the islands is in between 1nm and 3nm (see also Figure 4.2-9), the mean diameter is 1.6nm. Pt coverage is evaluated as $(1.0\pm 0.5)\%$ of a monolayer, i.e. about $(6\pm 3)\%$ of all islands could be visualized.

The discrepancy in coverage values determined through EC STM and adsorption/oxidation/reduction charges originates due to the following reason: Pt islands deposit preferably at step and defect sites [71]. If deposited at a very small overpotential, like in this study (deposition potential $E_{\text{dep}} = -0.05\text{V}$ vs. MSE), the islands grow pseudomorphically and their height is one monolayer, which was confirmed by Kondo and coworkers via resonance surface X-ray scattering (RSXS) measurements [43]. Therefore, Pt islands consisting of Pt atoms that attach on the lower terrace of step/defect sites (see Figure 4.2-10b) cannot be distinguished from the adjacent Au atoms, since the atomic radii of the two elements are nearly equal. The effect is very pronounced for Pt islands on defect-rich Au(111), since only about 6% of all the islands could be seen in the images. Up to now so-called “chemical contrast”-STM for bimetallic surfaces was only achieved on terraces and step/defect sites with UHV-STM [155-157] and on terraces with EC STM [158] for metal alloys. It is concluded from these results that islands that couldn't be visualized via EC STM attached on the lower terrace of step/defect sites (compare with Figure 4.2-10b). Islands

visualized in the images were well separated (compare with Figure 4.2-10a), such as the ones located on terraces or in the vicinity of step/defect sites. Thus, about $(56\pm 12)\%$ of the Pt nanoislands on defect-poor Au(111) and about $(94\pm 3)\%$ of the Pt nanoislands on defect-rich Au(111) attached on the lower terrace of steps/defects.

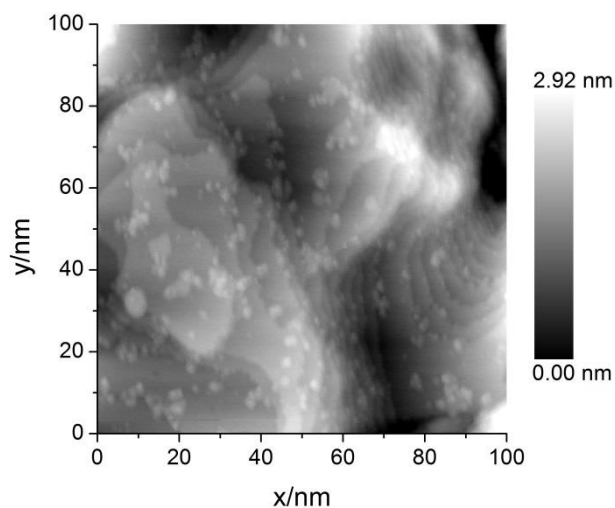


Figure 4.2-7 EC STM image of Pt on defect-poor Au(111) in 0.1M HClO₄. The corresponding island-diameter distribution is shown in Figure 4.2-9. The mean diameter of the Pt islands is 1.5nm, they are mostly monoatomic in height and deposit preferentially in the vicinity of step/defect sites, but also on terraces. (reprinted, see [153])

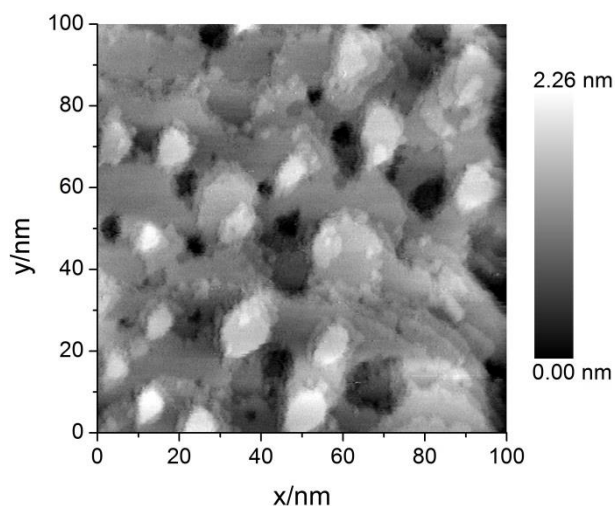


Figure 4.2-8 EC STM image of Pt on defect-rich Au(111) in 0.1M HClO₄. The corresponding island-diameter distribution is shown in Figure 4.2-9. The mean diameter of the Pt islands is 1.6nm, they are monoatomic in height and deposit nearly exclusively in the vicinity of step/defect sites. (reprinted, see [153])

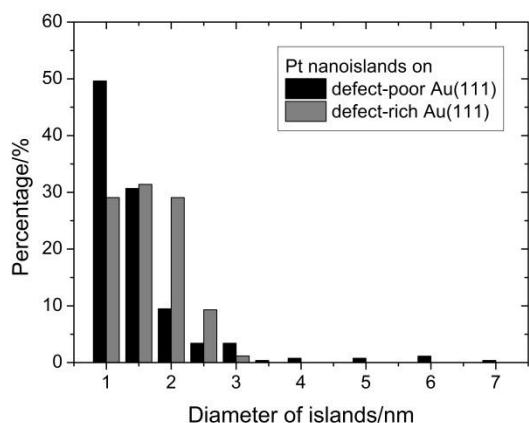


Figure 4.2-9 Pt-island diameter distribution evaluated with EC STM images of the corresponding surfaces. (reprinted, see [153])

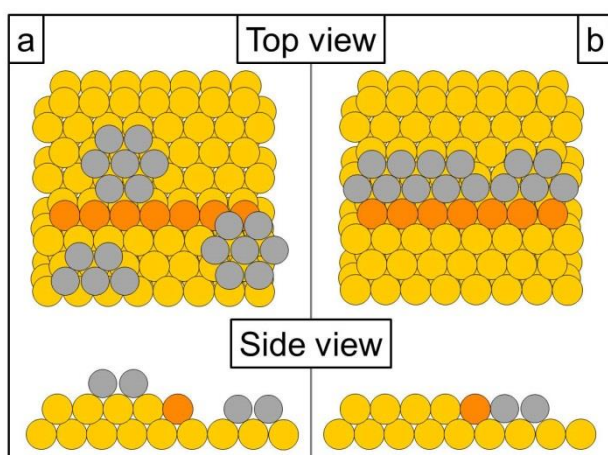


Figure 4.2-10 Sketch showing top and side view of Pt islands (gray circles) on Au(111) (yellow/orange circles) well separated on terrace sites or in the vicinity of step/defect sites (orange circles), that can be visualized by EC STM (a) and islands attached on the lower terrace of step/defect sites that cannot be distinguished from the Au(111) surface due to very similar atomic radius of Pt and Au (b).

4.2.3 Dependence of electrocatalytic activity on defect density

In Figure 4.2-11 Tafel plots of the kinetic and Pt-specific HOR- and HER-current densities for Pt nanoislands on defect-poor and defect-rich Au(111) are shown. Pt-specific current density was calculated as ratio of kinetic current density and mean Pt coverage (compare with Table 4) for each sample. This calculation was based on the precondition that the measured current originated only from the Pt nanoislands present on the Au(111) surface. In order to make sure that this precondition was met, an HOR-investigation was performed for the defect-rich Au(111) surface as a reference. Current densities in this measurement were more than two

orders of magnitude lower than for the Pt/Au samples. Therefore, the HOR- and HER-currents on the pure Au surface can be neglected in this context.

The kinetic current density was evaluated as described in section 3.4.5 (p. 53ff.). Therefore, the RC-time constant $\tau=R_{\Omega}C_{DL}$ was calculated, which was about $2\mu\text{s}$ ($R_{\Omega}\approx 0.3\Omega$, $C_{DL}\approx 6\mu\text{F}$) for Pt on defect-poor Au(111) and $4\mu\text{s}$ ($R_{\Omega}\approx 0.3\Omega$, $C_{DL}\approx 13\mu\text{F}$) for Pt on defect-rich Au(111). Pt coverage was practically identical on all four samples (see Table 4). Concerning HOR, specific current densities for Pt on defect-rich Au(111) are higher by slightly less than a factor of two, for HER specific current densities are higher by a factor of three when compared with Pt on defect-poor Au(111).

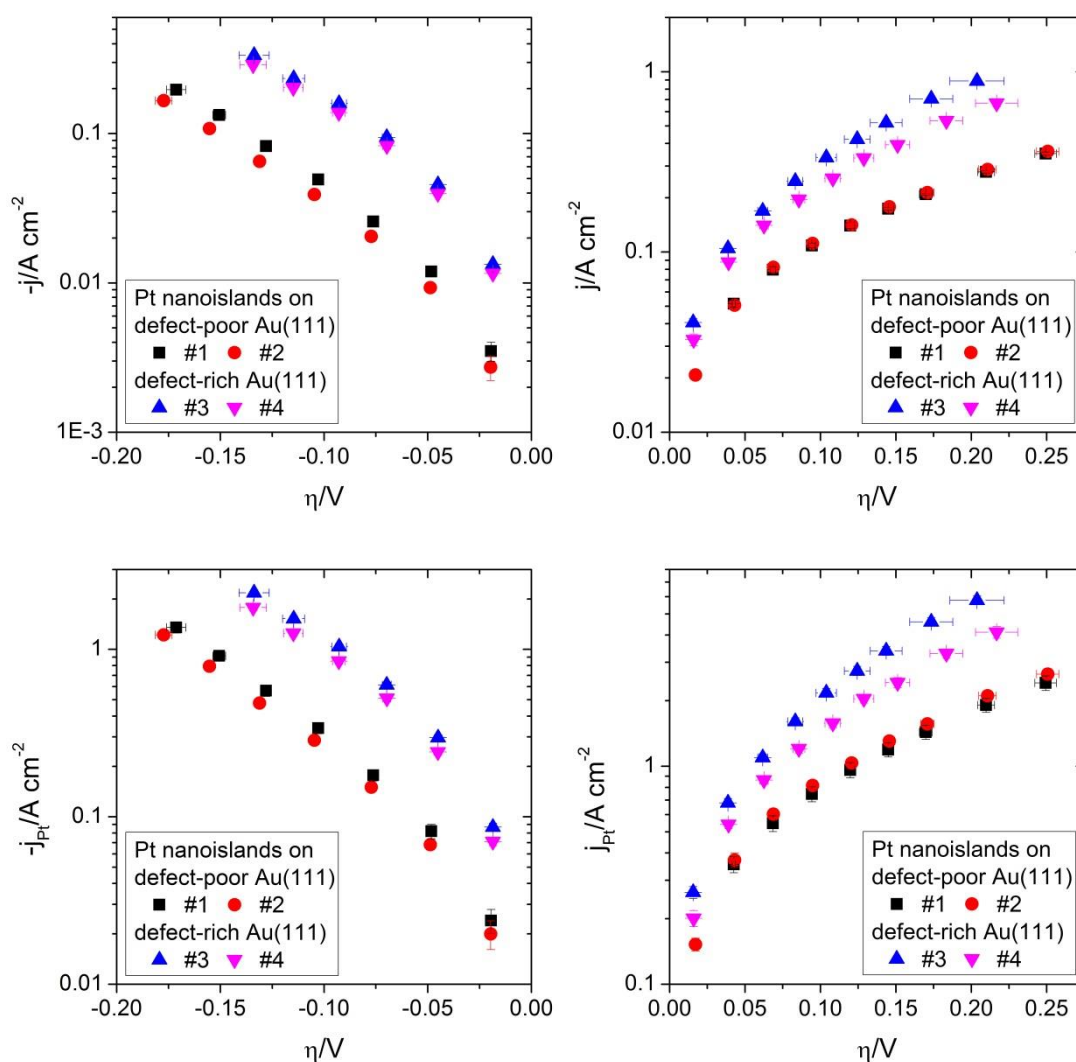


Figure 4.2-11 Tafel plot of the kinetic current density j (upper part) and Pt-specific current density j_{Pt} (lower part) for the HER (left) and the HOR (right) conducted at Pt nanoislands on defect-poor and defect-rich Au(111) in 1M HClO₄. The electrolyte was saturated with H₂. Pt coverage was identical on all four samples. The kinetic as well as the specific current density for Pt on defect-rich Au(111) is twice as high as for Pt on defect-poor Au(111) in the case of the HOR. For the HER the enhancement is even a factor of three. (reprinted, see [153])

As already mentioned in section 2.3.2, (p. 32ff.), many researchers found the catalytic activity determined by step and defect sites of support or catalyst material [23, 29, 96, 104, 159-161]. In various cases it turned out that activity increased for increasing step/defect density. Thus, in this work, the part of the islands that attached directly to step/defect sites is considered as the main contributor to electrocatalytic activity. In that case the contribution from all other islands (see also previous section and Figure 4.2-10, p. 76) can be neglected. By relating measured kinetic current density to the part of the islands that attached on the lower terrace of step/defect sites, we obtain a different result (see Figure 4.2-12): Specific current density for HOR is quite similar on defect-poor and defect-rich samples. The HER-current density, however, still differs and is higher by nearly a factor of two for Pt on defect-rich Au(111).

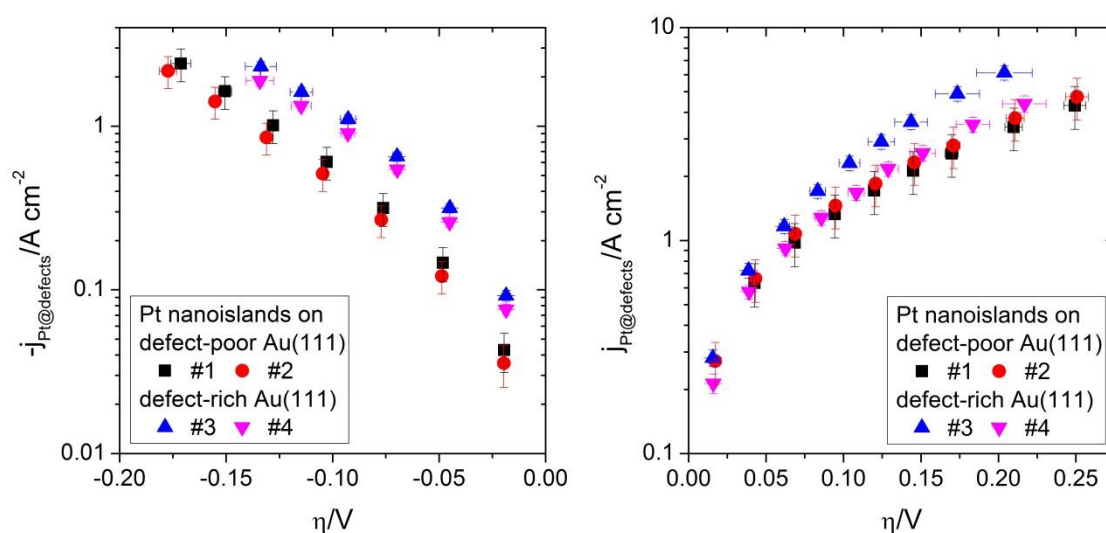


Figure 4.2-12 Tafel plot of the specific current density for HER (left) and HOR (right) for about 56% (on defect-poor Au(111)) and 94% (on defect-rich Au(111)) of all Pt nanoislands. These islands are located on the lower terrace of step and defect sites of the Au(111) surface (see also Figure 4.2-10b). For HOR the difference in specific current density when comparing Pt on defect-poor and on defect-rich Au(111) is rather small, for HER it is nearly a factor of two. (reprinted, see [153])

4.3 Platinum nanospheres from micellar diblock-copolymers on Au(111)

The generation of Pt nanospheres on Au(111) was motivated by the aim of demonstrating that the strain effect is not responsible for an activity enhancement when the Au surface is not completely covered by Pt. Hence, Pt nanospheres were established on Au(111) by diblock copolymer micelle lithography. Their electrocatalytic activity was compared with the activity of Pt nanoislands, which were electrochemically deposited on Au. Pt nanoislands are strained on the Au(111) surface, because of their height of only one or two atomic layers. In contrast, the topmost layers of Pt nanospheres are not strained, because of their height of several nanometers. The investigation was expected to yield equal activities for Pt nanoislands and Pt nanospheres concerning HER and HOR. Such a finding would imply that an enhancement of Pt activity on Au surfaces that are partially covered by Pt is determined by spillover and defects, but not by strain.

4.3.1 Characterization of platinum nanospheres

The samples were fabricated as described in section 3.3.2 (p. 45ff.). Presumably, some impurities assembled on the Pt surface during/after plasma etching, transfer and handling. Therefore, the surface had to be activated for electrochemical measurements. Such activation consisted of several oxidation-reduction cycles between 0.05V and 1.55V vs. SHE. Without that procedure, Pt was hardly detectable and the activity of the non-activated samples was quite low. After activation Pt coverage was determined via evaluation of hydrogen ad- and desorption, CO-adlayer oxidation and PtO_x-reduction charge. The average Pt coverage was about 5%.

CVs showing the hydrogen ad/desorption and Pt oxidation and reduction are depicted in Figure 4.3-1. The curves were evaluated as described in previous sections.

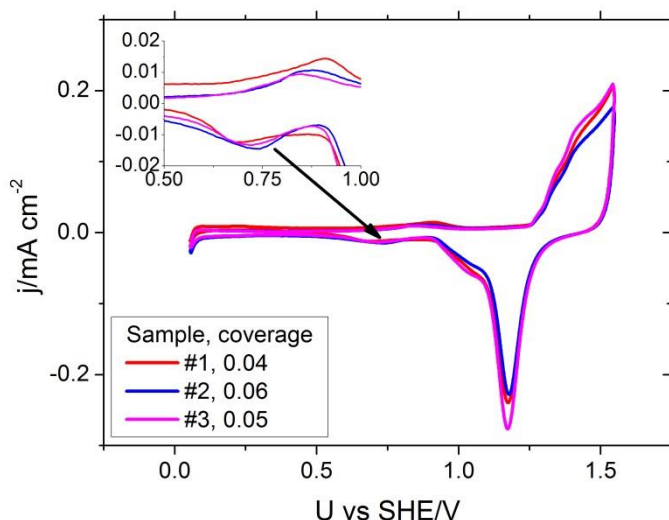


Figure 4.3-1 Hydrogen ad-/desorption and Pt oxidation and reduction for spherical Pt nanoparticles on Au(111) as measured via CV. Sample #1 was not annealed, sample #2 was annealed for 10s at a temperature of 300°C and sample #3 was annealed for 10min at 300°C in air.

In Figure 4.3-2 CO-adlayer oxidation is shown for the three samples. For sample #1, which was not annealed, no dominant peak can be observed. Here, CO is oxidized in a potential range from 0.85V to 1.3V vs. SHE continuously. CO adsorbed on samples #2 and #3 is oxidized in a potential range from 0.7V to 1.25V vs. SHE. However, for these two samples, which both were annealed, an oxidation peak is found at a potential of 0.85V vs. SHE. Once again the CO-adlayer oxidation measurements of Friedrich and coworkers, for spherical Pt nanoparticles on polycrystalline Au, serve as a comparison [145]. The mentioned publication includes CO-adlayer oxidation CVs for Pt nanoparticles with a diameter of 10nm, which is similar to the diameter of the spherical Pt nanoparticles of our investigations (compare with following section on AFM characterization). The CO adsorbed on Pt particles, which were investigated by Friedrich et al., is oxidized between 0.8V and 0.95V vs. RHE in one single peak with a peak potential of 0.87V vs. RHE for a coverage of 0.013 (Figure 6 in the publication); a value which is quite close to the peak potential found in this study. For higher coverage the peak broadens, which is the case for the data presented in this work (see Figure 4.3-2). Due to this accordance, the CO-adlayer oxidation charge is related to the one found by Friedrich et al. of $q \approx 600 \mu\text{C}/\text{cm}^2$ (particle diameter $\sim 10\text{nm}$, coverage 0.013; the value was calculated from the image shown in the publication because it was not mentioned in the text). Since the CV of sample #1 differs from the other two, it is possible that the particles didn't adhere properly to the Au(111) surface, because this sample was not annealed. Therefore, the

characteristics of 10nm-sized particles cannot be seen in the corresponding CO-adlayer oxidation CV.

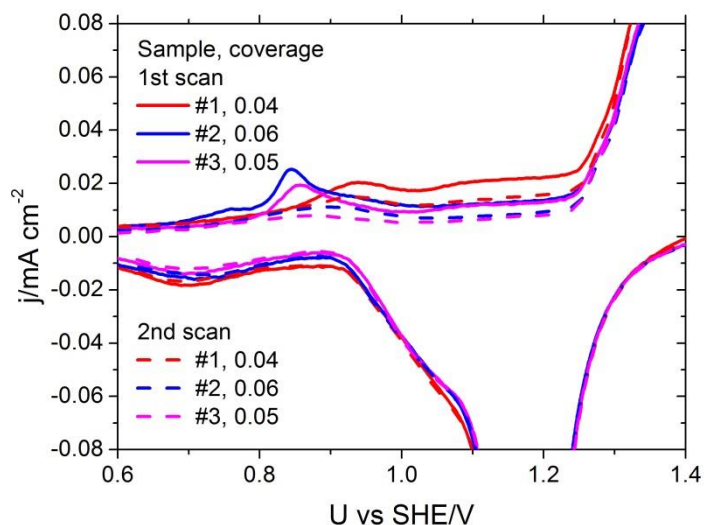


Figure 4.3-2 CO-adlayer oxidation for spherical Pt nanoparticles on Au(111). CO was adsorbed on the Pt-particle surface and oxidized during the first scan of the CV in a potential range from 0.7 to 1.25V vs. SHE. The second scan is shown for better visibility of the CO-adlayer oxidation peak.

A comparison of the coverage evaluated with the adsorption and oxidation measurements and the mean coverage for the three samples is given in Table 5. The three coverage values determined by the different methods differ slightly for sample #1, whereas for #2 and #3 they are very similar.

Table 5 Pt coverage determined by hydrogen ad/desorption, CO-adlayer oxidation and PtO_x-reduction measurements. Mean coverage was calculated as average of the three coverages given for each sample.

Sample #	Duration of heat treatment at 300°C	Pt coverage, determined via			Mean coverage
		Hydrogen ad-/desorption charge	CO-adlayer oxidation charge	PtO _x reduction charge	
1	-	0.02±0.01	0.04±0.01	0.06±0.01	0.04±0.02
2	10s	0.06±0.01	0.06±0.01	0.06±0.01	0.06±0.01
3	10min	0.05±0.01	0.05±0.01	0.05±0.01	0.05±0.01

For further characterization, TM-AFM images were recorded before and after electrochemical measurements. As already discussed before, the width of the particles is not correctly imaged by the cantilever, since its diameter is of similar size as the Pt particles. Therefore, only the measured height was considered reliable. The approximate width of the particles was determined by STM measurements of sample #3 after electrochemical measurements. The

STM image shows that particles had a width of $(7\pm 1)\text{nm}$ and a height of $(5\pm 1)\text{nm}$ (compare with Figure 4.3-3). The average height of the Pt particles of sample #3 after electrochemical measurements, as derived from AFM images, of $(5.0\pm 2.3)\text{nm}$ (compare with Figure 4.3-6), corresponds to the height measured by STM. Therefore their width seems to slightly exceed their height, which may be due to a slight compression or change in shape when they attach at the Au surface and/or the plasma-etching step. During the STM measurement some Pt nanospheres were moved by the STM tip (Pt tip) due to a strong interaction between tip and particles. Therefore, particles are not considered to be imaged at their initial location.

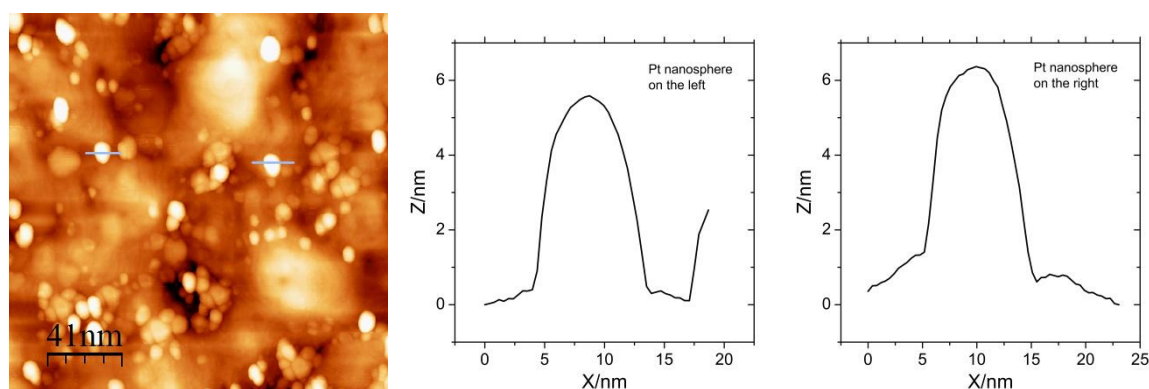


Figure 4.3-3 STM image of sample #3 after electrochemical measurements and line scans of two Pt particles. The left Pt nanosphere is $(5.0\pm 0.5)\text{nm}$ high and $(7.5\pm 0.5)\text{nm}$ wide, the right one is $(5.2\pm 0.5)\text{nm}$ high and $(7.0\pm 0.5)\text{nm}$ wide. Some particles were moved by the STM tip (Pt tip), due to a strong interaction between tip and particles.

TM-AFM images of samples #1-3 before and after electrochemical measurements are depicted in Figure 4.3-4 to Figure 4.3-6, respectively. The mean particle height was evaluated with these images. An additional image of another part of the sample was evaluated for each sample. Thus, the height of approximately 170 particles was measured in each case. Since the exact shape of the particles was unclear, Pt coverage was calculated by assuming a spherical shape with the radius corresponding to half the measured height and by assuming a hemispherical shape with the radius of the hemisphere corresponding to the measured height (compare with Figure 4.3-7). In Table 6 these values are summed up.

When comparing the AFM images of samples #1-3 before and after electrochemical measurements, it is observed that the particle height is smaller after electrochemical measurements. The effect is very pronounced for samples #1 and #3, whereas the change in particle height is very small for sample #2. The decreasing height with electrochemical measurements can be due to a higher mobility of Pt atoms and/or a loss of Pt during oxidation-reduction cycles, i.e. during the activation procedure.

A comparison of the Pt-particle height of samples #1-3 before electrochemical measurements (see Table 6) shows, that the annealing procedure led to a decrease in particle height. Annealing at 300°C for 10s (sample #2) resulted in a decrease of 0.5nm, annealing at 300°C for 10min (sample #3) resulted in a decrease of 2.3nm compared to the initial non-annealed state. Furthermore, the particles of samples #2 and #3 were probably better attached to the surface. Annealing for 10min (sample #3 before EC) additionally decreased particle height, which presumably led to an even better adhesion of the particles on the Au(111) surface. Pt coverage, calculated from images taken after electrochemical experiments, is slightly smaller for samples #1 and #3, when compared to the initial coverage. This is probably due to the electrochemical activation procedure, which might lead to partial dissolution of Pt. Such an effect was not seen for sample #2. If also Pt coverage determined by electrochemical adsorption/oxidation measurements is taken into account, it is apparent that for all samples the assumption of spherical particles, with a radius of half their height, matches best.

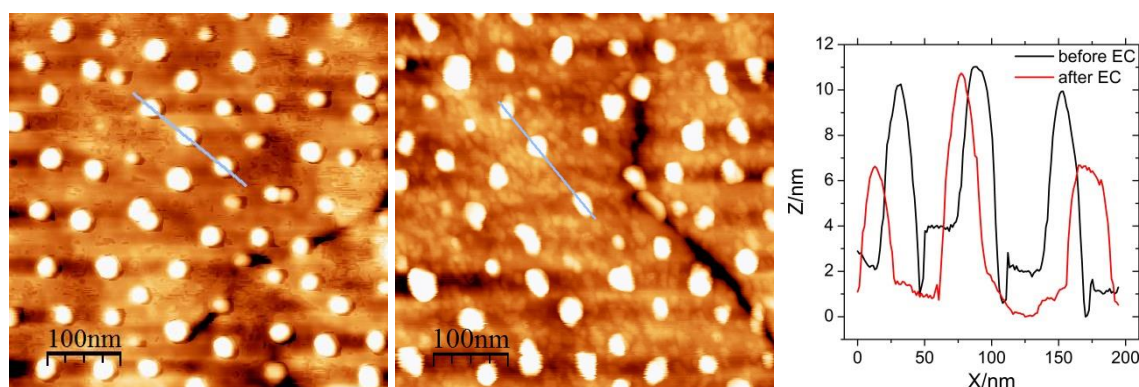


Figure 4.3-4 TM-AFM images of sample #1 before (left) and after electrochemical measurements (middle) and corresponding line scans (right). Particles are about 7nm high and the distance of neighboring particles is between 60nm and 70nm.

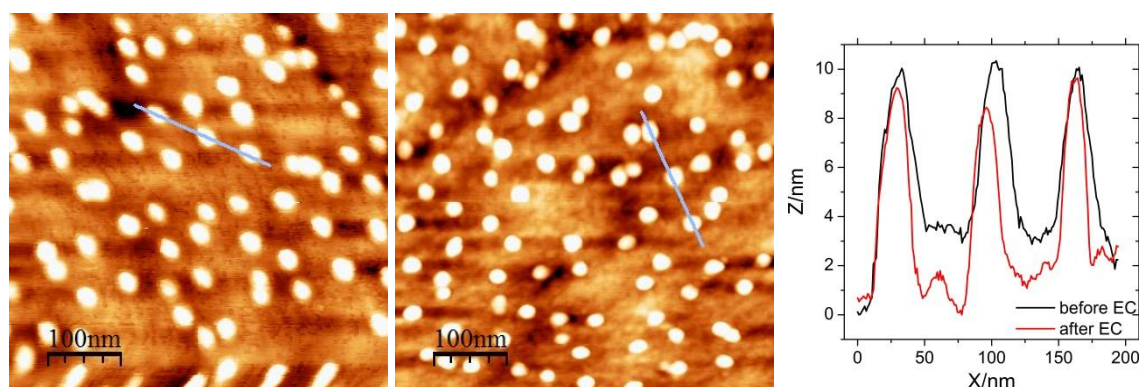


Figure 4.3-5 TM-AFM images of sample #2 before (left) and after electrochemical measurements (middle) and corresponding line scans (right). Particles are about 7nm high and the distance between neighboring particles is between 50nm and 60nm.

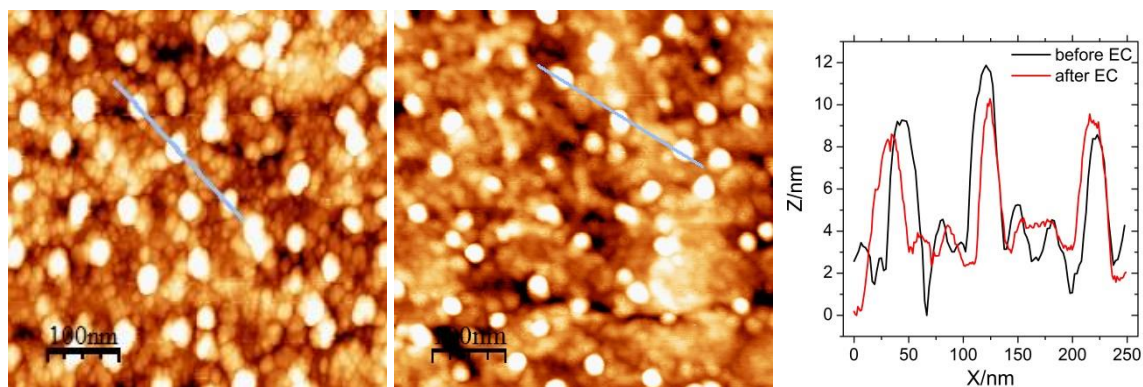


Figure 4.3-6 TM-AFM images of sample #3 before (left) and after electrochemical measurements (middle) and corresponding linescans (right). Particles are about 6 and 5nm high before and after electrochemical measurements, respectively, and the distance between neighboring particles is between 60nm and 70nm.

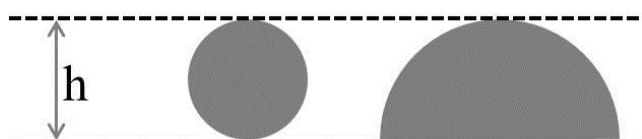


Figure 4.3-7 Two possible shapes of the Pt particles: A sphere with radius $h/2$ and a hemisphere with radius h .

Table 6 Summary of values determined and calculated from TM-AFM images. For comparison the mean Pt coverage determined by electrochemical measurements is included. (EC=electrochemical measurements)

Sample, description	Mean particle height/nm	Pt coverage calculated by assuming a spherical shape	Pt coverage calculated by assuming a hemispherical shape	Mean Pt coverage from electrochemical measurements
#1, before EC	7.2 ± 2.1	0.05 ± 0.02	0.10 ± 0.03	--
#1, after EC	6.4 ± 2.3	0.04 ± 0.02	0.07 ± 0.02	0.04 ± 0.02
#2, before EC	6.7 ± 1.6	0.05 ± 0.02	0.09 ± 0.03	--
#2, after EC	6.6 ± 1.7	0.05 ± 0.02	0.10 ± 0.03	0.06 ± 0.01
#3, before EC	5.9 ± 2.8	0.05 ± 0.02	0.11 ± 0.03	--
#3, after EC	5.0 ± 2.3	0.04 ± 0.02	0.08 ± 0.02	0.05 ± 0.01

4.3.2 Dependence of electrocatalytic activity on particle height

In Figure 4.3-8 Tafel plots of the kinetic and Pt-specific HER- and HOR-current densities are shown for the Pt nanospheres on Au(111) described in the previous section. For comparison, current densities for Pt nanoislands on Au(111) with similar Pt coverage and for a Pt(111) single crystal are shown. Pt nanoislands on Au(111) were fabricated by dipping and single pulse deposition. However, before HER-/HOR-measurements the samples were oxidized and

reduced in 1M HClO₄, in order to guarantee an equal pretreatment as for the spherical Pt nanoparticles (compare with previous section). Pt-specific current density was calculated as ratio of kinetic current density and mean Pt coverage. The kinetic current density was evaluated as described in section 3.4.5 (p. 53ff.). Therefore, the RC-time constant $\tau=R_{\Omega}C_{DL}$ was calculated, which was about 7 μ s ($R_{\Omega}\approx 0.3\Omega$, $C_{DL}\approx 13\mu$ F) for all samples and the linear fit was performed in a time range of 30 to 100 μ s. The influence of the double-layer charging current in this time range of about 0.01I_{0a} (compare with section 3.4.5) is thus very small.

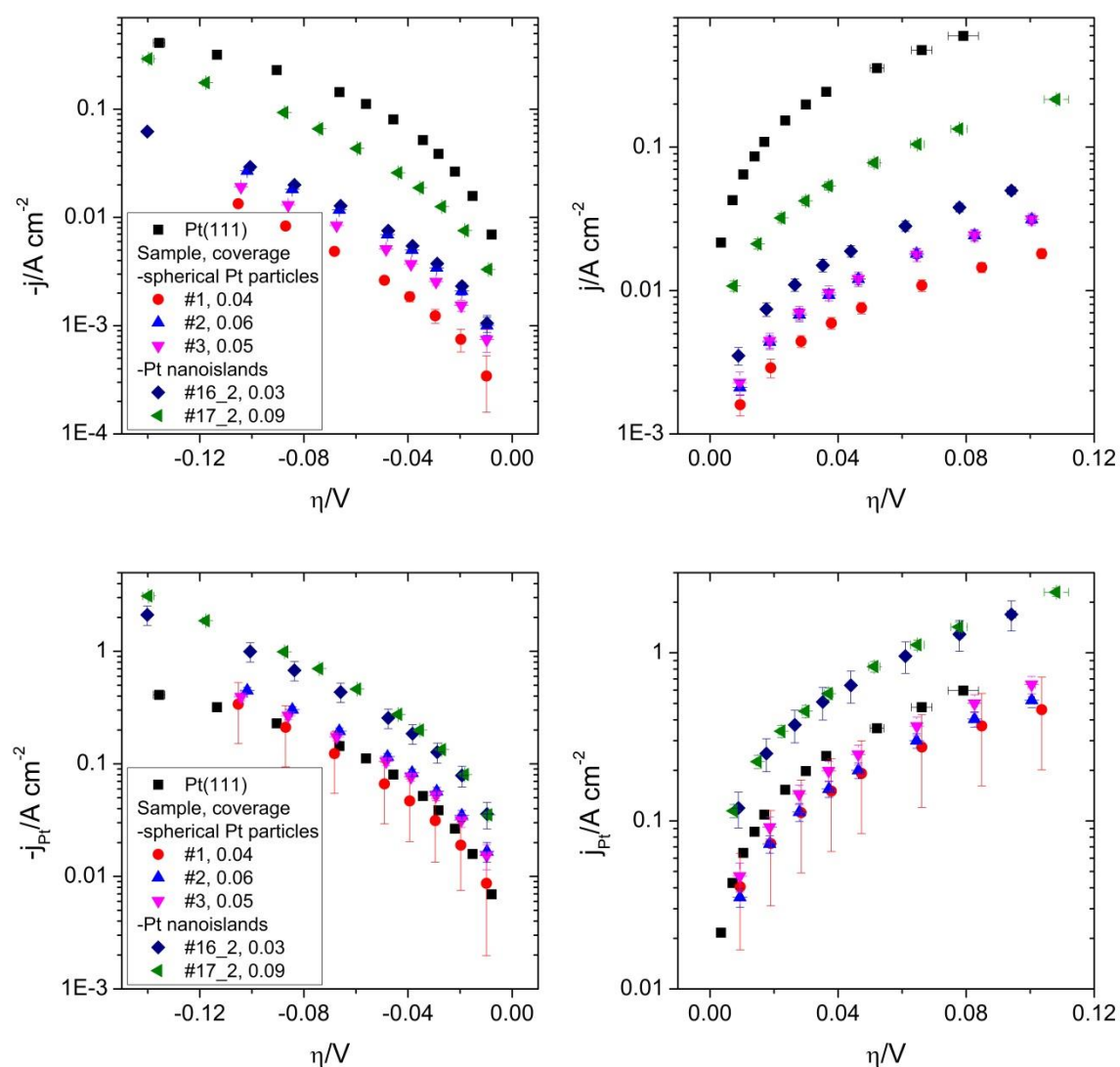


Figure 4.3-8 Tafel plots of the kinetic current density j (upper part) and the Pt-specific current density j_{Pt} (lower part) for the HER (left) and the HOR (right) at spherical Pt nanoparticles and Pt nanoislands on Au(111) and at Pt(111) in 1M HClO₄. The electrolyte was saturated with H₂.

Comparing the kinetic current densities of the samples shown in the Tafel plots (Figure 4.3-8), a similar trend as in section 4.1 (p. 57ff.) can be seen: The highest kinetic current

density is measured for Pt(111). For Pt nanoislands on Au(111) kinetic current densities increase with increasing Pt coverage. Below these values the kinetic current densities for the Pt nanospheres on Au(111) follow the same trend as the Pt-nanoisland samples: Currents increase with increasing coverage. Considering the Pt-specific current densities shown in the Tafel plots, it becomes apparent that the activity of Pt nanoislands on Au(111) is higher than the activity of the spherical Pt nanoparticles on Au(111), which is similar to the activity of a Pt(111) single crystal. A comparison of the Pt-specific current densities of these samples for overpotentials of $\eta = \pm 0.02\text{V}$, $\pm 0.04\text{V}$ and $\pm 0.06\text{V}$ (see Figure 4.3-9, specific current density is only shown for $\eta = \pm 0.02\text{V}$ because of equal trends), which were determined by linear interpolation of the Tafel plots, leads to the following conclusions: The activities of a Pt(111) single crystal and of Pt nanospheres on Au(111) are similar. However, for HOR, Pt(111) activity is slightly higher than Pt-nanosphere activity. A pronounced difference is seen between Pt nanoislands and Pt nanospheres for both reactions, HOR and HER: The activity of “two-dimensional” Pt nanoislands on Au(111) is more than twice as high as the activity of Pt nanospheres on Au(111).

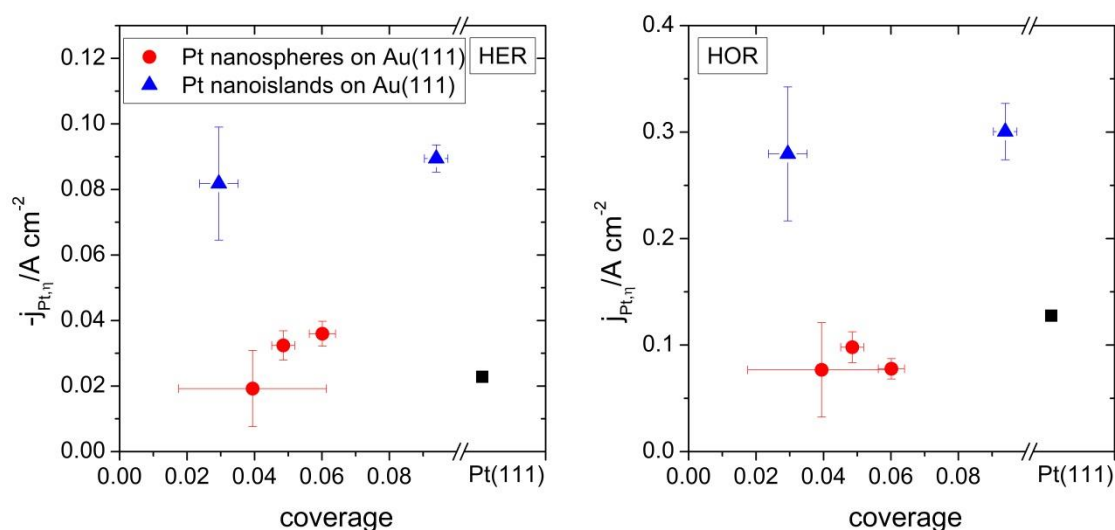


Figure 4.3-9 Specific current densities $j_{Pt,\eta}$ for HER (left) and HOR (right) at an overpotential $\eta = \pm 0.02\text{V}$ for a Pt(111) single crystal (black square), Pt nanospheres on Au(111) (samples #1-3, red circles) and Pt nanoislands on Au(111) (samples #16_2 and #17_2, blue triangles).

Considering the results of section 4.1 (p. 57ff.), which dealt with various Pt coverages on Au(111) one could argue that the different electrocatalytic activities in these investigations might as well be due to a coverage-determined effect. Therefore, the specific current densities at an overpotential $\eta = \pm 0.02\text{V}$, calculated from HER-/HOR-Tafel plots of the Pt nanoislands on Au(111), which were presented in section 4.1.2 (p. 64ff.), were compared with the ones of

Pt nanospheres on Au(111) (see Figure 4.3-10). This plot shows, that the activity of Pt nanospheres is in fact smaller than the activity of Pt nanoislands on Au(111). In the case of the HER the activities of Pt nanospheres are similar to the ones of Pt(111) and of high coverages c ($c > 0.3$) of Pt nanoislands on Au(111), but well below the activities of small coverages of Pt nanoislands on Au(111). In the case of the HOR the activities of Pt nanospheres are slightly below the one of Pt(111) and considerably smaller than the ones of Pt nanoislands on Au(111).

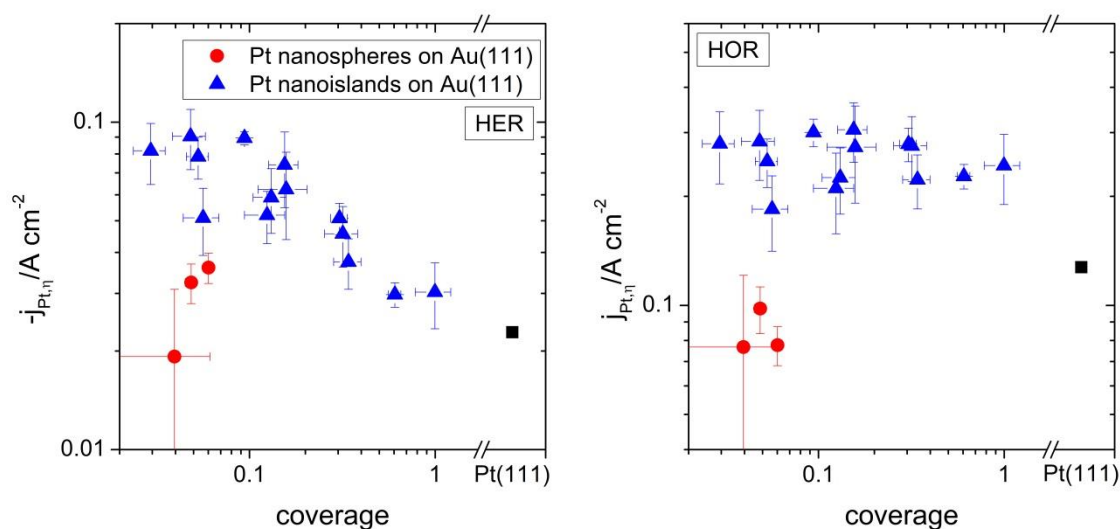


Figure 4.3-10 Comparison of Pt-specific current densities $j_{Pt,\eta}$ at an overpotential $\eta = \pm 0.02V$ calculated from HER-/HOR-Tafel plots, for Pt nanospheres on Au(111), Pt nanoislands on Au(111) and Pt(111).

4.4 Electrochemical properties of defined nanostructure arrays

Nanoimprint lithography (NIL) and nanotransfer printing (nTP) are nanostructuring techniques, which are usually employed in semiconductor research. Many different materials were therefore printed on or transferred to Si substrates. The following section aims at a demonstration of the applicability of such structures in electrochemical measurements.

Nevertheless, the main objective of this approach was to verify the spillover effect for the HER and the HOR at Pt nanoislands on Au. Therefore, NIL and nTP were used to establish defined arrays of Au lines and pillars. The Au lines were then electrochemically coated by Pt nanoislands. Their electrocatalytic activity was expected to be lower than the activity of Pt nanoislands on extended Au surfaces. On an extended Au surface spillover can proceed in all directions. However, on a limited Au surface, such as for example on Au lines, spillover is assumed to be partially inhibited. Therefore, Pt-nanoisland activity was expected to be lower on Au lines than on extended Au surfaces.

4.4.1 Gold pillars on highly doped silicon

In this section, first investigations of Au pillars in an electrochemical setup will be presented. The Au pillars were established on highly p-doped Si by nTP. With this approach, the Au surface surrounding electrochemically deposited Pt nanoislands can be decreased systematically. With decreasing diameter of the Au pillars spillover should be inhibited almost completely. This is expected to be reflected in a decreasing activity of the Pt nanoislands and a much lower activity than measured for Pt nanoislands on extended Au surfaces.

In these first investigations the diameter of the Au pillars was kept at 100nm. A major challenge of such an electrode configuration is the establishment of an electrical contact to the Au pillars: They are not connected by a metallic contact but through the Si surface. Therefore, the electrochemical properties of the Au pillars have to be characterized thoroughly in order to allow for comparison with extended Au surfaces.

4.4.1.1 Characterization by TM-AFM

Au pillars were fabricated as described in section 3.2.2 (p. 41ff.). TM-AFM images of such structures were recorded before and after electrochemical measurements. Several images of the as-prepared structures of samples PBPi04 and PBPi05 are shown in Figure 4.4-1 and

Figure 4.4-2, respectively. The pillars on each sample are very similar in size and only very few missing pillars, about 1-2%, can be seen. On sample PBPI04 the pillars have a diameter of $(110\pm 5)\text{nm}$, the spacing is $(170\pm 5)\text{nm}$ (from center to center) and their height is $(45\pm 5)\text{nm}$. On sample PBPI05 the pillars have a diameter of $(110\pm 5)\text{nm}$, the spacing is $(170\pm 5)\text{nm}$ and their height is $(30\pm 5)\text{nm}$. Thus, size and spacing are quite reproducible. Only the height of the pillars was varied, which is determined by the quality of the SAM on the nTP-mold and by the varying thickness of the metal layers evaporated on the mold.

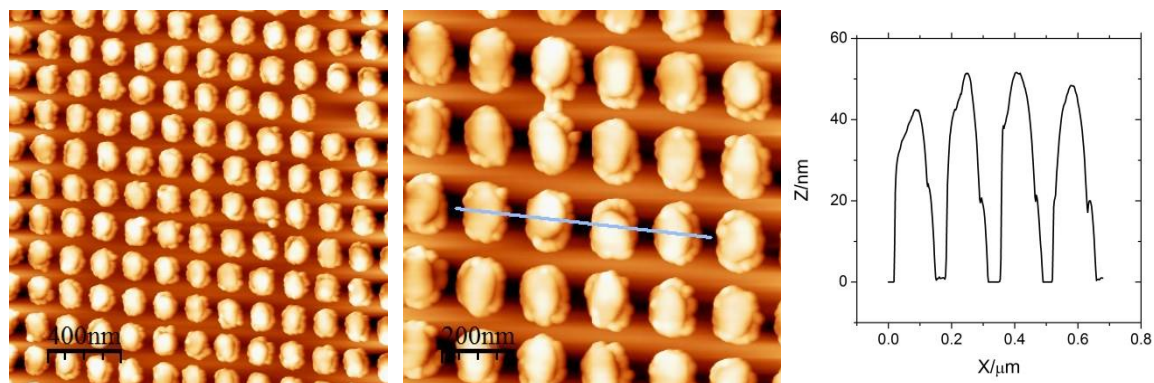


Figure 4.4-1 TM-AFM images of Au pillars on sample PBPI04 with different magnifications and a corresponding line scan, recorded before electrochemical measurements. The diameter of the pillars is $(110\pm 5)\text{nm}$, the spacing is $(170\pm 5)\text{nm}$ and the height of the pillars is $(45\pm 5)\text{nm}$.

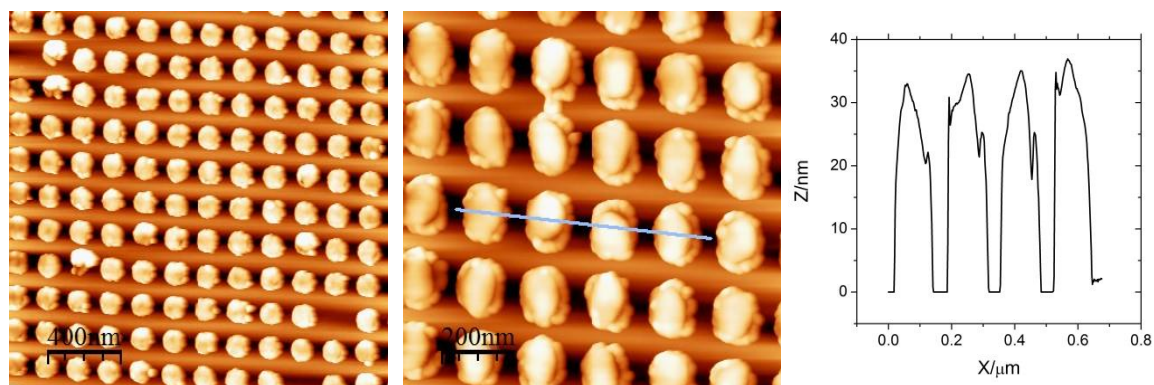


Figure 4.4-2 TM-AFM images of Au pillars on sample PBPI05 with different magnifications and a corresponding line scan, recorded before electrochemical measurements. The diameter of the pillars is $(110\pm 5)\text{nm}$, the spacing is $(170\pm 5)\text{nm}$ and the height of the pillars is $(30\pm 5)\text{nm}$.

TM-AFM images of sample PBPI04 captured after the electrochemical measurements are depicted in Figure 4.4-3. The size of the pillars and their spacing was maintained during the electrochemical measurements, which can be seen from AFM images and corresponding line scans before and after electrochemical measurements. Nevertheless, about 15% of the pillars were detached and nearly all of them reattached at another pillar/other pillars in the close vicinity of their previous place. In electrochemical measurements the mobility of the Au

pillars on the Si surface, if not properly attached, is enhanced and their detachment is facilitated compared to dry conditions. This detachment is related to the properties of the Ti layer under the Au layer. For instance, if the Ti layer is too thin or was not attached properly to the Si surface, the pillars are detached easily from the Si surface, since the adhesion of Au is very poor on Si substrates.

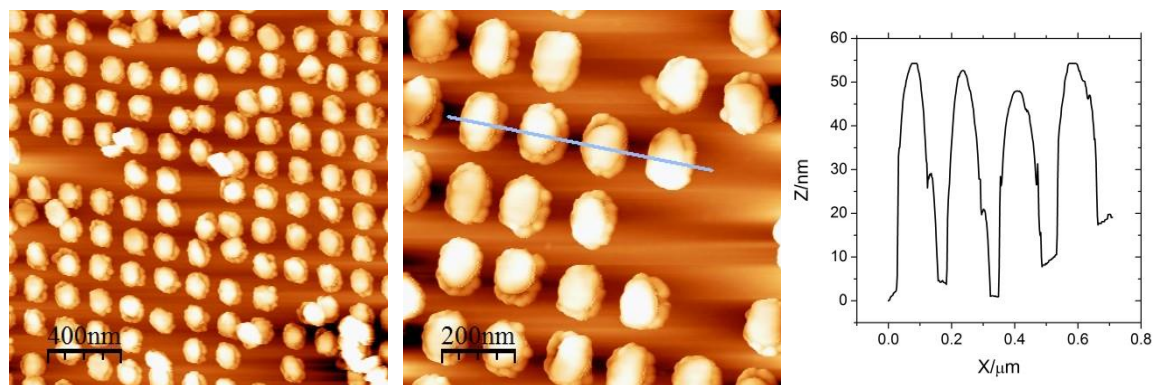


Figure 4.4-3 TM-AFM images of Au pillars on sample PBPI04 with different magnifications and a corresponding line scan, recorded after electrochemical measurements. The diameter of the pillars is $(110\pm 5)\text{nm}$, the spacing is $(170\pm 5)\text{nm}$ and the height of the pillars is $(45\pm 5)\text{nm}$.

From the dimensions determined by the TM-AFM images, the pillar density and the Au-surface area can be calculated. With respect to the constant spacing of $(170\pm 5)\text{nm}$ for both samples the pillar density is $(3.5\times 10^9 \pm 0.3\times 10^9)/\text{cm}^2$ on the structured surface. The Au surface, assuming a cylindrical shape of the pillars, is $(7.8\times 10^{-4} \pm 2.9\times 10^{-4})\text{cm}^2$ on PBPI04 before and after electrochemical measurements, since the detached Au pillars reattached and therefore also had electric contact. On PBPI05, the Au surface is $(6.2\times 10^{-4} \pm 2.3\times 10^{-4})\text{cm}^2$.

4.4.1.2 Applicability in electrochemistry

A suitable method to compare a newly fabricated Au structure with an extended Au surface for electrochemical means is usually done by CV. Characteristic features of the CVs have to appear in the same potential regions to make sure, that the electrochemical behavior corresponds to one another. Thus, the regimes of Au oxidation and reduction as well as oxygen and hydrogen evolution were compared in 1M HClO₄. Such investigations were conducted for the Au pillars on Si (PBPI04) and for an extended Au layer on a glass substrate (compare with section 3.2.1, p. 40ff.), which was not annealed. Additionally an extended, sputtered Au layer (height ~20nm) on a p-doped Si sample with a Ti layer in between for adhesion, which was fabricated like the Au/Ti deposit on the nTP-mold and contacted through the rear part of the Si sample, like the Au pillars, was also characterized via CV. This

investigation was performed to make sure that the contact through the rear part of the Si substrate did not introduce any semiconductor-related characteristics or a large Ohmic resistance. A CV at the pure Si surface, which was also contacted at the rear side, is included for comparison. Since the Si served as a conducting support material only and the Au pillars' behavior was to be studied, an influence of the Si surface was not eligible. Si was therefore believed to be very well suited for such measurements because of its natural surface oxide. An electrochemical reaction of the Si surface with electrolytes is usually only seen in highly concentrated potassium hydroxide (3-15M KOH) and hydrofluoric acid (HF) [162-166].

CVs of the oxygen evolution regime for the above mentioned samples in Ar-purged 1M HClO₄ are depicted in Figure 4.4-4. On the left the geometric current density at the pure Si surface and at the Au pillars on Si is shown. The current measured at the Si surface was also subtracted from the current measured at the pillar sample and included in the CV. On the right, CVs of the Au-oxidation and -reduction reaction and of the oxygen evolution reaction (OER) at the different Au surfaces are shown. Au-specific current density j_{Au} was calculated by relating the measured current to the Au surface area, which was determined by integration of the Au-oxidation current for the extended Au films on glass and on Si, as described in section 3.4.4.1 (p. 51f.). The determination of U_{min} for such an evaluation was straight forward for these samples. However, the sample with Au pillars on the Si surface does not show a distinct current minimum. Therefore the Au pillars' surface area was calculated by integration of the Au-reduction peak. In the case of the extended Au surfaces, the values determined by integration matched well with the calculated ones (compare with Table 7). The Au pillars' surface on the Si substrate is similar to the one calculated from AFM measurements, but the two values differ somewhat. This is due to the more qualitative character of such a surface determination (compare with section 3.4.4.1).

Table 7 Comparison of the Au-surface area determined by electrode dimensions/Au-pillar dimensions and by Au-oxidation/-reduction charge.

Sample	Description	Au-surface area/cm ² , determined via	
		dimension of electrode surface/Au pillars (AFM)	Au-oxidation/-reduction charge
Au on glass	extended 250nm thick Au layer on glass	0.07±0.03	0.10±0.01
Au on Si	extended 20nm thick Au layer on Si	0.07±0.03	0.11±0.01
Au pillars	Au pillars on Si	$7.8 \cdot 10^{-4} \pm 2.9 \cdot 10^{-4}$	$2.1 \cdot 10^{-4} \pm 0.5 \cdot 10^{-4}$

Comparing the different CVs (Figure 4.4-4, right side), several important features are quite obvious: The double-layer capacity C_{DL} of the Au-pillar sample is much higher than that of the samples with extended Au surfaces. This is due to a rather high double-layer capacity of the Si surface, which could not be separated completely from the double-layer capacity of the Au pillars (compare with left side of the figure). Also, the current at potentials positive of 1.7V vs. SHE, i.e. in the oxygen evolution regime, is much higher at the sample with Au pillars, compared with the extended Au surfaces. This can be due to an enhancement of the oxygen evolution reaction (OER) by the Au pillars and/or an additional OER-current contributed by the Si surface. Furthermore, the oxidation of the Au surface starts at 1.24V vs. SHE for all samples, no matter if an extended Au layer or the Au pillars are investigated. Additionally, the Au_2O_3 reduction takes place in the same potential regime, i.e. from 1.30V to 0.95V vs. SHE, for these samples, and the peak potentials of the pillar-sample and the extended Au film on glass are very similar.

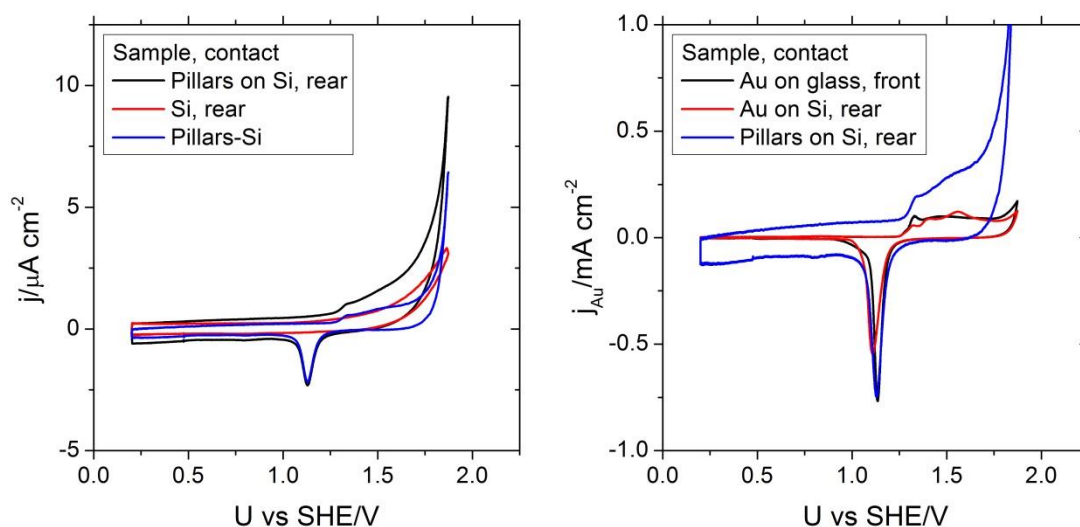


Figure 4.4-4 Comparison of CVs for Au oxidation/reduction and oxygen evolution reaction (OER) at different Au surfaces in Ar-purged 1M $HClO_4$: (i) extended Au layer deposited on glass, contacted directly on the Au surface, (ii) extended Au layer deposited on p-doped Si, contacted through the rear part of the Si sample and (iii) Au pillars on p-doped Si, also contacted through the rear part of the Si sample (PBPi04). Another CV at the pure Si surface is included in the left graph.

In Figure 4.4-5 the CVs of the HER in Ar-purged 1M $HClO_4$ at the different electrodes are shown. The current was again normalized to Au surface. As a precondition for that, the assumption was made that the Si surface of the Au-pillar sample is not active for hydrogen evolution. This assumption is based on the observation of strongly fluctuating current in the

HER-regime at a bare Si surface, which is very small compared to the current measured at an extended Au surface.

At a first glance, it seems that the onset potential of about -0.15V vs. SHE for the HER is very similar at the three electrodes (compare with left image of Figure 4.4-5). However, a closer look at the low-potential range (right image) shows that there is a slight difference: In spite of the slopes being very steep and similar, the activity for hydrogen evolution increases in the following sequence: extended Au layer on Si < extended Au layer on glass < Au pillars on Si. A higher activity of the extended Au layer on glass compared with the one on Si can be due to a more defined Au surface of the Au layer on glass, which is based on preparation conditions. The high HER-current measured at the Au pillars can be caused by a higher activity of the Au nanostructures compared with extended surfaces.

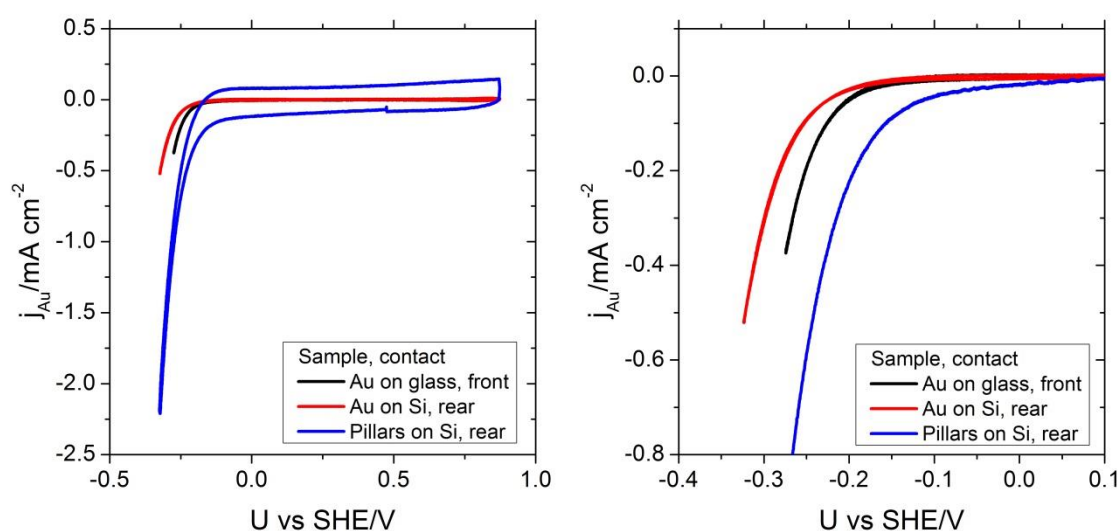


Figure 4.4-5 Comparison of CVs in the HER-regime at different Au surfaces in Ar-purged 1M HClO₄: (i) extended Au layer deposited on glass, contacted directly on the Au surface, (ii) extended Au layer deposited on p-doped Si, contacted through the rear part of the Si sample and (iii) Au pillars on p-doped Si, also contacted through the rear part of the Si sample. For better comparability, the right figure only shows the cathodic scan for the pillar-sample and the curve is shifted upwards. Since the double layer current is much more pronounced at this sample, this current is subtracted, because it does not contribute to the actual HER current.

It was quite important to find the Au oxidation/reduction of pillars and extended surfaces and the HER for these samples in approximately the same potential regimes. The differences of some 0.01V can be due to different properties of the different Au surfaces. A considerable shift to higher/lower potentials for oxidation/reduction reaction and to lower potentials for HER would indicate an influence of the semiconducting Si substrate on the Au pillars. In that case, it would be very difficult to compare the electrochemical properties of the Au pillars

with those of extended Au surfaces. However, even the small potential-shifts have to be further investigated and several more samples will have to be characterized.

Nevertheless, it was demonstrated that the Au pillars on Si are a suitable system for electrochemical experiments. Thus, it will also be possible to deposit Pt on the Au pillars and investigate the electrocatalytic activity of such electrodes.

4.4.2 Platinum nanoislands on gold lines between polymer lines

In the following, results of electrochemical measurements on Au lines with a width of about 160nm, fabricated by NIL, as described in section 3.2.2 (p. 41ff.), will be discussed. Pt was electrochemically deposited on these Au lines and HOR/HER was measured with potentiostatic single pulses. The activity of the deposited Pt nanoislands on Au lines was compared with the activity of Pt nanoislands on an extended Au surface.

As mentioned above, the motivation for such measurements is governed by the spillover effect. The electrocatalytic activity of Pt nanoislands on nanostructured Au lines is expected to be lower than on extended Au surfaces, due to a partial inhibition of the spillover effect. For Pt nanoislands, which are deposited in the vicinity of the border of an Au line (compare with Figure 4.4-6), spillover is diminished or inhibited in one direction. Such diminishment should be reflected in a decreased electrocatalytic activity of such an electrode.

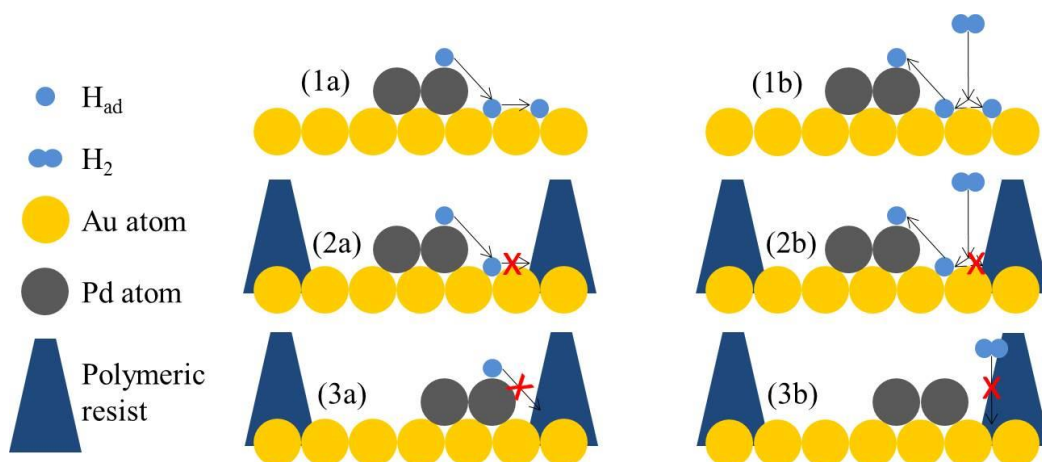


Figure 4.4-6 Spillover effect on different electrode structures during HER (a) and HOR (b): (1a+1b) On a conventional electrode consisting of Pt nanoislands on an extended Au(111) surface spillover is possible. (2a+2b)+(3a+3b) On nanostructured electrodes consisting of Pt nanoislands on Au lines spillover is diminished (2) or inhibited (3) in one direction, depending on the distance of the Pt nanoisland to the border of the Au line.

4.4.2.1 Characterization of support surface and platinum deposit

The Au surface with polymer lines was analyzed by TM-AFM to determine the width of the lines and their spacing. The width of the polymer lines was $(100\pm 10)\text{nm}$, their spacing $(260\pm 10)\text{nm}$ and consequently the width of the Au lines was $(160\pm 10)\text{nm}$ (compare with Figure 4.4-7).

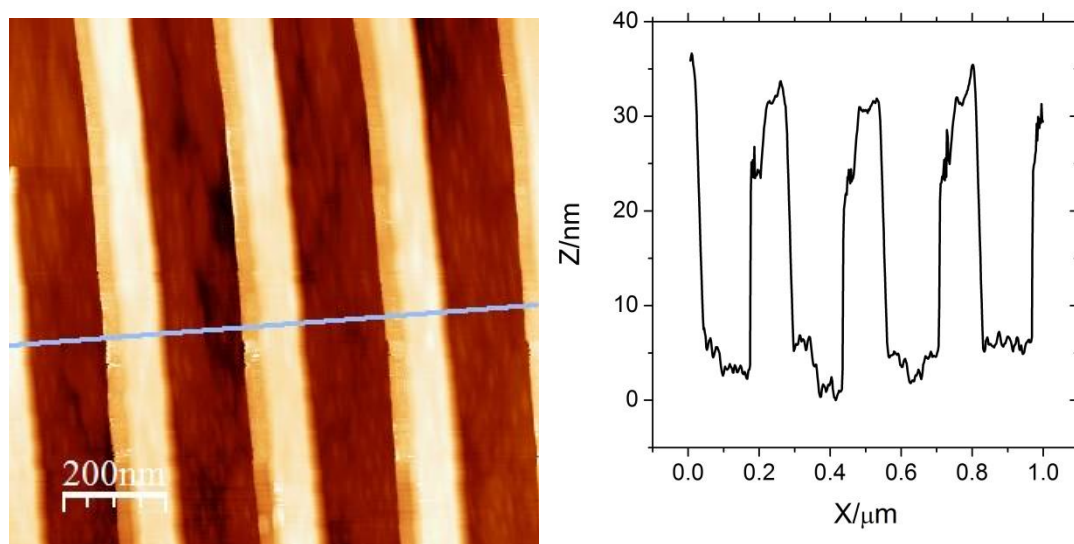


Figure 4.4-7 TM-AFM image and corresponding line scan of polymer lines (bright lines) on an Au surface (dark lines), established by NIL. The polymer lines are $(100\pm 10)\text{nm}$ wide and approximately 30nm high and the Au lines in between are $(160\pm 10)\text{nm}$ wide.

Since such samples were to be used in high concentrated electrolyte, such as 1M HClO_4 , the polymer had to be tested for its chemical stability therein. Thus, one of the samples was covered with 1M HClO_4 for more than one hour. When TM-AFM was performed on this sample, the images showed that polymer lines were still present and that there was no change in shape before and after electrolyte-treatment.

With these preconditions fulfilled, Pt could be deposited from $0.5\text{mM K}_2\text{PtCl}_6 + 1\text{M HClO}_4$ on the free Au lines between polymer lines. Thus, two samples were coated with Pt by the single pulse deposition method. For sample PB3 an overpotential of -0.26V and a deposition time of 0.5s was used, at sample PB4 an overpotential of -0.06V was applied for 0.5s . Subsequently, the samples were subjected to an oxidation-reduction sequence for activation (compare with section 4.3, p. 79ff.) and their activity for the HOR and HER was measured with potentiostatic pulses in hydrogen purged 1M HClO_4 .

As demonstrated in previous sections and shown by Kondo and coworkers [43], the Pt deposit is one atomic layer high in the case of small deposition overpotential (PB4) and several layers in the case of high deposition overpotential (PB3). The Pt deposit was characterized by

hydrogen ad-/desorption and PtO_x reduction. The procedures were carried out as described in the sections before. Corresponding CVs are shown in Figure 4.4-8.

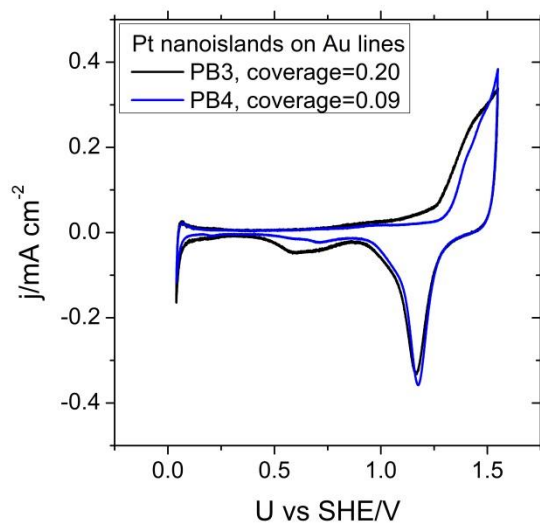


Figure 4.4-8 Oxidation and reduction cycles at samples PB3 and PB4 in Ar-purged 1M HClO_4 .

4.4.2.2 Dependence of electrocatalytic activity on the gold surface surrounding platinum nanoislands

The electrocatalytic activity of Pt nanoislands on Au lines was compared with the electrocatalytic activity of Pt nanoislands on extended Au surfaces. Similar Pt coverages were chosen for this comparison to exclude an influence of different coverages on activity. In Figure 4.4-9 Tafel plots for HER and HOR at Pt nanoislands on Au lines between polymer lines for the sample with high Pt coverage (PB3, coverage=0.20) and at Pt nanoislands on an extended Au(111) surface are shown. The corresponding Tafel plots for Pt(111) are also included.

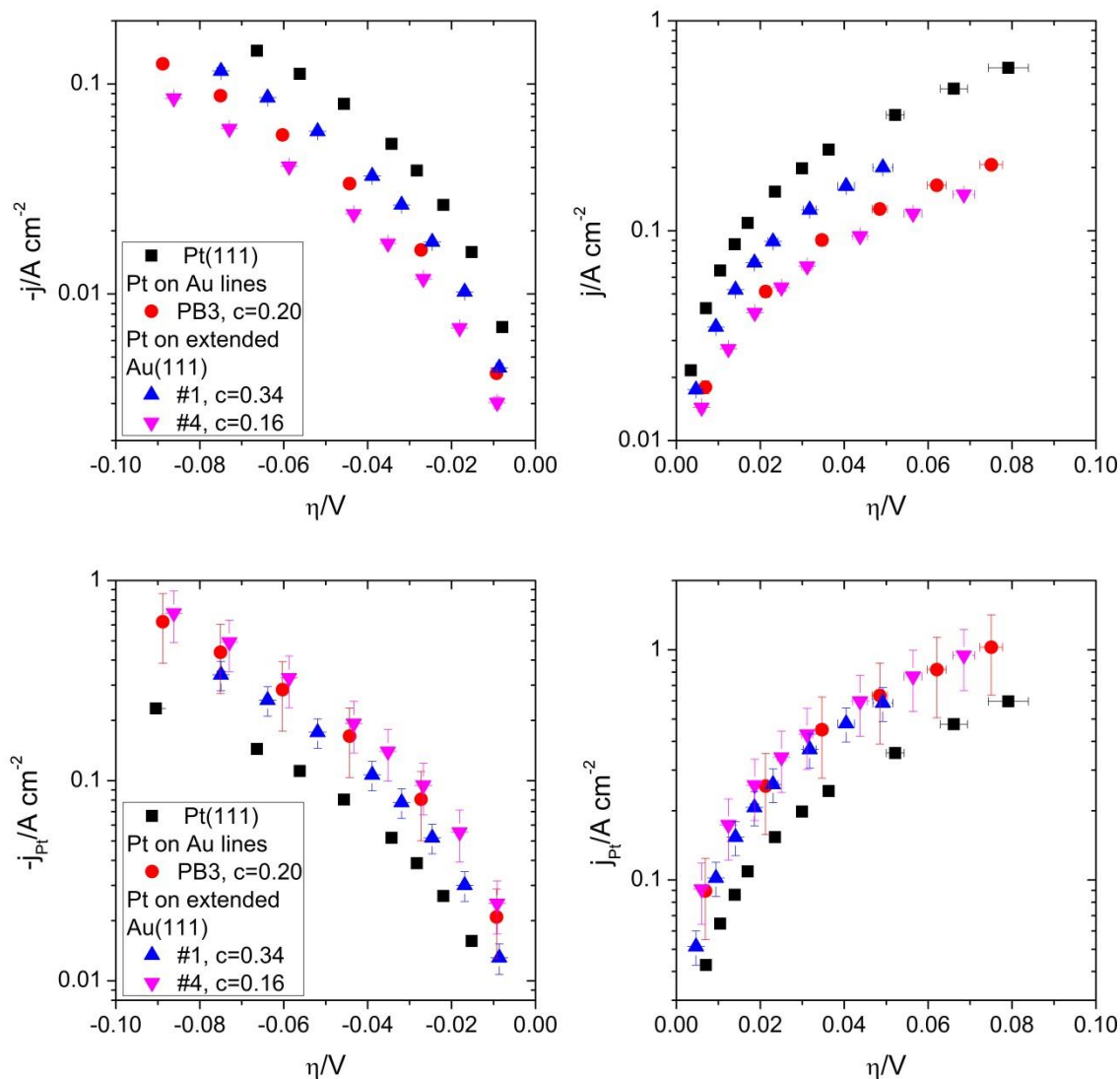


Figure 4.4-9 Tafel plots of the kinetic current density j (upper part) and the Pt-specific current density j_{Pt} (lower part) for the HER (left) and the HOR (right) at Pt(111) (black squares), at Pt nanoislands on Au lines between polymer lines (red circles) and at Pt nanoislands on extended Au(111) surfaces (triangles) in 1M HClO₄, with Pt coverage c . The electrolyte was saturated with H₂.

The kinetic current densities of the Tafel plots show the same behavior as in the studies before: They increase with increasing Pt coverage. Comparing the Pt-specific current densities of the samples with similar coverage (red circles and triangles), very similar activities for the HER and HOR are found, except for Pt(111) whose electrocatalytic activity is lower. Thus, as a general outcome no difference in activity can be recorded for rather high Pt coverage of about 0.2ML on Au lines and on extended Au surfaces.

In contrast, for smaller Pt coverage (0.09ML) there is a difference in activity when comparing Pt nanoislands on Au lines between polymer lines (PB4) and Pt nanoislands on extended Au(111) surfaces (see Figure 4.4-10): The kinetic current density of Pt nanoislands on Au

lines is considerably smaller than the one of Pt nanoislands on extended Au surfaces, although Pt coverage is very similar. The same situation is reflected by the Tafel plots of Pt-specific current density: For Pt nanoislands on extended Au(111) surfaces it is more than twice as high as for Pt nanoislands on Au lines between polymer lines. Interestingly, the activity of Pt nanoislands on Au lines between polymer lines is comparable to the one of Pt(111).

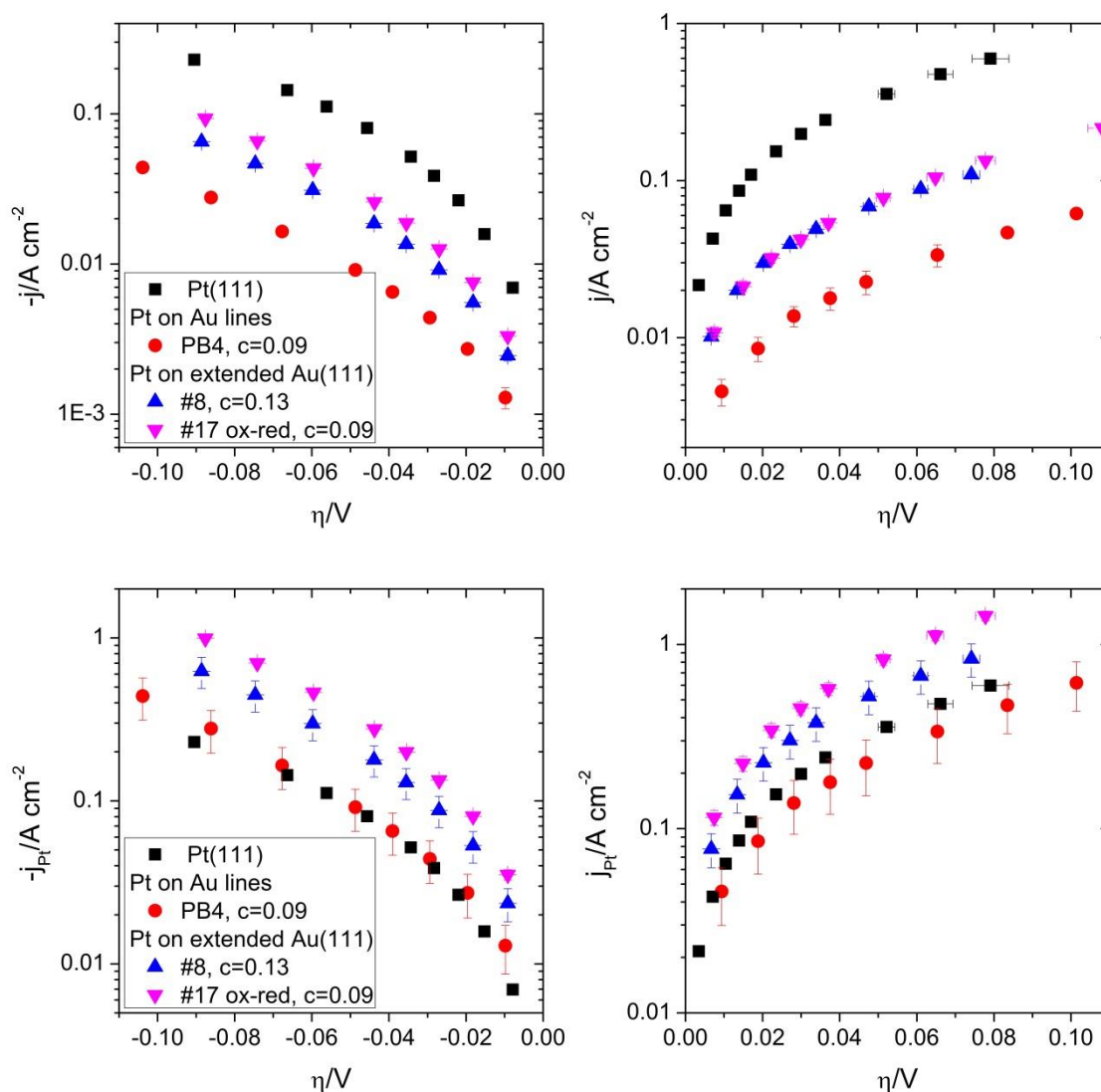


Figure 4.4-10 Tafel plots of the kinetic current density j (upper part) and the Pt-specific current density j_{Pt} (lower part) for the HER (left) and the HOR (right) at Pt(111) (black squares), at Pt nanoislands on Au lines between polymer lines (red circles) and at Pt nanoislands on extended Au(111) surfaces (triangles) in 1M HClO₄, with Pt coverage c . The electrolyte was saturated with H₂. Sample #17 was subjected to an oxidation-reduction sequence like sample PB4, for better comparison.

A comparison of the Pt-specific current densities of these samples and of Pt(111) for an overpotential of $\eta = \pm 0.02$ V (see Figure 4.4-11), which were determined by linear interpolation of the Tafel plots, leads to the following conclusions: The activities of a Pt(111)

single crystal and of Pt nanoislands on Au lines for a Pt coverage of 0.09 are similar. At this coverage a pronounced difference is seen between Pt nanoislands on an extended Au(111) surface and on Au lines: The activity of Pt nanoislands on extended Au surfaces is more than twice as high as the one of Pt nanoislands on Au lines. However, for a Pt coverage of 0.20 there is no difference in activity between Pt nanoislands on extended Au surfaces and Au lines.

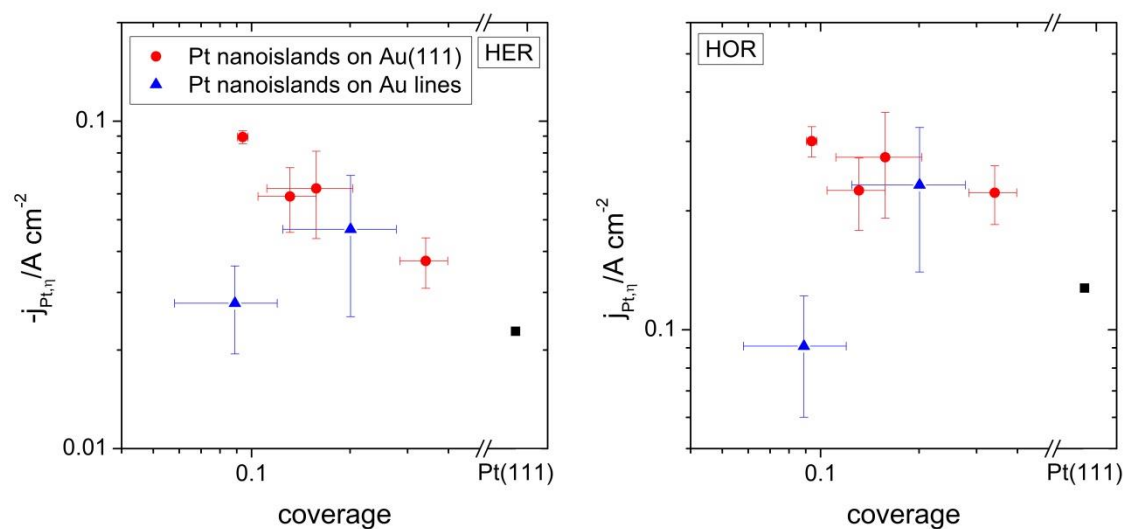


Figure 4.4-11 Specific current densities $j_{Pt,\eta}$ for HER (left) and HOR (right) at an overpotential $\eta = \pm 0.02V$ for a Pt(111) single crystal, Pt nanoislands on extended Au(111) surfaces and Pt nanoislands on Au lines.

5 Discussion

Any of the investigations, which were presented in the previous chapter, were carried out with the aim to contribute to a detailed understanding of the HER and the HOR at Pt nanostructures on Au surfaces. Spillover, strain and defect-density effect play a fundamental role in this context. Hence, the results of the different studies need to be discussed in this respect.

5.1 Platinum nanoislands on Au(111) – Double pulse deposition and dependence of electrocatalytic activity on deposition sites and coverage

In section 4.1 (p. 57ff.) electrochemical deposition of Pt on Au(111) in general and in particular double pulse deposition were analyzed. With this approach, the dependence of the electrocatalytic activity of Pt on Au(111) was investigated with respect to deposition sites, number of Pt nanoislands and Pt coverage. A summary of the results is given in the following:

- Four different deposition routines were applied: dipping, single and double pulse deposition as well as CV.
- Dipping at a potential positive of the equilibrium potential for Pt deposition yields a coverage of about 5% of a ML on the used Au(111) surfaces, which is mostly located on step and defect sites. Since this procedure is part of any deposition routine, deposition at step and defect sites cannot be prevented by e.g. choosing high deposition overpotential. Furthermore, a coverage lower than 5% of a ML cannot be achieved by electrochemical deposition, without any post-treatment such as for example oxidation of the metallic Pt.
- The fact that after dipping, a Pt coverage of about 5% of a ML could be determined is most probably due to adsorption of the $[\text{PtCl}_6]^{2-}$ complex on the Au surface [71]. The actual deposition takes place after the dipping procedure due to reduction of the adsorbed complex to metallic Pt when the potential is decreased during subsequent measurements.
- Via double pulse deposition the Pt-nanoisland size and the number of islands on terraces can be influenced. With increasing nucleation overpotential η_{nuc} the number of deposited islands increases and with increasing growth-pulse time t_{gro} the size of the islands increases.

- The activity of Pt nanoislands on Au(111) for HER and HOR was enhanced by a factor of three and two, respectively, when compared to bulk Pt(111). In the case of the HER (compare with Figure 5.1-1), a trend of increasing activity with decreasing Pt coverage is obvious. This is in contrast to the HOR, for which the activity of Pt nanoislands on Au(111) shows no clear trend with respect to coverage. For both reactions, the Pt nanoislands on Au(111) were found to be more active than a Pt(111) single crystal.

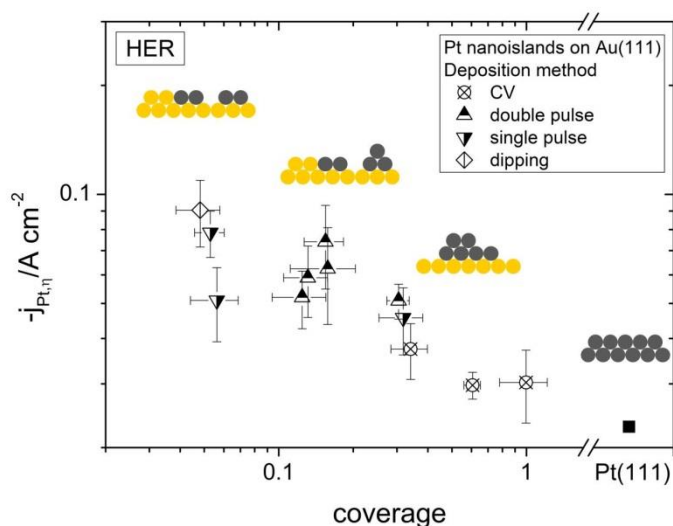


Figure 5.1-1 Pt-specific current density $j_{Pt,\eta}$ for the HER at an overpotential $\eta = -0.02V$, plotted versus coverage for different deposition methods. Several schemes of possible positions of Pt and Au atoms corresponding to deposition method and coverage are included.

The objective to demonstrate the suitability of double pulse deposition for the Pt/Au system was partly accomplished: Double pulse deposition of Pt on Au is characterized by the typical features, such as an increasing number of Pt nanoislands with increasing nucleation overpotential and an increasing island size with increasing growth-pulse time. However, due to the irreversible adsorption of the $[PtCl_6]^{2-}$ complex on the Au surface there is always a small amount of Pt, which is deposited in an uncontrolled way; also on step and defect sites. That is why the second goal, i.e. to determine a dependence of the electrocatalytic activity of Pt on Au(111) on deposition sites, island size and island number, was partly achieved, either: For HER and HOR one of the highest activities was exhibited by a dip-coated sample, for which Pt is mostly located on step and defect sites. Nevertheless, a controlled double pulse deposition of Pt with a defined number and size of islands, located mostly on terrace sites, would have brought additional knowledge on this system. In any case, the dependence of Pt activity on coverage was determined. An increasing activity with decreasing Pt coverage for HER can be due to strain, spillover and different adsorption sites of hydrogen atoms for different Pt coverage. A pronounced change in Pt activity for the HER is seen at a Pt coverage

between 0.3 and 0.5. For higher coverage the behavior is bulk-like, for lower coverage activities are considerably higher than Pt(111) activity. For HOR such a transition occurs from bulk Pt(111) to Pt nanoislands on Au(111). However, there is no clear trend for decreasing Pt coverage. The finding for both reactions, i.e. that the activity of Pt nanoislands on Au(111) is higher than the activity of Pt(111) is in line with the idea of spillover and with effects discussed in section 2.3 (p. 28ff.): Pt nanoislands on Au(111) may offer ideal adsorption sites for hydrogen atoms ($\Delta G_H \approx 0$).

5.2 Platinum nanoislands on defect-rich Au(111) – Spillover effect for the hydrogen oxidation reaction

In section 4.2 (p. 67ff.) the influence of defect density on an Au(111) surface on electrocatalytic properties of Pt nanoislands was evaluated. The particular goal of these investigations was the verification of the spillover effect for the HOR. An enhancement of the activity of Pt nanoislands on defect-rich Au(111) in comparison with Pt on defect-poor Au(111) was therefore expected to occur for the HOR, but not for the HER. In detail, the following results were achieved:

- Using potentiostatic single pulses with very small deposition overpotential, Pt deposits preferentially on step and defect sites of an Au(111) surface. In particular, Pt nanoislands deposit nearly exclusively on step and defect sites of a defect-rich Au(111) surface. At equal coverage, a higher number of Pt nanoislands was found on step and defect sites of a defect-rich Au(111) surface compared with a defect-poor Au(111) surface and attributed to the increased amount of step and defect sites on a defect-rich Au(111) surface. This was confirmed by comparing EC STM with hydrogen ad-/desorption, CO-adlayer oxidation and PtO_x-reduction measurements. EC STM images furthermore showed that the islands were mostly monoatomic in height.
- Pt-specific current density is higher by a factor of two for HOR and higher by more than a factor of three for HER on Pt nanoislands on defect-rich Au(111), when compared with Pt nanoislands on defect-poor Au(111). This shows that Pt nanoislands are more active on step/defect sites (compare with Figure 5.2-1).
- If Pt-specific current densities are plotted with respect to the part of Pt nanoislands that are located on the lower terrace of step/defect sites (see also Figure 4.2-12, p. 78), the enhancement nearly disappears for the HOR and decreases for the HER. This leads to the conclusion that the highest activity of Pt nanoislands investigated in this study is exhibited

by the ones on the lower terrace of Au(111) step/defect sites. Obviously, HOR and HER strongly depend on specific sites of the Au(111) surface where Pt nanoislands are located.

- Since in the above mentioned plot an enhancement is still observable for HER, not only the position of the Pt nanoislands but also the defect-rich Au(111) surface influences Pt activity.

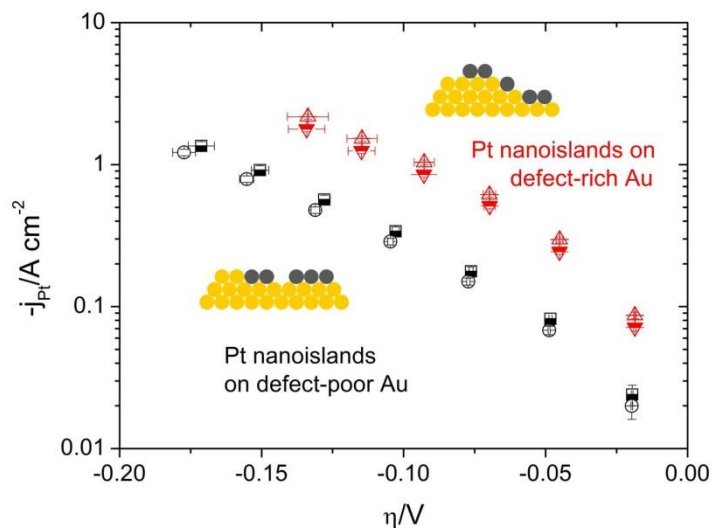


Figure 5.2-1 Tafel plot of the Pt-specific current density j_{Pt} for the HER at Pt nanoislands on defect-poor and defect-rich Au(111). Two schemes of the preferential positions of the Pt nanoislands on the Au surface are included.

The goal of verifying the spillover effect for the HOR was accomplished in part: An enhancement of Pt activity was demonstrated for Pt nanoislands on defect-rich Au(111) with respect to Pt nanoislands on defect-poor Au(111). However, such an enhancement also occurred for the HER. Therefore, in the case of HOR, a higher activity of Pt nanoislands on defect-rich Au(111) cannot be ascribed to spillover exclusively. Similarly to the implications of the investigations of the previous section, these results illustrate the interdependence of spillover and defect-density effect: The enhancement can either be due to a spillover of hydrogen atoms from the Pt nanoislands to the Au surface or vice versa. It can have its origin in different hydrogen adsorption energies for Pt nanoislands, which are located at different sites (defect or terrace sites). However, also a combination of both effects can lead to the observed correlation.

A detailed analysis of the possible role of (111)- and (100)-step sites on the Au(111) surface leads to the following interpretations:

- The HER-activity of Pt atoms on a (100) step of the Au(111) surface may be higher than on a (111) step, comparable to the Pd/Au system [40]. As mentioned in section 2.2.2 (p. 23ff.), the number of (100)-step sites on the defect-rich Au(111) surface is higher than on

defect-poor Au(111). This can be a reason for the more enhanced activity of Pt for the HER compared with the HOR.

- Considering the HOR, hydrogen dissociation is the basis for this reaction to proceed. Theoretical calculations showed an enhanced activity of (111)-step sites on Pt(111) compared with (100)-step sites for H₂ dissociation [106]. If this finding is transferable to Pt nanoislands forming (111) and (100) steps with the Au(111) surface, it can be a reason for the lesser enhancement of the activity of Pt on defect-rich Au(111) compared with the HER. Thus, for the HOR the (111) steps may be more beneficial.

The role of the defect sites of an Au(111) surface for the activity enhancement of Pt islands has not been analyzed in detail by theoretical means until now. However, the electronic structure of the Au(111) surface is definitely altered at defect sites because of the low coordination of the corresponding Au atoms. This also influences the electronic structure of Pt nanoislands attached to such Au atoms, which might for example lead to lower hydrogen adsorption energy and therefore facilitate HER and HOR. Moreover, the steps and defects on the Au(111) surface may enhance spillover by e.g. a higher adsorption energy for hydrogen atoms on these sites.

5.3 Relevance of strain: Platinum nanospheres compared with platinum nanoislands

In section 4.3 (p. 79ff.) the electrocatalytic activity of Pt nanospheres on Au(111), of Pt nanoislands on Au(111) and of Pt(111) was compared. Pt nanospheres were expected to be as active as Pt nanoislands on Au(111) and therefore considerably more active than Pt(111). Such a finding would have led to the conclusion that the electrocatalytic activity of Au surfaces that are partially covered by Pt is influenced by spillover and surface defects, but not by strain. However, these expectations were not met by the results of the investigations, which are summarized in the following:

- Using micellar diblock-copolymers, it is possible to generate a defined arrangement of Pt nanospheres on Au(111). It was demonstrated that such electrodes can be used for electrochemical investigations. In particular, they showed a good electrochemical performance, when they were annealed at 300°C for 10s and 10min.

- The activity of Pt nanospheres is comparable to the activity of Pt(111) and considerably smaller than the activity of Pt nanoislands on Au(111) with similar Pt coverage for HOR and HER (see Figure 5.3-1).

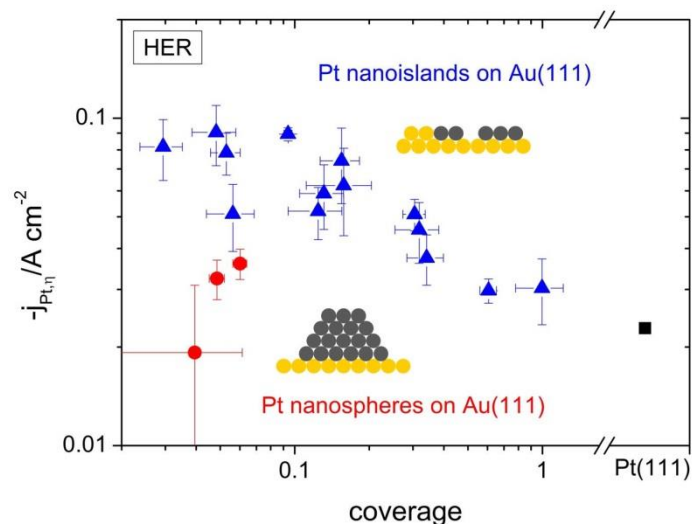


Figure 5.3-1 Pt-specific current density $j_{Pt,\eta}$ for the HER at an overpotential $\eta = -0.02V$, plotted versus coverage for Pt nanoislands and Pt nanospheres on Au(111) and for Pt(111). Schemes of Pt nanoislands and a Pt nanosphere on the Au surface are included.

This finding is in contrast to the expected behavior, i.e. the relevance of strain with respect to the electrocatalytic activity of Pt nanoislands on Au(111) could not be excluded. However, the finding is in line with recent DFT calculations for Pd on Au(111), which claim a higher activity of Pd nanoislands compared with bulk Pd, because strained nanoislands offer optimal adsorption sites for hydrogen atoms ($\Delta G \approx 0$, see also section 2.3.1, p. 29ff.) [40]. Since the Pt nanospheres with a height of 7nm are at least 20 atomic layers high, the lattice constant is equal or very close to the bulk value, except for the first few layers at the Pt-particle/Au-interface, which do not take part in the electrocatalytic reaction.

These results point out that strain plays an important role for the electrocatalytic activity of Pt on Au(111), since a considerable enhancement in activity only occurs for Pt nanoislands on Au(111). The results also indicate that spillover effect is very limited for Pt nanospheres on Au(111), since their activity is very similar to the one of bulk Pt(111). Therefore, the spillover effect is also connected to the height of the nanostructures. This means that spillover is closely related to strain. Thus, the experimental separation of the two effects is difficult.

5.4 Gold pillars on highly doped silicon

In section 4.4.1 (p. 88ff.) the applicability of Au pillars on Si substrates in an electrochemical environment was tested. The pillars were fabricated by the nTP process, which allows for a systematic variation of the diameter and spacing of the pillars. Hence, these structures can be very useful for the evaluation of the influence of geometrical factors on electrochemical properties. In the following, the results of these investigations are summarized:

- The oxidation/reduction of Au pillars on Si and the HER at these samples was compared with the behavior of extended Au surfaces. The reactions occurred in very similar potential regimes.
- The double-layer capacity of Si in 1M HClO₄ was found to be much higher than the one of extended Au surfaces.
- The applicability of nTP-manufactured free standing nanostructures on Si in electrochemical experiments was successfully demonstrated.
- The dimensions and the spacing of the Au pillars were maintained during electrochemical experiments. However, some pillars detached from the Si support.

The electrochemical measurements prove that the electric contact, which was established via a silver paste on the HF-treated rear side of the Si substrate, is an Ohmic contact. Therefore, such a system is suitable for the utilization in electrochemical experiments. The main benefit of these structures is the large variability offered by the nanotransfer technique: The width of the Au pillars can be varied systematically from a minimum of 5-10nm through hundreds of nanometers to micrometers. In particular, the electrocatalytic activity of Pt on such Au pillars can be investigated thoroughly to gain further knowledge on the spillover effect and, more generally, on the interdependence of Pt and Au in an electrocatalytic system.

5.5 Relevance of spillover: Platinum nanoislands on gold lines

In section 4.4.2 (p. 94ff.) the electrocatalytic activity of Pt nanoislands on 160nm-wide Au lines and on extended Au(111) surfaces was compared. The objective of these investigations was the verification of the spillover effect. The activity of Pt nanoislands on Au lines was expected to be lower than the one of Pt nanoislands on extended Au surfaces: The Au lines were established by NIL between polymer lines. The polymer lines were thought to act as an inhibitor for spillover of adsorbed hydrogen atoms from Pt nanoislands in the vicinity of a

polymer line to the Au surface and vice versa (compare with Figure 4.4-6, p. 94). In detail the following results were achieved:

- The applicability of Au substrates with NIL-nanostructured polymer lines in electrochemical measurements was successfully demonstrated: the polymer lines were stable and electrochemically inactive in the acidic electrolyte.
- The electrocatalytic activity of Pt nanoislands on Au lines with a Pt coverage of 0.09ML is very similar to the activity of Pt(111).
- A comparison of the electrocatalytic activity of Pt nanoislands on Au lines between polymer lines with the activity of Pt nanoislands on extended Au(111) surfaces for the HOR and the HER showed that no difference in activity can be seen for high Pt coverage (~0.2ML). In contrast, for low Pt coverage (~0.09ML) a decrease in activity by a factor of two was found for the Pt nanoislands on Au lines (compare with Figure 5.5-1).

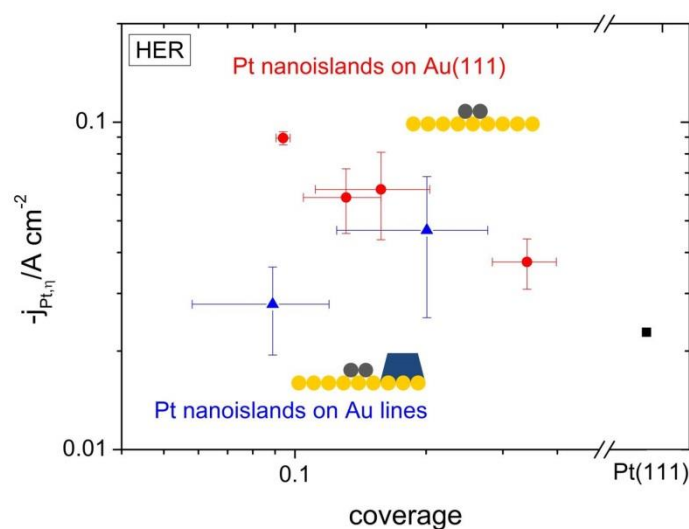


Figure 5.5-1 Pt-specific current density $j_{Pt,\eta}$ for the HER at an overpotential $\eta=-0.02V$, plotted versus coverage for Pt nanoislands on extended Au(111) surfaces, for Pt nanoislands on Au lines and for Pt(111). Schemes of the different configurations of Pt nanoislands on the Au surface are included.

These findings are as expected and can be interpreted in terms of spillover, the concept of which was explained in section 2.3.3 (p. 35ff.): When Pt coverage on the Au surface is high, spillover of adsorbed hydrogen atoms from Pt to the Au surface or vice versa may happen to some extent, but is not significant, due to the large Pt surface area. This is the case for sample PB3 with a Pt coverage of 0.2ML on the Au lines. For these and higher coverages the strain effect may be dominant. For smaller Pt coverage on Au lines, as in the case of sample PB4 (Pt coverage $c=0.09ML$), the amount of hydrogen atoms that spill over to the Au surface and vice versa is more significant. Following this reasoning, the sample with polymer lines (PB4) was

less active than the ones without polymer lines (Pt nanoislands on extended Au surfaces), because the polymer lines acted as a barrier and inhibited spillover. Since the activity of this sample (PB4) is comparable to the activity of Pt(111), spillover is the dominant effect at this and probably also at lower coverages. Furthermore, the width of the Au lines of 160nm is small enough to diminish or inhibit a considerable fraction of hydrogen spillover, when taking into account the optimum radius of the Au surface of 30-40nm surrounding a Pt or Pd nanoisland, as found by Wang and coworkers [42] (compare with section 2.3.3, p. 35ff.). These results can be discussed without consideration of strain, since the Pt-nanoisland size and coverage were practically equal for compared samples due to similar deposition routines. Thus, it was demonstrated that spillover influences the activity of Pt nanoislands on Au surfaces. Furthermore, the dimension of the Au surface surrounding a Pt nanoisland, which is necessary for spillover was determined to be in a range of 50 to 100nm.

6 Summary and conclusions

The discussion of the electrocatalytic activity of different systems of Pt nanostructures on Au illustrated that the interdependence of Pt and Au is determined by several factors. One main factor was identified as the defect sites on the Au(111) surface. However, the defect-density effect, can have its origin in a different electronic structure of low-coordinated metal atoms, such as a shift in d-band center and therefore altered adsorption energies, but also in facilitated hydrogen spillover at such sites. Hence, it is obvious, that several factors that determine the electrocatalytic activity are correlated and not easily separable. Nevertheless, this thesis showed that a quantification of the contribution of different effects is possible, by using different approaches, such as the variation of defect density of an extended Au(111) surface and the fabrication of nanometer-wide Au lines with Pt decoration.

The overall objective of this work was to contribute to the fundamental understanding of the HER and HOR at Pt nanostructures on Au surfaces. This goal was pursued by application of different methods, starting from the conventional electrochemical technique of Pt deposition on extended single crystalline Au surfaces. The approach was expanded gradually, first of all, by generating defects on the Au surface and comparison of the measured electrocatalytic activities. Results of this work served as a basis for novel electrode structures, which were fabricated on the one hand by a micellar deposition of Pt nanospheres on an extended Au(111) surface. On the other hand nanoimprint techniques, i.e. NIL and nTP, were used to establish defined nanostructure arrays of Au, on which Pt was deposited electrochemically.

A summarized analysis of the investigations on extended Au surfaces is presented in the following part: The electrocatalytic activity of Pt nanospheres on Au(111) was comparable to the electrocatalytic activity of Pt(111), but considerably smaller than the one of Pt nanoislands on Au(111). These results point out that the electrocatalytic activity of Pt is related to strain and/or spillover effect.

A similar consequence was drawn from the analysis of the electrocatalytic activities of Pt nanoislands, which were deposited electrochemically on Au(111) surfaces. It was shown that their activity increases with decreasing coverage. In particular the activity of Pt nanoislands on Au(111) is higher than the activity of bulk Pt(111). Variation of the defect

density on the Au(111) surface at constant Pt coverage demonstrated an activity enhancement by a factor of two to three for Pt on defect-rich Au(111) when compared with defect-poor Au(111). The enhancement was attributed to the unique activity of Pt nanoislands on the lower terrace of Au(111) step/defect sites.

Implementation of nanoimprint techniques in electrochemistry with the aim to generate ordered arrays of defined nanostructures was also successful. By depositing Pt nanoislands on 160nm-wide Au lines between polymer lines the spillover effect could be demonstrated: a comparison of these electrodes with Pt nanoislands on extended Au(111) electrodes showed a decreased activity of the polymer-line electrodes in the case of small Pt coverage. This is an indication for the diminishment of the spillover of hydrogen atoms to and from the Pt nanostructures (for HOR and HER, respectively) when polymer lines are present on the Au surface. Involved parameters, such as the ideal radius of the Au surface surrounding a Pt nanostructure and an influence of Pt coverage, as theoretically determined by Wang et al. [42], were confirmed.

The utilization of Au nanostructures, which are limited in a second direction, i.e. by generation of Au pillars via nTP, was also successful: The applicability of such electrode structures in an electrochemical system was demonstrated. Hence, such a structure is suitable for the systematic evaluation of involved parameters, since the width of the Au pillars can be varied successively from a minimum of approximately 5nm to several hundreds of nanometers or even micrometers.

As a consequence, the nanolithography techniques could be used to generate electrode structures with a maximum ratio of electrocatalytic activity to active material. Therefore, the utilization of nanoimprinted electrode structures in an electrochemical system is highly profitable. Moreover, the nanoimprint techniques are designed for large-scale application. Thus, the demonstration of the applicability of such electrode structures in electrochemical systems is also of industrial relevance: fast and efficient pattern transfer over large areas is possible with a roll-to-roll apparatus, which is already used for conventional printing.

Once again it became clear that the considered effects, strain, defect density and spillover, contribute to the electrocatalytic activity and are related to each other. The investigations performed for this thesis demonstrated the separability of the involved effects by different nanostructuring methods. Hence, it is perceivable that new techniques, which yield increasingly defined surface structures, constitute an important factor for the

identification of the mechanisms underlying complex electrocatalytic reactions. In addition, advanced theoretical methods, such as DFT calculations accounting for electrolyte and electrode potential, can contribute to a fundamental understanding of electrocatalysis.

Bibliography

- [1] A.J. Appleby, Electrocatalysis, in: B.E. Conway, J.O.M. Bockris, E. Yeager, S.U.M. Khan, E.R. White (Eds.) *Comprehensive Treatise of Electrochemistry*, vol. 7, Plenum Press, 1981.
- [2] V.S. Bagockii, *Fundamentals of Electrochemistry*, 2nd ed., Wiley-Interscience, Hoboken, NJ, 2006.
- [3] J. Tafel, *Z. Phys. Chem.*, 50 (1905) 641.
- [4] P. Sabatier, *Ber. Dtsch. Chem. Ges.*, 44 (1911) 1984.
- [5] L.P. Hammett, *J. Am. Chem. Soc.*, 46 (1924) 7.
- [6] H.S. Taylor, *Proceedings of the Royal Society of London. Series A*, 108 (1925) 105.
- [7] J. Heyrovský, *Recl. Trav. Chim. Pays-Bas*, 46 (1927) 582.
- [8] T. Erdey-Gruz, M. Volmer, *Z. Phys. Chem.*, (1930).
- [9] H. Gerischer, W. Vielstich, *Z. Phys. Chem.*, 3 (1955) 16.
- [10] K.J. Vetter, *Elektrochemische Kinetik*, Springer Verlag, 1961.
- [11] K.J. Vetter, *Angew. Chem.*, 73 (1961) 277.
- [12] J. Clavilier, *J. Electroanal. Chem.*, 107 (1979) 211.
- [13] J. Clavilier, R. Faure, G. Guinet, R. Durand, *J. Electroanal. Chem.*, 107 (1979) 205.
- [14] L. Kibler, A. Cuesta, M. Kleinert, D. Kolb, *J. Electroanal. Chem.*, 484 (2000) 73.
- [15] L.A. Kibler, *Preparation and Characterization of Noble Metal Single Crystal Electrode Surfaces*, International Society of Electrochemistry, 2003.
- [16] D. Zurawski, L. Rice, M. Hourani, A. Wieckowski, *J. Electroanal. Chem.*, 230 (1987) 221.
- [17] L. Chen, A. Lasia, *J. Electrochem. Soc.*, 138 (1991) 3321.
- [18] E.J. Kelly, *J. Electrochem. Soc.*, 112 (1965) 124.
- [19] N. Markovic, B. Grgur, P. Ross, *J. Phys. Chem. B*, 101 (1997) 5405.
- [20] N. Marković, P. Ross Jr, *Surf. Sci. Rep.*, 45 (2002) 117.
- [21] A. Wieckowski, E.R. Savinova, C.G. Vayenas, *Catalysis and electrocatalysis at nanoparticle surfaces*, CRC, 2003.
- [22] T. Brülle, W. Ju, P. Niedermayr, A. Denisenko, O. Paschos, O. Schneider, U. Stimming, *Molecules*, 16 (2011) 10059.
- [23] L.A. Kibler, *ChemPhysChem*, 7 (2006) 985.

- [24] L.A. Kibler, *Electrochim. Acta*, 53 (2008) 6824.
- [25] J. Meier, K.A. Friedrich, U. Stimming, *Faraday Discuss.*, 121 (2002) 365.
- [26] S. Pandelov, U. Stimming, *Electrochim. Acta*, 52 (2007) 5548.
- [27] H. Wolfschmidt, R. Bussar, U. Stimming, *J. Phys.: Condens. Matter*, 20 (2008) 374127.
- [28] H. Wolfschmidt, D. Weingarth, U. Stimming, *ChemPhysChem*, 11 (2010) 1533.
- [29] F. Hernandez, H. Baltruschat, *J. Solid State Electrochem.*, 11 (2007) 877.
- [30] T. Brülle, A. Denisenko, H. Sternschulte, U. Stimming, *PCCP*, 13 (2011) 12883.
- [31] T. Brülle, U. Stimming, *J. Electroanal. Chem.*, 636 (2009) 10.
- [32] T. Brülle, Investigations on the electrocatalytic hydrogen reaction on extended and nanostructured surfaces, Dissertation, Lehrstuhl für Technische Physik E19, Technische Universität München, 2012.
- [33] Y. Gohda, A. Groß, *J. Electroanal. Chem.*, 607 (2007) 47.
- [34] J. Greeley, T.F. Jaramillo, J. Bonde, I. Chorkendorff, J.K. Nørskov, *Nature Mater.*, 5 (2006) 909.
- [35] B. Hammer, J. Nørskov, *Surf. Sci.*, 343 (1995) 211.
- [36] P. Quaino, E. Santos, H. Wolfschmidt, M.A. Montero, U. Stimming, *Catal. Today*, 177 (2011) 55.
- [37] A. Roudgar, A. Groß, *J. Electroanal. Chem.*, 548 (2003) 121.
- [38] A. Roudgar, A. Groß, *Surf. Sci.*, 559 (2004) L180.
- [39] A. Ruban, B. Hammer, P. Stoltze, H.L. Skriver, J. Nørskov, *J. Mol. Catal. A: Chem.*, 115 (1997) 421.
- [40] M.E. Björketun, G.S. Karlberg, J. Rossmeisl, I. Chorkendorff, H. Wolfschmidt, U. Stimming, J.K. Nørskov, *Phys. Rev. B*, 84 (2011) 045407.
- [41] M. Eikerling, J. Meier, U. Stimming, *Z. Phys. Chem.*, 217 (2003) 395.
- [42] L. Wang, U. Stimming, M. Eikerling, *Electrocatalysis*, 1 (2010) 60.
- [43] T. Kondo, M. Shibata, N. Hayashi, H. Fukumitsu, T. Masuda, S. Takakusagi, K. Uosaki, *Electrochim. Acta*, 55 (2010) 8302.
- [44] G. Kästle, H.G. Boyen, F. Weigl, G. Lengl, T. Herzog, P. Ziemann, S. Riethmüller, O. Mayer, C. Hartmann, J.P. Spatz, M. Möller, M. Ozawa, F. Banhart, M.G. Garnier, P. Oelhafen, *Adv. Funct. Mater.*, 13 (2003) 853.
- [45] J.P. Spatz, S. Mössmer, C. Hartmann, M. Möller, T. Herzog, M. Krieger, H.-G. Boyen, P. Ziemann, B. Kabius, *Langmuir*, 16 (1999) 407.
- [46] D. Kolb, R. Ullmann, T. Will, *Science*, 275 (1997) 1097.

- [47] S. Harrer, S. Strobel, G. Scarpa, G. Abstreiter, M. Tornow, P. Lugli, *IEEE Trans. Nanotechnol.*, 7 (2008) 363.
- [48] P. Lugli, S. Harrer, S. Strobel, F. Brunetti, G. Scarpa, M. Tornow, G. Abstreiter, *Proc. 7th IEEE Conference on Nanotechnology*, 2007.
- [49] G. Scarpa, S. Harrer, A. Abdellah, G. Penso-Blanco, P. Lugli, S. Strobel, G. Abstreiter, M. Tornow, *Proc. 9th IEEE Conference on Nanotechnology*, 2009.
- [50] S. Strobel, S. Harrer, G. Penso Blanco, G. Scarpa, G. Abstreiter, P. Lugli, M. Tornow, *Small*, 5 (2009) 579.
- [51] B. Weiler, C. Ostermayr, U. Stimming, G. Scarpa, *Proc. The Energy and Materials Research Conference 2012*, 1 (2012) 293.
- [52] C.H. Hamann, A. Hamnett, W. Vielstich, *Electrochemistry*, 2nd, completely revised and updated ed., WILEY-VCH Verlag GmbH & Co. KGaA, Weinheim, 2007.
- [53] A.J. Bard, L.R. Faulkner, *Electrochemical methods: Fundamentals and Applications*, John Wiley & Sons, Inc., 2001.
- [54] W. Schmickler, E. Santos, *Interfacial Electrochemistry*, 2nd ed., Springer, 2010.
- [55] H. Gerischer, W. Vielstich, *Z. Phys. Chem.*, 4 (1955) 10.
- [56] K. Uosaki, Y. Shen, T. Kondo, *J. Phys. Chem.*, 99 (1995) 14117.
- [57] C. Kittel, *Introduction to Solid State Physics*, 7th ed., John Wiley & Sons, 1996.
- [58] J.V. Barth, H. Brune, G. Ertl, R.J. Behm, *Phys. Rev. B*, 42 (1990) 9307.
- [59] T. Michely, G. Comsa, *Surf. Sci.*, 256 (1991) 217.
- [60] Y. Hasegawa, P. Avouris, *Science*, 258 (1992) 1763.
- [61] D.L. Abernathy, D. Gibbs, G. Grübel, K.G. Huang, S.G.J. Mochrie, A.R. Sandy, D.M. Zehner, *Surf. Sci.*, 283 (1993) 260.
- [62] D. Kolb, *Prog. Surf. Sci.*, 51 (1996) 109.
- [63] V. Repain, J. Berroir, S. Rousset, J. Lecoer, *Appl. Surf. Sci.*, 162 (2000) 30.
- [64] Reprinted from *Surface Science*, Vol. 283, D.L. Abernathy, D. Gibbs, G. Grübel, K.G. Huang, S.G.J. Mochrie, A.R. Sandy, D.M. Zehner, *Reconstruction of the (111) and (001) surfaces of Au and Pt: thermal behavior*, p. 260-276, Copyright (1993), with permission from Elsevier.
- [65] Reprinted from *Physical Review B*, Vol. 42, Iss. 15, J.V. Barth, H. Brune, G. Ertl, R.J. Behm, *Scanning tunneling microscopy observations on the reconstructed Au(111) surface: Atomic structure, long-range superstructure, rotational domains, and surface defects*, p. 9307-9318, with permission from Prof. Dr. J.V. Barth, Copyright (1990) by The American Physical Society.

- [66] Reprinted from Applied Surface Science, Vol. 162-163, V. Repain, J. Berroir, S. Rousset, J. Lecoer, Reconstruction, step edges and self-organization on the Au(111) surface, p. 30-36, Copyright (2000), with permission from Elsevier.
- [67] J. Wang, B. Ocko, A.J. Davenport, H.S. Isaacs, Phys. Rev. B, 46 (1992) 10321.
- [68] O.M. Magnussen, J. Hageböck, J. Hotlos, R.J. Behm, Faraday Discuss., 94 (1992) 329.
- [69] X. Gao, A. Hamelin, M.J. Weaver, J. Chem. Phys., 95 (1991) 6993.
- [70] J.O.M. Bockris, A.R. Despic, The Mechanism of Deposition and Dissolution of Metals, in: H. Eyring (Ed.) Physical Chemistry, An Advanced Treatise IXB/Electrochemistry, Academic Press, 1970.
- [71] H.F. Waibel, M. Kleinert, L. Kibler, D. Kolb, Electrochim. Acta, 47 (2002) 1461.
- [72] L. Kibler, M. Kleinert, R. Randler, D. Kolb, Surf. Sci., 443 (1999) 19.
- [73] J. Tang, M. Petri, L. Kibler, D. Kolb, Electrochim. Acta, 51 (2005) 125.
- [74] F. Hernandez, H. Baltruschat, Langmuir, 22 (2006) 4877.
- [75] N.W. Ashcroft, N.D. Mermin, Solid State Physics, Brooks/Cole, 2009.
- [76] E. Budevski, V. Bostanov, G. Staikov, Annu. Rev. Mater. Sci., 10 (1980) 85.
- [77] E. Budevski, G. Staikov, W.J. Lorenz, Electrochim. Acta, 45 (2000) 2559.
- [78] L.A. Kibler, A.M. El-Aziz, R. Hoyer, D.M. Kolb, Angew. Chem. Int. Ed., 44 (2005) 2080.
- [79] J. Greeley, J.K. Nørskov, L.A. Kibler, A.M. El-Aziz, D.M. Kolb, ChemPhysChem, 7 (2006) 1032.
- [80] B. Hammer, J.K. Nørskov, Adv. Catal., 45 (2000) 71.
- [81] A. Groß, Theoretical Surface Science, 2nd ed., Springer-Verlag Berlin Heidelberg, 2009.
- [82] M. Mavrikakis, B. Hammer, J.K. Nørskov, Phys. Rev. Lett., 81 (1998) 2819.
- [83] A. Roudgar, A. Groß, Phys. Rev. B, 67 (2003) 033409.
- [84] J.K. Nørskov, T. Bligaard, A. Logadottir, J. Kitchin, J. Chen, S. Pandalov, U. Stimming, J. Electrochem. Soc., 152 (2005) J23.
- [85] E. Skúlason, G.S. Karlberg, J. Rossmeisl, T. Bligaard, J. Greeley, H. Jónsson, J.K. Nørskov, PCCP, 9 (2007) 3241.
- [86] T. Roman, A. Groß, Catal. Today, 202 (2013) 183.
- [87] R. Parsons, Trans. Faraday Soc., 54 (1958) 1053.
- [88] I.A. Pašti, N.M. Gavrilov, S.V. Mentus, Advances in Physical Chemistry, 2011 (2011).

- [89] M. Boudart, *Adv. Catal.*, 20 (1969) 153.
- [90] T. Engel, G. Ertl, *Adv. Catal.*, 28 (1979) 1.
- [91] M. Boudart, *J. Mol. Catal.*, 30 (1985) 27.
- [92] H. Conrad, G. Ertl, E. Latta, *Surf. Sci.*, 41 (1974) 435.
- [93] J.A. Dumesic, H. Topsøe, S. Khammouma, M. Boudart, *J. Catal.*, 37 (1975) 503.
- [94] P. Emmett, S. Brunauer, *J. Am. Chem. Soc.*, 56 (1934) 35.
- [95] G. Ertl, *Catalysis Reviews*, 21 (1980) 201.
- [96] G.A. Somorjai, D.W. Blakely, *Nature*, 258 (1975) 580.
- [97] S. Bernasek, G. Somorjai, *J. Chem. Phys.*, 62 (1975) 3149.
- [98] D. Blakely, G. Somorjai, *J. Catal.*, 42 (1976) 181.
- [99] J. Gland, K. Baron, G. Somorjai, *J. Catal.*, 36 (1975) 305.
- [100] A. Gee, B. Hayden, C. Mormiche, T. Nunney, *J. Chem. Phys.*, 112 (2000) 7660.
- [101] I. Groot, A.W. Kleyn, L.B. Juurlink, *Angew. Chem. Int. Ed.*, 50 (2011) 5174.
- [102] N. Lebedeva, M. Koper, J. Feliu, R. Van Santen, *J. Phys. Chem. B*, 106 (2002) 12938.
- [103] G. Garcia, M.T.M. Koper, *PCCP*, 10 (2008) 3802.
- [104] N.P. Lebedeva, A. Rodes, J.M. Feliu, M.T.M. Koper, R.A. van Santen, *J. Phys. Chem. B*, 106 (2002) 9863.
- [105] M.J.S. Farias, E. Herrero, J.M. Feliu, *The Journal of Physical Chemistry C*, 117 (2013) 2903.
- [106] J. Ludwig, D.G. Vlachos, A.C. Van Duin, W.A. Goddard III, *J. Phys. Chem. B*, 110 (2006) 4274.
- [107] F. Ahmed, R. Nagumo, R. Miura, S. Ai, H. Tsuboi, N. Hatakeyama, A. Endou, H. Takaba, M. Kubo, A. Miyamoto, *Appl. Surf. Sci.*, 257 (2011) 10503.
- [108] J. Kuriacose, *Ind. J. Chem.*, 5 (1957) 646.
- [109] H.S. Taylor, *Actes Congr. Int. Catal.*, 2 (1961) 159.
- [110] J.H. Sinfelt, P.J. Lucchesi, *J. Am. Chem. Soc.*, 85 (1963) 3365.
- [111] S. Khoobiar, *J. Phys. Chem.*, 68 (1964) 411.
- [112] W.C. Conner, G. Pajonk, S. Teichner, *Adv. Catal*, 34 (1986) 1.
- [113] W.C. Conner, J.L. Falconer, *Chem. Rev.*, 95 (1995) 759.
- [114] J.O.M. Bockris, J. McHardy, *J. Electrochem. Soc.*, 120 (1973) 61.
- [115] K. Seto, J. Noël, J. Lipkowski, Z. Altounian, R. Reeves, *J. Electrochem. Soc.*, 136 (1989) 1910.

- [116] K.-W. Park, K.-S. Ahn, Y.-C. Nah, J.-H. Choi, Y.-E. Sung, *J. Phys. Chem. B*, 107 (2003) 4352.
- [117] J. Meier, Herstellung, Charakterisierung und Reaktivität von Oberflächeninhomogenitäten an der Grenzfläche fest-flüssig, Dissertation, Lehrstuhl für Physik E19, Technische Universität München, 2003.
- [118] G.S. Karlberg, J.K. Nørskov, unpublished results, (2008).
- [119] A. Corma, M. Boronat, S. González, F. Illas, *Chem. Commun.*, (2007) 3371.
- [120] A. Hamelin, *J. Electroanal. Chem.*, 407 (1996) 1.
- [121] D. Dickertmann, J. Schultze, K. Vetter, *J. Electroanal. Chem.*, 55 (1974) 429.
- [122] K. Juodkazis, A. Lukinskas, B. Šebeka, *Electrochem. Commun.*, 2 (2000) 503.
- [123] Z. Jusys, S. Bruckenstein, *Electrochem. Solid-State Lett.*, 1 (1998) 74.
- [124] T. Kondo, J. Morita, K. Hanaoka, S. Takakusagi, K. Tamura, M. Takahasi, J. Mizuki, K. Uosaki, *J. Phys. Chem. C*, 111 (2007) 13197.
- [125] F.J.R. Nieto, G. Andreasen, M.E. Martins, F. Castez, R.C. Salvarezza, A.J. Arvia, *J. Phys. Chem. B*, 107 (2003) 11452.
- [126] M. Schneeweiss, D. Kolb, *Solid State Ionics*, 94 (1997) 171.
- [127] D.J. Trevor, C.E.D. Chidsey, D.N. Loiacono, *Phys. Rev. Lett.*, 62 (1989) 929.
- [128] S. Xia, V. Birss, *J. Electroanal. Chem.*, 500 (2001) 562.
- [129] *CRC Handbook of Chemistry and Physics*, 52nd ed., Cleveland, OH, 1971.
- [130] Y.N.C. Chan, G.S.W. Craig, R.R. Schrock, R.E. Cohen, *Chem. Mater.*, 4 (1992) 885.
- [131] S. Krishnamoorthy, C. Hinderling, H. Heinzelmann, *Mater. Today*, 9 (2006) 40.
- [132] J.F. Moulder, W.F. Stickle, P.E. Sobol, K.D. Bomben, *Handbook of X-ray Photoelectron Spectroscopy*, Physical Electronics, Inc., 1995.
- [133] C. Ostermayr, U. Stimming, *Surf. Sci.*, 631 (2015) 229.
- [134] G. Binnig, H. Rohrer, C. Gerber, E. Weibel, *Phys. Rev. Lett.*, 49 (1982) 57.
- [135] G. Binnig, H. Rohrer, C. Gerber, E. Weibel, *Appl. Phys. Lett.*, 40 (1982) 178.
- [136] R. Wiesendanger, *Scanning probe microscopy and spectroscopy: methods and applications*, Cambridge University Press, 1994.
- [137] G. Binnig, C.F. Quate, C. Gerber, *Phys. Rev. Lett.*, 56 (1986) 930.
- [138] R. Sonnenfeld, P.K. Hansma, *Science*, 232 (1986) 211.
- [139] P. Lustenberger, H. Rohrer, R. Christoph, H. Siegenthaler, *J. Electroanal. Chem.*, 243 (1988) 225.
- [140] K. Itaya, E. Tomita, *Surf. Sci.*, 201 (1988) L507.

- [141] J.G. Xu, X.W. Wang, *Surf. Sci.*, 408 (1998) 317.
- [142] N. Batina, T. Will, D.M. Kolb, *Faraday Discuss.*, 94 (1992) 93.
- [143] M. Hölzle, V. Zwing, D. Kolb, *Electrochim. Acta*, 40 (1995) 1237.
- [144] A.A. Michri, A.G. Pshchenichnikov, R.K. Burshtein, *Sov. Electrochem.*, 8 (1972) 351.
- [145] K. Friedrich, F. Henglein, U. Stimming, W. Unkauf, *Electrochim. Acta*, 45 (2000) 3283.
- [146] D.V. Heyd, D.A. Harrington, *J. Electroanal. Chem.*, 335 (1992) 19.
- [147] J.O.M. Bockris, A.K.N. Reddy, *Modern Electrochemistry*, Vol. 1, Ionics, 2nd ed., Plenum Press, New York, 1998.
- [148] S. Chen, A. Kucernak, *J. Phys. Chem. B*, 108 (2004) 13984.
- [149] E. Yeager, J. Kuta, *Techniques for the Study of Electrode Processes*, in: H. Eyring, D. Henderson, W. Jost (Eds.) *Physical Chemistry, An Advanced Treatise*, vol. IXA/Electrochemistry, Academic Press, New York/London, 1970, pp. 345.
- [150] V. Climent, R. Gómez, J.M. Feliu, *Electrochim. Acta*, 45 (1999) 629.
- [151] M.N. Zinner, *Charaterization of electrochemically polarized Au(111) surfaces via STM*, Bachelor Thesis, Lehrstuhl für Technische Physik E19, Technische Universität München, 2011.
- [152] A. Kuzume, E. Herrero, J.M. Feliu, R.J. Nichols, D.J. Schiffrin, *J. Electroanal. Chem.*, 570 (2004) 157.
- [153] Reprinted from *Surface Science*, Vol. 631, C. Ostermayr, U. Stimming, *Electrocatalytic activity of platinum submonolayers on defect-rich Au(111)*, p. 229-234, Copyright (2015), with permission from Elsevier.
- [154] A. El-Aziz, L. Kibler, *J. Electroanal. Chem.*, 534 (2002) 107.
- [155] W.A. Hofer, G. Ritz, W. Hebenstreit, M. Schmid, P. Varga, J. Redinger, R. Podloucky, *Surf. Sci.*, 405 (1998) L514.
- [156] H.E. Hoster, A. Bergbreiter, P.M. Erne, T. Hager, H. Rauscher, R.J. Behm, *PCCP*, 10 (2008) 3812.
- [157] M. Schmid, H. Stadler, P. Varga, *Phys. Rev. Lett.*, 70 (1993) 1441.
- [158] F. Maroun, F. Ozanam, O. Magnussen, R. Behm, *Science*, 293 (2001) 1811.
- [159] T. Janssens, B. Clausen, B. Hvolbæk, H. Falsig, C. Christensen, T. Bligaard, J. Nørskov, *Top. Catal.*, 44 (2007) 15.
- [160] N. Tian, Z.-Y. Zhou, S.-G. Sun, *J. Phys. Chem. C*, 112 (2008) 19801.

- [161] G.-R. Zhang, D. Zhao, Y.-Y. Feng, B. Zhang, D.S. Su, G. Liu, B.-Q. Xu, *ACS Nano*, 6 (2012) 2226.
- [162] P.M.M.C. Bressers, J.J. Kelly, J.G.E. Gardeniers, M. Elwenspoek, *J. Electrochem. Soc.*, 143 (1996) 1744.
- [163] H. Seidel, L. Csepregi, A. Heuberger, H. Baumgärtel, *J. Electrochem. Soc.*, 137 (1990) 3612.
- [164] I. Zobel, *Sensors and Actuators A: Physical*, 84 (2000) 116.
- [165] L. Canham, *Appl. Phys. Lett.*, 57 (1990) 1046.
- [166] X.G. Zhang, S.D. Collins, R.L. Smith, *J. Electrochem. Soc.*, 136 (1989) 1561.

Appendix

A1 Symbols and abbreviations

A	surface area
$\alpha_{a,c}$	anodic, cathodic transfer coefficient
AFM	atomic force microscopy
b	Tafel slope
BCML	diblock copolymer micelle lithography
C_{DL}	double layer capacitance
CE	counter electrode
$C_{Ox,Red}(x, t)$	concentration of oxidizing, reducing agent at point x and time t
CV	cyclic voltammetry/cyclic voltammogram
DFT	density functional theory
DOS	density of states
$D_{Ox,Red}$	diffusion coefficient of oxidizing, reducing agent
e	elementary charge
ϵ	dielectric constant of electrolyte
ϵ_0	permittivity of the free space
EC STM	electrochemical scanning tunneling microscopy
EIS	electrochemical impedance spectroscopy
F	Faraday constant
fcc	face centered cubic
FRA	frequency response analyzer
$\Delta G, (\Delta G^0)$	(standard) molar free energy of reaction
ΔG_H	free energy of hydrogen adsorption
$\Delta G_{c,a}^\ddagger, (\Delta G_{0c,0a}^\ddagger)$	(standard) cathodic, anodic activation energy
η	overpotential
ΔH	enthalpy of formation
H_{ad}	adsorbed hydrogen atom
hcp	hexagonal close packed
HER	hydrogen evolution reaction

HOPG	highly oriented pyrolytic graphite
HOR	hydrogen oxidation reaction
I_0	exchange current
$I_{c,a}$	cathodic, anodic current
I_t	tunneling current
j_0	exchange current density
$J_{Ox,Red}$	flux of oxidizing, reducing species
$k_{f,b}, (k_{f,b}^0)$	(standard) forward, backward rate constant
ML	monolayer
MSE	mercury sulfate electrode
n	number of transferred electrons
N_A	Avogadro constant
NHE	normal hydrogen electrode
NIL	nanoimprint lithography
nTP	nanotransfer printing
OER	oxygen evolution reaction
ORR	oxygen reduction reaction
φ	inner/Galvani potential
ρ	space-charge density
RE	reference electrode
rds	rate determining step
RHE	reversible hydrogen electrode
RTP	rapid thermal processing
R_Ω	Ohmic resistance of electrolyte
ΔS	entropy of formation
SHE	standard hydrogen electrode
STM	scanning tunneling microscopy
Θ, Θ_H	coverage of adsorbed hydrogen on the electrode surface
T	absolute temperature
TM AFM	tapping mode atomic force microscopy
$\Delta U, (\Delta U^\ominus)$	(standard) potential difference between electrodes at open circuit
U^\ominus	standard electrode potential
U_0	equilibrium potential

UHV	ultrahigh vacuum
upd	underpotential deposition
$v_{f,b}$	forward, backward reaction rate
WE	working electrode
XPS	X-ray photoelectron spectroscopy
XRD	X-ray diffraction

A2 Additional experimental details

To section 4.1.1, p. 57ff.: Detailed table of Pt coverage on samples 1-16:

Table 8 Comparison of Pt coverage on the different samples, determined via evaluation of the charge recorded during Pt deposition, hydrogen ad-/desorption, CO-adlayer oxidation and PtO_x reduction. The mean coverage was calculated from all values listed, except Pt deposition coverage, which had a very large error.

Sample name	Pt coverage [ML], determined via				Mean coverage [ML]
	Pt deposition charge	Hydrogen ad-/desorption charge	CO-adlayer oxidation charge	PtO _x reduction charge	
1	1.52±0.01	0.282±0.006	0.346±0.001	0.395±0.001	0.341±0.057
2	0	0.059±0.006	0.041±0.001	0.045±0.001	0.048±0.010
4	2.11±0.11	0.108±0.006	0.199±0.001	0.166±0.001	0.158±0.046
5	0.398±0.063	0.101±0.006	0.159±0.001	0.113±0.001	0.124±0.030
6	2.37±0.04	0.306±0.006	0.273±0.001	0.336±0.001	0.305±0.032
7	0.233±0.032	0.127±0.006	0.183±0.001	0.154±0.001	0.155±0.028
8	0.091±0.032	0.108±0.006	0.080±0.001	0.125±0.001	0.104±0.023
9	0.060±0.032	0.106±0.006	0.066±0.001	0.099±0.001	0.091±0.021
10	0.377±2.056	0.271±0.006	0.292±0.001	0.391±0.001	0.318±0.064
11	0.044±0.021	0.057±0.006	0.045±0.001	0.057±0.001	0.053±0.007
12	0.004±0.001	0.043±0.006	0.059±0.001	0.067±0.001	0.056±0.012
13	4.42±0.01	0.570±0.006	0.591±0.001	0.659±0.001	0.606±0.046
14	0	0.047±0.006	0.050±0.001	0.056±0.001	0.051±0.004
15	4.72±0.01	0.754±0.006	1.17±0.01	1.06±0.01	0.996±0.217
16	0	0.037±0.006	--	0.059±0.001	0.048±0.016

To section 4.1.1, p. 57ff.: Higher negative current in first scan of hydrogen adsorption measurement compared with second scan:

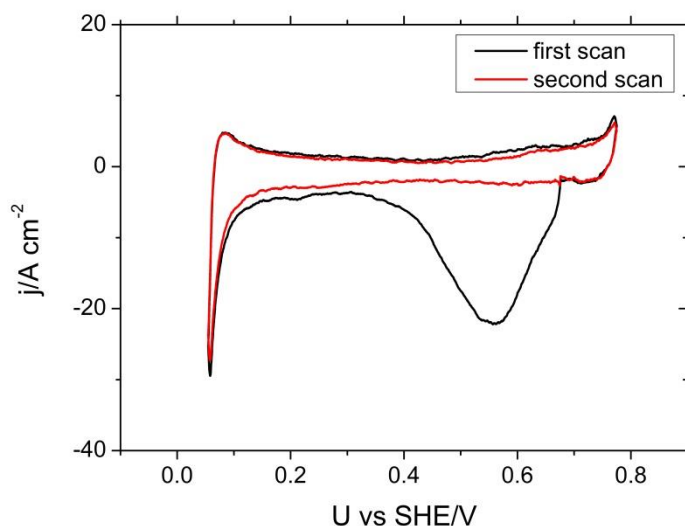


Figure 0-1 First and second scan of the hydrogen adsorption measurement for sample #2. In the first scan a negative peak occurs at 0.55V vs. SHE. The negative current starts to flow from a potential of 0.7V vs. SHE, which corresponds approximately to the onset potential for Pt deposition. Therefore, the current can be ascribed to the reduction of the adsorbed $[PtCl_4]^{2-}$ -complex to metallic Pt.

Error calculations

Any errors corresponding to mean values are standard deviations. Errors of evaluated deposition, adsorption/desorption, oxidation/reduction charges are due to resolution limits in the current ranges of the used potentiostats. Errors of Ohmic drop R_{Ω} and double layer capacitance C_{DL} are due to the error of the corresponding fits if not otherwise mentioned. Errors in HOR-kinetic currents are the sum of the RMSE error of the linear fit of $t^{0.5}$ -I curves and the error which is due to the selection of the time range, in which the fit is performed. The latter error implies the repetition of the fit routine for reasonable time ranges differing from the selected ones and calculation of the corresponding deviation. The error in Pt coverage values calculated by analysis of AFM-/STM-images is due to a sensible estimation of the error made by determination of the diameter of Pt nanostructures and by counting them.

A3 Publications

Some results of this thesis were published previously:

- B. Weiler, C. Ostermayr, U. Stimming, G. Scarpa, Nanostructured electrodes for electrochemical systems applications, in Fuelling the Future: Advances in Science and Technologies for Energy Generation, Transmission and Storage. *Proc. The Energy and Materials Research Conference 2012* **1**, 293 (2012).
- C. Ostermayr, U. Stimming, Electrocatalytic activity of platinum submonolayers on defect-rich Au(111), *Surf. Sci.*, *631* (2015) 229

Danksagung

An dieser Stelle danke ich allen meinen Betreuern, Freunden, Kollegen und meiner Familie für die wunderbare Unterstützung während meiner Doktorandinnenzeit.

Insbesondere möchte ich mich bei Prof. Dr. Ulrich Stimming für die interessanten Diskussionen, die hilfreichen Tipps und die Unterstützung bedanken. Durch meine Doktorarbeit an seinem Lehrstuhl habe ich nicht nur wissenschaftlich sondern auch persönlich sehr viel dazugelernt.

Ein großes Dankeschön geht auch an Prof. Dr. Giuseppe Scarpa und Dr. Oliver Schneider, die mir jederzeit mit hilfreichen Ratschlägen zur Seite gestanden haben.

Meinen Kollegen Dr. Tine Brülle, Celine Rüdiger, Christoph Traunsteiner, Luisa Kneer und Jochen Friedl danke ich für die wunderbare Büroatmosphäre, die guten wissenschaftlichen und nicht-wissenschaftlichen Gespräche und für das geduldige Korrekturlesen dieser Arbeit.

Dr. Tine Brülle, Dr. Claudia Lintz und Dr. Holger Wolfschmidt danke ich für die Einführung in die Elektrochemie und die gute Laboratmosphäre. Gerade während der Anfangszeit habe ich von ihnen viele hilfreiche Tipps bekommen.

In vielerlei Hinsicht danke ich zudem Maximilian Zinner, Benedikt Weiler, Robin Nagel, Dr. Hadwig Sternschulte, Axel Seidenstücker, Dr. Alfred Plettl, Wenbo Ju, Siegfried Schreier, Markus Haß und Joana Figueiredo.

Außerdem danke ich den Mitarbeitern des Lehrstuhls E19, die alle zu einer guten, kollegialen Atmosphäre während der Arbeit beigetragen haben.

Auch die Kollegen von TUM CREATE in Singapur möchte ich erwähnen, die meinen Auslandsaufenthalt zu einem unvergesslichen Erlebnis gemacht haben und mir den Zugang zur Batterie- und Elektromobilitätsforschung erleichtert haben.

Ganz besonderer Dank gilt meinen Eltern, meiner Schwester und meinem Freund Sven Hack, die mich immer wieder ermutigt und an mich geglaubt haben.